Electromagnetic form factors of the nucleon from $N_f = 2 + 1$ lattice QCD

Dalibor Djukanovic,[1,2] Georg von Hippel,[3] Harvey B. Meyer,[1,3] Konstantin Ottnad,[3] Miguel Salg,[3,*] and Hartmut Wittig[1,3]

[1]*Helmholtz Institute Mainz, Staudingerweg 18, 55128 Mainz, Germany*
[2]*GSI Helmholtzzentrum für Schwerionenforschung, 64291 Darmstadt, Germany*
[3]*PRISMA$^+$ Cluster of Excellence and Institute for Nuclear Physics, Johannes Gutenberg University Mainz, Johann-Joachim-Becher-Weg 45, 55128 Mainz, Germany*

(Received 20 September 2023; accepted 15 April 2024; published 22 May 2024)

There is a long-standing discrepancy between different measurements of the electric and magnetic radii of the proton. Lattice QCD calculations are a well-suited tool for theoretical investigations of the structure of the nucleon from first principles. However, all previous lattice studies of the proton's electromagnetic radii have either neglected quark-disconnected contributions or were not extrapolated to the continuum and infinite-volume limit. Here, we present results for the electromagnetic form factors of the proton and neutron computed on the $(2 + 1)$-flavor coordinated lattice simulations (CLS) ensembles including both quark-connected and -disconnected contributions. From simultaneous fits to the Q^2-, pion-mass, lattice-spacing, and finite-volume dependence of the form factors, we determine the electric and magnetic radii and the magnetic moments of the proton and neutron. For the proton, we obtain as our final values $\langle r_E^2\rangle^p = (0.672 \pm 0.014(\text{stat}) \pm 0.018(\text{syst}))$ fm^2, $\langle r_M^2\rangle^p = (0.658 \pm 0.012(\text{stat}) \pm 0.008(\text{syst}))$ fm^2, and $\mu_M^p = (2.739 \pm 0.063(\text{stat}) \pm 0.018(\text{syst})$. The magnetic moment is in good agreement with the experimental value, as is the one of the neutron. On the one hand, our result for the electric (charge) radius of the proton clearly points towards a small value, as favored by muonic hydrogen spectroscopy and the recent ep-scattering experiment by PRad. Our estimate for the magnetic radius, on the other hand, is well compatible with that inferred from the A1 ep-scattering experiment.

DOI: 10.1103/PhysRevD.109.094510

I. INTRODUCTION

Despite the fact that protons and neutrons, collectively referred to as nucleons, make up the largest fraction of the mass of the visible matter in the Universe [1], there are many open problems relating to their internal structure, which are the subject of a broad research effort in subatomic physics. In particular, the question whether discrepant measurements of the electric and magnetic radii can be reconciled has been vigorously debated [2].

Regarding the electric radius, the value reported by the A1 collaboration based on ep-scattering data [$\sqrt{\langle r_E^2\rangle^p} = (0.879 \pm 0.005(\text{stat}) \pm 0.006(\text{syst}))$ fm [3]], while in good agreement with hydrogen spectroscopy [$\sqrt{\langle r_E^2\rangle^p} = 0.8758(77)$ fm [4]] at the time of publication, is incompatible with the most precise determination, which comes from the spectroscopy of muonic hydrogen [$\sqrt{\langle r_E^2\rangle^p} = 0.84087(39)$ fm [5,6]]. This significant inconsistency between measurements using either electrons or muons has been dubbed the "proton radius puzzle" [7]. It has triggered many additional efforts to explain or resolve the discrepancy.

The most recent experiments using electronic hydrogen spectroscopy favor the lower value [8–10], with the exception of Ref. [11] which reports a larger value in agreement with older measurements [4]. The latest determinations from ep scattering yield differing results as well: while the A1 collaboration has essentially confirmed their previous result using the initial-state radiation technique [$\sqrt{\langle r_E^2\rangle^p} = (0.878 \pm 0.011(\text{stat}) \pm 0.031(\text{syst}))$ fm [12]], the PRad experiment at Jefferson Lab has reported a smaller value [$\sqrt{\langle r_E^2\rangle^p} = (0.831 \pm 0.007(\text{stat}) \pm 0.012(\text{syst}))$ fm [13]]. It is worth pointing out that dispersive analyses had already favored a smaller proton radius for a long time [14,15] and continue to do so [16–19]. This applies in particular to the dispersive analysis of the data taken by the A1 experiment [20,21].

In an effort to resolve the still existing tensions, several new experimental efforts are underway: A new ep-scattering experiment, MAGIX [22], is being prepared at the Mainz-based accelerator MESA, which is currently

*msalg@uni-mainz.de

under construction. An upgrade of PRad, dubbed PRad-II, has been approved [23], while the ULQ^2 experiment at ELPH in Tohoku, Japan, is already taking data [24]. To complement the results from electronic and muonic hydrogen spectroscopy and ep scattering with a result from μp scattering, the MUSE collaboration aims to measure the μp cross section to subpercent precision at PSI [25]. Furthermore, the AMBER experiment at CERN plans to determine the electric proton radius to a precision on the order of 0.01 fm using a similar method [26].

For the magnetic radius, an analysis based on the z-expansion obtains two different numbers, depending on whether just the A1 data is analyzed [$\sqrt{\langle r_M^2\rangle^p} = (0.776 \pm 0.034(\text{stat}) \pm 0.017(\text{syst}))$ fm [3,27]] or the rest of the ep-scattering world data excluding A1 [$\sqrt{\langle r_M^2\rangle^p} = 0.914(35)$ fm [27]]. The tension is not as large as for the electric radius, but still, these two numbers are not compatible with each other. For this reason, the magnetic proton radius has received somewhat more attention recently, see, *e.g.,* Ref. [21]. Of the newly planned experiments devoted to the electric proton radius, only MAGIX will address the magnetic radius as well [28], though.

In order to understand whether these discrepancies can be traced to the experimental data and their analyses, or whether they are perhaps an indication for physics beyond the standard model [7], a precise standard-model prediction of the proton's radii is required. Since the inner dynamics of the nucleon is governed by the strong interaction, it is mandatory to apply a nonperturbative methodology, such as lattice QCD, since the QCD coupling is large at typical hadronic scales [29,30].

In lattice QCD as in the context of scattering experiments, radii are extracted from the derivative of the electromagnetic form factors $G_{E,M}(Q^2)$ at $Q^2 = 0$. To distinguish between proton and neutron requires the calculation of quark-disconnected diagrams, which are notorious for their unfavorable signal-to-noise ratio. Previous lattice calculations of electromagnetic form factors and radii published in Refs. [31–48], with the exception of Refs. [41,45], have neglected quark-disconnected contributions due to this technical complication.

In this paper we present our results for the electromagnetic form factors of the proton and neutron computed from a set of coordinated lattice simulations (CLS) ensembles with $N_f = 2 + 1$ flavors of $\mathcal{O}(a)$-improved Wilson quarks [49] at four different lattice spacings and pion masses between 130 and 290 MeV. Our study improves on all previous calculations by explicitly evaluating both quark-connected and -disconnected contributions and, at the same time, taking into account all relevant systematic effects due to excited-state contamination, finite-volume effects and the extrapolation to the physical point. To assess the influence of excited states, we employ a wide range of source-sink separations and apply the summation method. In addition to determining the shape of the form factors at moderate momentum transfers ($Q^2 \lesssim 0.6$ GeV^2), we extract the electric and magnetic radii and magnetic moments in the isovector and isoscalar channels, as well as those of the proton and neutron. For this purpose, we perform simultaneous fits to the Q^2-, pion-mass, lattice-spacing, and finite-volume dependence of the form factors to the expressions resulting from covariant baryon chiral perturbation theory (BχPT), including vector mesons and amending the expressions by models for lattice artifacts. Systematic errors are quantified using a model average with weights derived from the Akaike information criterion (AIC). Our model-averaged results at the physical point reproduce the experimental values of the magnetic moments within our quoted uncertainties and favor a small value both for the electric and the magnetic radius of the proton. Our main findings and conclusions are presented in the companion letter [50].

This paper provides the full details of our calculation and is organized as follows: Sec. II describes our lattice setup and computational details, as well as the extraction of the effective form factors from our lattice observables, while Sec. III is dedicated to the treatment of excited states. In Sec. IV, a comprehensive account of the parametrization of the Q^2 dependence of the form factors and their extrapolation to the physical point is presented. Section V discusses the model average and our final results, and Sec. VI draws some conclusions. Details on our treatment of the pion and nucleon masses relevant to the analysis are contained in Appendix A. Additional crosschecks on our excited-state analysis can be found in Appendix B, and a closer examination of the form factors on our near-physical pion mass ensemble in Appendix C. For completeness and ease of reference, we provide tables of all computed form factors in Appendix D, of the results of all direct BχPT fits in Appendix E, of the radii and magnetic moments extracted using z-expansion fits in Appendix F, and of their extrapolation to the physical point in Appendix G.

II. LATTICE SETUP

To compute the electromagnetic form factors of the nucleon, we consider the vector current insertion for quark flavor f,

$$V_f^\mu(x) = \bar{\Psi}_f(x)\gamma^\mu\Psi_f(x), \tag{1}$$

and its nucleon matrix elements,

$$\langle N(\mathbf{p}', s')|V_f^\mu(x)|N(\mathbf{p}, s)\rangle = e^{iq\cdot x}\bar{u}^{s'}(\mathbf{p}')\mathcal{V}_f^\mu(q)u^s(\mathbf{p}). \tag{2}$$

Here, $N(\mathbf{p}, s)$ denotes a nucleon state with three-momentum $\mathbf{p}$ and spin s, $u^s(\mathbf{p})$ the corresponding Dirac spinor, and $q_\mu = p'_\mu - p_\mu$ the four-momentum transfer. The quantities $\mathcal{V}_f^\mu(q)$ are defined by

$$\mathcal{V}_f^\mu(q) = \gamma^\mu F_1^f(Q^2) + i\frac{\sigma^{\mu\nu}q_\nu}{2m_N}F_2^f(Q^2), \tag{3}$$

TABLE I. Overview of the ensembles used in this study. $N_{\mathrm{meas,HP}}$ and $N_{\mathrm{meas,LP}}$ denote the aggregated number of high-precision (HP) and low-precision (LP) solves used for the computation of the connected and the disconnected contributions, respectively. For the connected contribution, $N_{\mathrm{meas}}^{\mathrm{conn,max}}$ refers to the number of measurements used for the largest value of t_{sep}, while for the smaller values, the number of measurements is scaled down in stages.

ID	β	t_0^{sym}/a^2	T/a	L/a	M_π [MeV]	$N_{\mathrm{cfg}}^{\mathrm{conn}}$	$N_{\mathrm{cfg}}^{\mathrm{disc}}$	$N_{\mathrm{meas,HP}}^{\mathrm{conn,max}}$	$N_{\mathrm{meas,LP}}^{\mathrm{conn,max}}$	$N_{\mathrm{meas,HP}}^{\mathrm{disc}}$	$N_{\mathrm{meas,LP}}^{\mathrm{disc}}$	t_{sep}/a
C101	3.40	2.860(11)	96	48	227	1988	994	1988	63 616	7 951	237 965	4–17
N101[a]	3.40	2.860(11)	128	48	283	1588	1588	1588	50 816	3 176	406 518	4–17
H105[a]	3.40	2.860(11)	96	32	283	1024	1024	4096	49 152	25 585	248 331	4–17
D450	3.46	3.659(16)	128	64	218	498	498	3984	63 744	3 984	63 744	4–20
N451[a]	3.46	3.659(16)	128	48	289	1010	1010	8080	129 280	8 080	129 280	4–20 (stride 2)
E250	3.55	5.164(18)	192	96	130	398	796	3184	101 888	6 368	203 776	4–22 (stride 2)
D200	3.55	5.164(18)	128	64	207	1996	998	1996	63 872	8 982	271 258	4–22 (stride 2)
N200[a]	3.55	5.164(18)	128	48	281	1708	1708	1708	22 828	13 664	406 016	4–22 (stride 2)
S201[a]	3.55	5.164(18)	128	32	295	2092	2092	2092	66 944	4 181	96 279	4–22 (stride 2)
E300	3.70	8.595(29)	192	96	176	569	569	569	18 208	1 138	163 872	4–28 (stride 2)
J303	3.70	8.595(29)	192	64	266	1073	1073	1073	17 168	3 219	145 872	4–28 (stride 2)

[a]These ensembles are not used in the final fits but only to constrain discretization and finite-volume effects.

where m_N is the nucleon mass, and $Q^2 = -q^2 > 0$ in the spacelike region. Furthermore, we have introduced the Dirac and Pauli form factors $F_1(Q^2)$ and $F_2(Q^2)$, respectively, which are connected to the electric and magnetic Sachs form factors $G_E(Q^2)$ and $G_M(Q^2)$ via

$$G_E(Q^2) = F_1(Q^2) - \frac{Q^2}{4m_N^2} F_2(Q^2), \tag{4}$$

$$G_M(Q^2) = F_1(Q^2) + F_2(Q^2). \tag{5}$$

The electric form factor at zero momentum transfer yields the nucleon's electric charge, i.e., $G_E^p(0) = 1$ and $G_E^n(0) = 0$, whereas the magnetic form factor at zero momentum transfer is identified with the magnetic moment, $G_M(0) = \mu_M$. The corresponding radii are given by the derivative of the form factors at zero momentum transfer,

$$\langle r^2 \rangle = -\frac{6}{G(0)} \frac{\partial G(Q^2)}{\partial Q^2}\bigg|_{Q^2=0}. \tag{6}$$

The only exception to this definition is the electric radius of the neutron, where the normalization factor is omitted,

$$\langle r_E^2 \rangle^n = -6 \frac{\partial G_E^n(Q^2)}{\partial Q^2}\bigg|_{Q^2=0}. \tag{7}$$

For our lattice determination of these quantities, we use the CLS ensembles [49] which have been generated with $2+1$ flavors of nonperturbatively $\mathcal{O}(a)$-improved Wilson fermions [51,52] and a tree-level improved Lüscher-Weisz gauge action [53]. Only ensembles following the chiral trajectory characterized by $\mathrm{tr}M_q = 2m_l + m_s = \mathrm{const}$ are employed. In order to prevent topological freezing [54], the fields obey open boundary conditions (oBC) in time [55,56], with the exception of the ensembles E250, D450, and N451, which use periodic boundary conditions in time. Table I displays the set of ensembles entering the analysis: they cover four lattice spacings in the range from 0.050 fm to 0.086 fm, and several different pion masses, including one slightly below the physical value (E250). We note that data is available on additional (heavier) ensembles, but only the ones shown in Table I are included in this analysis.

In order to compensate for the twisted mass introduced for the light quarks [56,57] and the rational approximation used for the dynamical strange quark [58,59] during the gauge field generation, all observables need to be reweighted. We employ the reweighting factors computed in Ref. [60] with exact low-mode deflation on all ensembles except E300, where the standard stochastic CLS run [49] is used. In all cases, we correct for the treatment of the strange-quark determinant following the procedure outlined in Ref. [61].

We measure the two- and three-point functions of the nucleon,

$$\langle C_2(\mathbf{p}'; t_{\mathrm{sep}}) \rangle = \sum_{\mathbf{y}} e^{-i\mathbf{p}'\cdot\mathbf{y}} \Gamma^p_{\beta\alpha} \langle N_\alpha(\mathbf{y}, t_{\mathrm{sep}}) \bar{N}_\beta(0) \rangle, \tag{8}$$

$$\langle C_{3,O}(\mathbf{p}', \mathbf{q}; t_{\mathrm{sep}}, t) \rangle = \sum_{\mathbf{y},\mathbf{z}} e^{i\mathbf{q}\cdot\mathbf{z}} e^{-i\mathbf{p}'\cdot\mathbf{y}} \Gamma^p_{\beta\alpha} \langle N_\alpha(\mathbf{y}, t_{\mathrm{sep}}) O(\mathbf{z}, t) \bar{N}_\beta(0) \rangle. \tag{9}$$

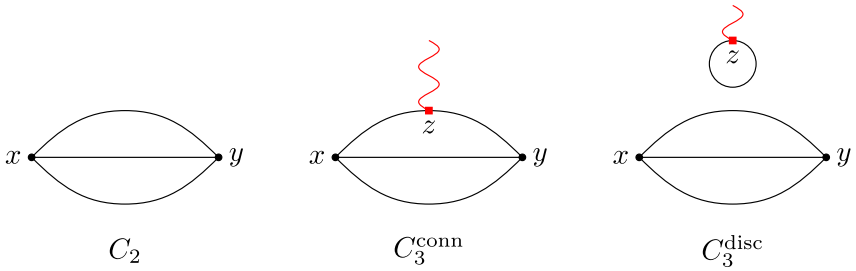

FIG. 1. Diagrammatic representation of the two- and three-point functions of the nucleon. Only quark lines are shown, while all gluon lines are suppressed. The red squares in the three-point functions represent the operator insertion, and the wavy red lines the external photons.

Here, Γ^p denotes the polarization matrix of the nucleon and we have set the source position x to zero for simplicity. In our setup, the nucleon at the sink is at rest, i.e., for a momentum transfer $\mathbf{q}$ the initial and final states have momenta $\mathbf{p} = -\mathbf{q}$ and $\mathbf{p}' = \mathbf{0}$, respectively. Our interpolating operator for the proton is the same as in Refs. [47,62,63], which is built using Gaussian-smeared [64] quark fields with spatially APE-smeared [65] gauge links and tuning the parameters so that a smearing radius $r_G \approx 0.5$ fm [66] is realized.

For the three-point functions (9), the pertinent Wick contractions yield a connected and a disconnected contribution, $\langle C_{3,O}\rangle = \langle C_{3,O}^{\mathrm{conn}}\rangle + \langle C_{3,O}^{\mathrm{disc}}\rangle$. They are depicted diagrammatically in Fig. 1. To calculate the connected part, we employ the "fixed-sink" variant of the extended propagator method. This requires additional inversions for each source-sink separation while allowing the momentum transfer to be varied via a phase factor at the point of the current insertion [67]. The disconnected part of the three-point functions is constructed from the quark loops and the two-point functions according to

$$\langle C_{3,O}^{\mathrm{disc}}(\mathbf{p}', \mathbf{q}; t_{\mathrm{sep}}, t)\rangle = \langle L^{O,\mathrm{disc}}(\mathbf{q}; t) C_2(\mathbf{p}'; t_{\mathrm{sep}})\rangle, \tag{10}$$

$$L^{O,\mathrm{disc}}(\mathbf{q}; z_0) = -\sum_{\mathbf{z}} e^{i\mathbf{q}\cdot\mathbf{z}} \mathrm{tr}[D_q^{-1}(z, z)\Gamma^O]. \tag{11}$$

The all-to-all propagator $D_q^{-1}(z, z)$ appearing in the quark loops Eq. (11) is computed via stochastic estimation using a variation of the frequency-splitting technique [68]. To that end, we employ a generalized hopping-parameter expansion [69] combined with hierarchical probing [70] for one heavy quark flavor and subsequently apply a split-even estimator, i.e., the one-end trick [68,71,72], for the remaining flavors. For further details, we refer the interested reader to Ref. [73].

To reduce the cost of the inversions, we apply the truncated-solver method [74–76] with bias correction. Details on our setup of sources are contained in Table I, alongside the available source-sink separations t_{sep}. On ensembles with open boundary conditions in time, the sources are generally placed on a single timeslice in the middle of the lattice. Additional measurements of the two-point function are used on all oBC ensembles except S201 to extend the statistics for the disconnected contribution. For these additional measurements, we put the nucleon sources on different timeslices in the bulk of the lattice. We have checked explicitly that the observables studied in this work are not significantly influenced by boundary effects for the chosen source positions. No such issues arise for ensembles with periodic boundary conditions in time. Here, one can distribute the sources randomly on edges of subblocks of the entire lattice volume, as dictated by even-odd [77] and Schwarz [78] preconditioning. On all ensembles, we employ iterative statistics for the different source-sink separations. This means that with rising t_{sep}, the number of sources used for the computation of the connected part is increased. The scaling of measurements is tuned in such a way that the behavior of the effective statistics as a function of t_{sep} more closely resembles a constant instead of showing an exponential decay of the signal-to-noise ratio. For the disconnected part, the highest statistics at our disposal is always utilized, in order to obtain the best possible signal.

Instead of the local current Eq. (1), we use the conserved vector current in the same way as in Ref. [47], so that no renormalization is required. The $\mathcal{O}(a)$ improvement is also performed analogously to Ref. [47], with the improvement coefficient computed in Ref. [79].

As a first step towards extracting the effective form factors, the nucleon two-point functions from Eq. (8) are averaged over equivalent momentum classes. We call all three-momenta $\mathbf{p}$ which share the same modulus $|\mathbf{p}|$ equivalent and assign them the equivalence class $\mathfrak{p} = \{\tilde{\mathbf{p}} \in \mathbb{P}^3 : |\tilde{\mathbf{p}}| = |\mathbf{p}|\}$. Here, $\mathbb{P}^3$ is the set of possible lattice momenta, $\mathbb{P}^3 = \{\mathbf{p} = \frac{2\pi}{L}\mathbf{n}_p : \mathbf{n}_p \in \mathbb{Z}^3\} \subset \mathbb{R}^3$. The momentum-averaged two-point functions are then defined as

$$\langle \bar{C}_2(\mathfrak{p}; t_{\mathrm{sep}})\rangle = \sum_{\tilde{\mathbf{p}}\in\mathfrak{p}} \langle C_2(\tilde{\mathbf{p}}; t_{\mathrm{sep}})\rangle \Big/ \sum_{\tilde{\mathbf{p}}\in\mathfrak{p}} 1. \tag{12}$$

Afterwards, we calculate the ratios [80]

$$R_{V_\mu}(\mathbf{0},\mathbf{q};t_{\mathrm{sep}},t)=\frac{\langle C_{3,V_\mu}(\mathbf{0},\mathbf{q};t_{\mathrm{sep}},t)\rangle}{\langle C_2(\mathbf{0};t_{\mathrm{sep}})\rangle}\sqrt{\frac{\langle\bar{C}_2(\mathbf{q};t_{\mathrm{sep}}-t)\rangle\langle C_2(\mathbf{0};t)\rangle\langle C_2(\mathbf{0};t_{\mathrm{sep}})\rangle}{\langle C_2(\mathbf{0};t_{\mathrm{sep}}-t)\rangle\langle\bar{C}_2(\mathbf{q};t)\rangle\langle\bar{C}_2(\mathbf{q};t_{\mathrm{sep}})\rangle}}. \tag{13}$$

For the connected part, we employ for each value of t_{sep} matching statistics in terms of sources for the two- and three-point functions entering Eq. (13). This preserves the full correlation between them, which slightly reduces the statistical fluctuations in the ratio. For the disconnected part, on the other hand, the highest statistics at our disposal is utilized for all values of t_{sep}, both for the two-point functions used to construct Eq. (10) and for the ones entering Eq. (13). In all cases, the same projection matrix is employed for both the two- and three-point functions entering Eq. (13), again to ensure full correlation. For the connected part, this is only $\Gamma_3^p=\frac{1}{2}(1+\gamma_0)(1+i\gamma_5\gamma_3)$. For the disconnected part, we employ all three polarization directions, $\Gamma_j^p=\frac{1}{2}(1+\gamma_0)(1+i\gamma_5\gamma_j)$, $j=1,\ 2,\ 3$, and average the thus obtained effective form factors. Moreover, we average over the forward- and backward-propagating nucleon for the disconnected part. For the determination of the nucleon mass (*cf.* Appendix A), we make use of the unpolarized nucleon, i.e., $\Gamma^p=\frac{1}{2}(1+\gamma_0)$, as this is equivalent to averaging over the three polarization directions in the case of the two-point function.

We use the same estimators for the effective electric and magnetic Sachs form factors as in Ref. [47], i.e., we do not employ the spatial components of the vector current to compute the electric form factor, as they are more noisy. Note that for the disconnected contribution to the effective magnetic form factor, one needs to adapt the indices of the momenta and the current insertions in Eq. (11) of Ref. [47] according to the polarization direction. We average these estimators over all three-momenta $\tilde{\mathbf{q}}$ belonging to the equivalence class $\mathbf{q}$ and thus yielding the same Q^2 [except for those with $\tilde{q}_1=\tilde{q}_2=0$ (or the components appropriate for Γ_j^p) in the case of the magnetic form factor]. Furthermore, we assume the relativistic dispersion relation $E_{\mathbf{q}}=\sqrt{m_N^2+|\mathbf{q}|^2}$. We have checked explicitly that employing the extracted ground-state energies also for nonvanishing momenta instead of the above dispersion relation does not change our results for the ground-state form factors significantly.

We build the effective form factors in the isospin basis, i.e., for the isovector $(u-d)$ and the connected isoscalar $(u+d)$ combinations, as well as for the disconnected contributions of the light and strange quarks. Since we impose strong SU(2) isospin symmetry ($m_u=m_d$) in our calculation, the disconnected contribution cancels in the isovector case. The full isoscalar (octet) combination $u+d-2s$, on the other hand, can be obtained from the connected and disconnected pieces as

$$G_{E,M}^{\mathrm{eff},u+d-2s}=G_{E,M}^{\mathrm{eff,conn},u+d}+2G_{E,M}^{\mathrm{eff,disc},l-s}. \tag{14}$$

Note that the disconnected part only requires the difference $l-s$ between the light and strange contributions, in which correlated noise cancels and which can be computed very effectively by the one-end trick. We drop the disconnected contribution $G_E^{\mathrm{eff,disc},l-s}$ at $Q^2=0$, as it has to be zero. Our data, on the other hand, shows fluctuations around the exact zero due to the stochastic estimation of the quark loops and the application of the truncated-solver method for the calculation of the two-point functions. Thus, explicitly adding this superfluous term, which is always compatible with zero, would artificially enhance noise in all data points for G_E, because we normalize them by $G_E(0)$ (*cf.* Sec. IV).

The resulting isoscalar effective form factors are shown in Fig. 2 for the first nonvanishing momentum on the ensemble E300. This illustrates that we obtain a clear signal including the disconnected contributions: the families of points for the different source-sink separations can be clearly distinguished in $G_E^{\mathrm{eff},u+d-2s}$, and for the smaller values of t_{sep} also in $G_M^{\mathrm{eff},u+d-2s}$.

Unless otherwise stated, errors are estimated using single-elimination jackknife. Autocorrelations are largely absent in the ratios of Eq. (13). Nevertheless, in order to remove any residual autocorrelation, we block our data with a bin size of two, if the spacing between two analyzed configurations in terms of molecular dynamics time does not already account for this factor. The latter is the case for the disconnected contribution on C101 and D200, for the connected contribution on E250, and for both the connected and the disconnected contributions on E300 and J303.

On some ensembles, we observe that individual measurements on a small number of configurations are located very far outside the distribution of the vast majority of configurations. Keeping these exceptional configurations in the sample leads to a drastically increased error and, more importantly, to an unexpected scaling of the error with the source-sink separation, i.e., the error is inflated strongly only for single values of t_{sep}. The most prominent example is D200, where we identify one configuration to be the root cause of the gross overestimation of errors. Similar observations of outliers have already been reported for previous analyses on CLS ensembles [63,81]. In order to identify the problematic configurations, we first extract the effective form factors using single-elimination jackknife on unbinned data. We then scan the isovector, connected isoscalar, and disconnected contributions for all relevant

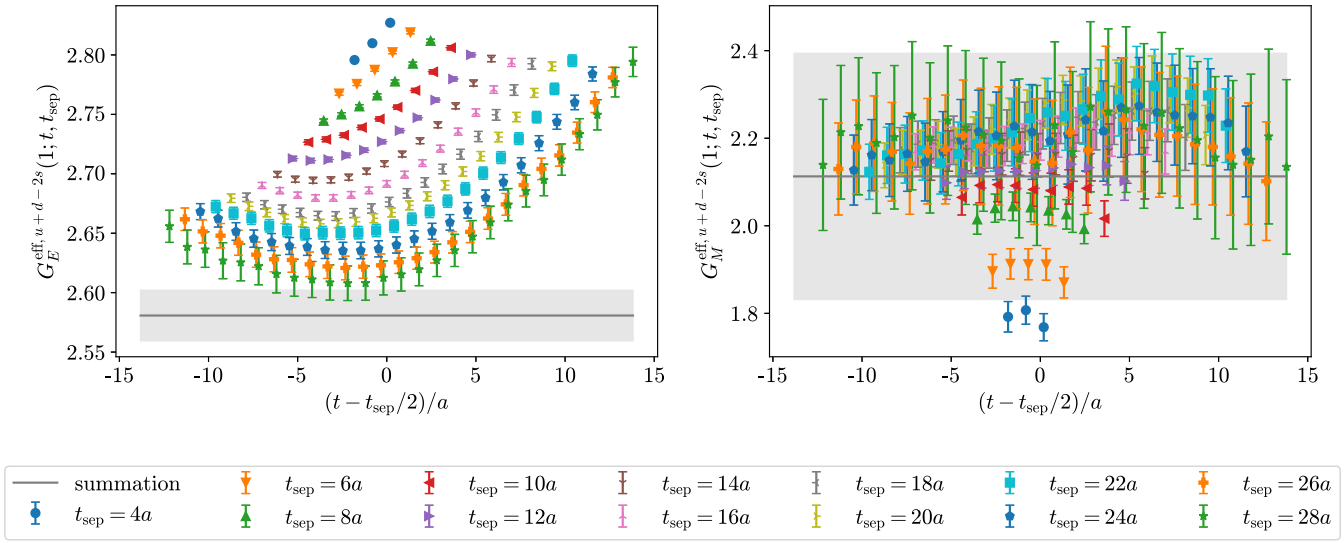

FIG. 2. Isoscalar effective form factors at the first nonvanishing momentum on the ensemble E300 ($Q^2 \approx 0.067$ GeV^2). The left plot shows the electric and the right one the magnetic form factor. For each source-sink separation t_{sep}, the effective form factors are displayed as a function of the operator insertion time t, offset to the midpoint between nucleon source and sink. The data points are horizontally displaced for better visibility. The gray bands and curves depict the results of the summation method using the window average, as detailed in Sec. III.

values of Q^2, t_{sep}, and t, employing the procedure described in the supplementary material of Ref. [63]. The corresponding configurations are omitted during the whole main analysis; the numbers in Table I already reflect this.

We express all dimensionful quantities in units of t_0 using the determination of t_0^{sym}/a^2 from Ref. [82]. Only our final results for the radii are converted to physical units by means of the world-average value of

$$\sqrt{t_{0,\mathrm{phys}}} = 0.14464(87)\ \mathrm{fm} \tag{15}$$

for $N_f = 2+1$ from Ref. [83]. This procedure ensures that the error of the calibration is treated independently of that of the (more precise) pure lattice measurement of t_0^{sym}/a^2.

III. EXCITED-STATE ANALYSIS

In general, baryonic correlation functions suffer from a strong exponential growth of the relative statistical noise when the distance in Euclidean time between operators is increased [84,85]. Therefore, for the typically accessible source-sink separations in current lattice calculations of baryon structure observables, it cannot be guaranteed that contributions from excited states are sufficiently suppressed. This underlines the necessity to explicitly address the excited-state systematics in order to extract the ground-state form factors from the effective ones [83,86].

In this work, we make use of the summation method [87–89]. It takes advantage of the fact that in the ratios of Eq. (13), when summed over timeslices in between source and sink, the contributions from excited states are parametrically suppressed. Accordingly, we sum the effective form factors over the operator insertion time, omitting $t_{\mathrm{skip}} = 2a$ timeslices at both ends,[1]

$$S_{E,M}(Q^2;t_{\mathrm{sep}}) = \sum_{t=t_{\mathrm{skip}}}^{t_{\mathrm{sep}}-t_{\mathrm{skip}}} G_{E,M}^{\mathrm{eff}}(Q^2;t_{\mathrm{sep}},t). \tag{16}$$

In the asymptotic limit with only ground-state contributions, the slope of this quantity as a function of t_{sep} is given by the ground-state form factor [40,47],

$$\begin{aligned} S_{E,M}(Q^2;t_{\mathrm{sep}}) \overset{t_{\mathrm{sep}}\gg 0}{\longrightarrow}\ & C_{E,M}(Q^2) \\ & + \frac{1}{a}(t_{\mathrm{sep}} + a - 2t_{\mathrm{skip}})G_{E,M}(Q^2) \\ & + \ldots, \end{aligned} \tag{17}$$

where the ellipsis denotes exponentially suppressed corrections from excited states.

We perform several fits to Eq. (17) for different starting values $t_{\mathrm{sep}}^{\mathrm{min}}$ of the source-sink separation. Instead of choosing a single value of $t_{\mathrm{sep}}^{\mathrm{min}}$ on each ensemble, we perform a weighted average over $t_{\mathrm{sep}}^{\mathrm{min}}$, where the weights are given by a smooth window function [62,63],

$$\hat{G} = \frac{\sum_i w_i G_i}{\sum_i w_i}, \quad w_i = \tanh\frac{t_i - t_w^{\mathrm{low}}}{\Delta t_w} - \tanh\frac{t_i - t_w^{\mathrm{up}}}{\Delta t_w}. \tag{18}$$

[1]We justify this choice in Appendix B.

Here, t_i is the value of $t_{\mathrm{sep}}^{\mathrm{min}}$ in the ith fit, and we choose $t_w^{\mathrm{low}} = 6.22\sqrt{t_0} \approx 0.9$ fm, $t_w^{\mathrm{up}} = 7.61\sqrt{t_0} \approx 1.1$ fm, and $\Delta t_w = 0.553\sqrt{t_0} \approx 0.08$ fm. Note that the window has been shifted to larger values of $t_{\mathrm{sep}}^{\mathrm{min}}$ by 0.1 fm compared to the one originally used in Refs. [62,63]. The reason for this is that our data for the electromagnetic form factors are statistically more precise than those for the axial form factor in Ref. [62] or the sigma term in Ref. [63]. Hence, we can resolve excited-state effects for larger values of $t_{\mathrm{sep}}^{\mathrm{min}}$, so that the plateau region is expected to start later. Accordingly, we have observed that the window using larger $t_w^{\mathrm{up,low}}$ better captures the plateau on the majority of our ensembles. Thus, we have opted for the more conservative choice, which also yields a slightly larger error. The two choices are compared in Fig. 9 in Appendix B.

We average over all available values of $t_{\mathrm{sep}}^{\mathrm{min}}$, subject to the constraint that at least three values of t_{sep} are contained in the underlying fit to Eq. (16). It should be stressed that the only quantity that is effectively restricted by this method is the minimal source-sink separation; all fits go up to the largest t_{sep} we have computed. Essentially, the window average merely serves as a smoothing of the lower end of the fit interval.

This strategy is illustrated in Fig. 3 for the isoscalar combination at the first nonvanishing momentum on the ensembles D450 and E300. One can see that the window averages agree within their errors with what one might identify as plateaux in the blue points. This being valid to a similar degree for all other ensembles, flavor combinations, and momenta employed in the analysis, we conclude that the window method reliably identifies the asymptotic value of the effective form factors. Moreover, it reduces the human bias compared to manually picking one particular value for $t_{\mathrm{sep}}^{\mathrm{min}}$ on each ensemble, since we use the same window parameters in units of t_0 on all ensembles. It is important to note that even if a plateau appears to be reached, this does not guarantee ground-state dominance. The situation is aggravated by the fact that in general, relatively few values of $t_{\mathrm{sep}}^{\mathrm{min}}$ are available, and correlated fluctuations in any direction can easily be mistaken for a plateau. This underlines once more the necessity of an automated strategy such as the window average which can readily be applied to all ensembles and momenta. The size

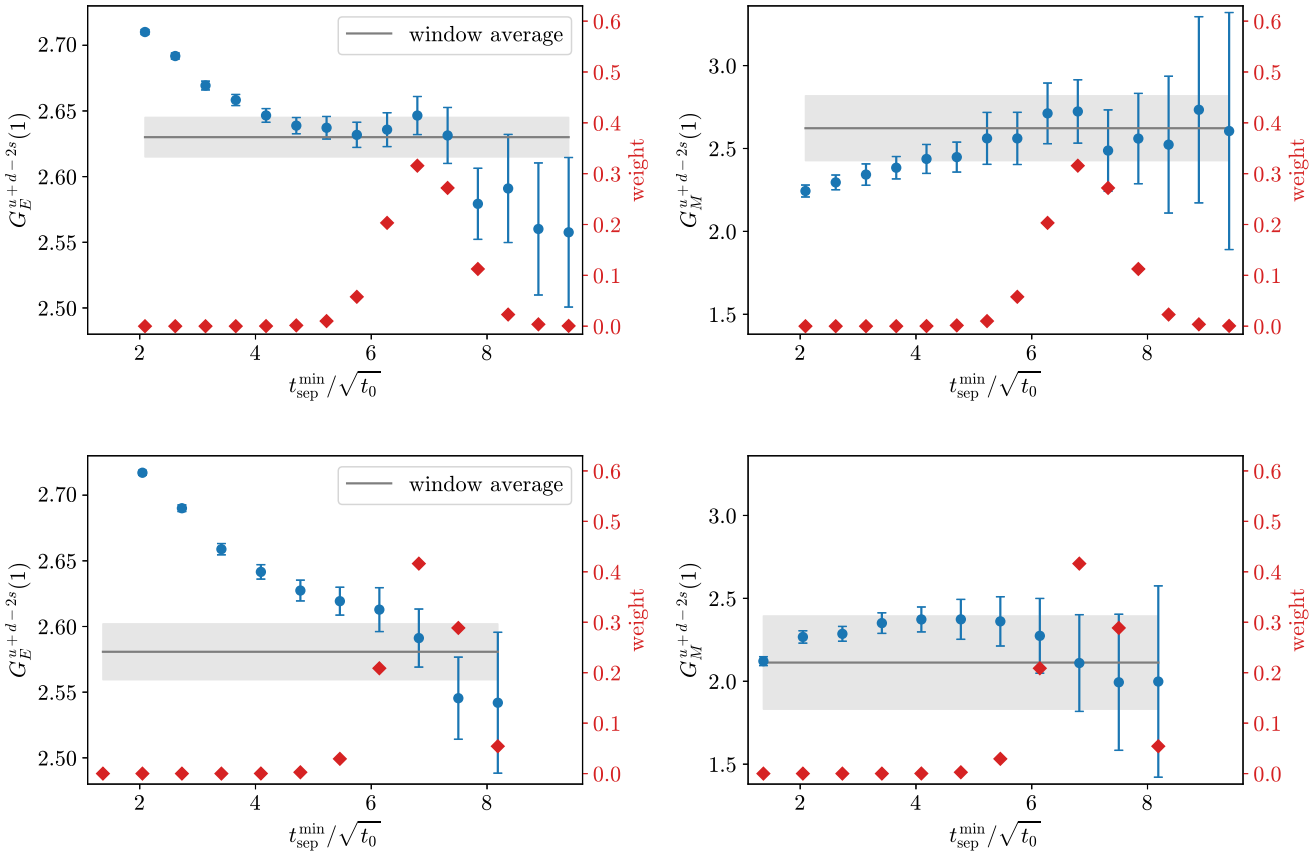

FIG. 3. Isoscalar electromagnetic form factors at the first nonvanishing momentum on ensembles D450 (upper panel) and E300 (lower panel) as a function of the minimal source-sink separation entering the fits to Eq. (16). Each blue point represents a single fit starting at the source-sink separation given on the horizontal axis. The associated weights derived from Eq. (18) are shown by the red diamonds, with the gray lines and bands depicting the averaged results.

of the gray error bands in Fig. 3 furthermore shows that our window average yields, in contrast to error-weighted procedures, an error estimate which is comparable to the errors of the individual points entering the average. Thus, we are convinced that our error estimates are conservative enough to exclude any systematic bias in the identification of ground-state form factors.

In order to ensure that ground-state dominance is reached by the method described above, we have explored additional variations of it as well as a complementary approach based on two-state fits to the effective form factors. Details on these crosschecks can be found in Appendix B. The form factor values obtained by our preferred method are collected in Appendix D for all ensembles and all momenta which we have considered.

IV. PARAMETRIZATION OF THE Q^2 DEPENDENCE

As the radii are defined in terms of the slope of the form factors at zero momentum transfer [*cf.* Eq. (6)], a description of their Q^2 dependence is necessary. Proceeding analogously to Refs. [40,47], we apply two different methods: Our preferred strategy is to combine the parametrization of the Q^2 dependence with the chiral, continuum, and infinite-volume extrapolation by performing a simultaneous fit to the Q^2-, pion-mass, lattice-spacing, and finite-volume dependence of our form factor data directly to the expressions resulting from covariant baryon chiral perturbation theory (BχPT) [90]. This is explained in detail in Sec. IV A. Alternatively, one can follow the more traditional approach of first extracting the radii on each ensemble from a generic parametrization of the Q^2 dependence and subsequently extrapolating them to the physical point. A crosscheck of our main analysis with this two-step procedure is presented in Sec. IV B.

A. Direct BχPT fits

For our main analysis using the direct (simultaneous) fits, we fit our data for the form factors to the full expressions of Ref. [90] without explicit Δ degrees of freedom. The fits are performed for the isovector and isoscalar channels separately, but for G_E and G_M together. This allows us to take the correlations not only between different Q^2, but also between G_E and G_M into account. The ensembles, on the other hand, are treated as statistically independent. $G_E(0)$ is fixed by fitting the normalized ratio $G_E(Q^2)/G_E(0)$. We incorporate the contributions from the relevant vector mesons in the expressions for the form factors. In the isovector case, this is the ρ meson, while in the isoscalar channel, we include the leading-order terms from the ω and ϕ resonances. Because the loop diagrams involving ω or ϕ resonances only yield small numerical contributions to the form factors, our fits depend only marginally on them. This means that the corresponding low-energy constants (LECs) g_ω and g_ϕ are very poorly constrained by our data, so that we neglect these loop diagrams. The corresponding tree-level diagrams, on the other hand, only depend on the combinations $c_\omega = f_\omega g_\omega$ and $c_\phi = f_\phi g_\phi$, respectively [90]. Thus, we only use the products c_ω and c_ϕ as independent fit parameters. To summarize, the fit for the isoscalar form factors depends linearly on the LECs d_7, c_7, c_ω, and c_ϕ, whereas for the isovector form factors, the relevant LECs are d_6, $\tilde{c}_6$, d_x, and G_ρ [90].[2] For further details on the LECs, we refer to Table III in Ref. [40]. The full expressions for the form factors which we employ can be found in Appendix D 2 1 of Ref. [97]. Starting from the formulae for the Dirac and Pauli form factors given there, we form the appropriate linear combinations for the electric and magnetic Sachs form factors according to Eqs. (4) and (5).

The mass of the ρ meson is set on each ensemble to the value at the corresponding pion mass and lattice spacing. This is determined from a parametrization of the pion-mass and lattice-spacing dependence of a subset of the values for M_ρ/M_π obtained in Ref. [73],

$$\frac{M_\rho}{M_\pi} = \frac{M_{\rho,\mathrm{phys}}}{M_{\pi,\mathrm{phys}}} + A\left(\frac{1}{\sqrt{t_0}M_\pi} - \frac{1}{\sqrt{t_{0,\mathrm{phys}}}M_{\pi,\mathrm{phys}}}\right) + C(\sqrt{t_0}M_\pi - \sqrt{t_{0,\mathrm{phys}}}M_{\pi,\mathrm{phys}}) + D\frac{a^2}{t_0}, \tag{19}$$

with the independent fit parameters A, C, and D. For the fit to this formula, we disregard ensembles which are not included in our main analysis (*cf.* Table I), or which are solely used to study finite-volume effects (H105 and S201), since the finite-volume dependence of the ρ masses is not sufficiently constrained by the data. On each ensemble, we set the ω mass equal to the ρ mass obtained from Eq. (19), because no lattice data for the ω masses on our ensembles are available, and the mass splitting between the ρ and ω mesons is small. This means that the true ω mass on our ensembles is probably much closer to the ensemble-dependent ρ mass than to the physical value of the ω mass.[3] The physical pion mass $M_{\pi,\mathrm{phys}}$ is fixed in units of $\sqrt{t_0}$ using its value in the isospin limit [98],

[2]The nucleon (average of the proton and neutron) and ϕ masses are fixed to their physical values [91]. Moreover, we replace the pion decay constant and the axial-vector coupling constant in the chiral limit, which appear in the BχPT formulas, by their physical values, $F_\pi = 92.2$ MeV [82] and $g_A = 1.2754$ [91], respectively. We also use the KSRF relation [92–94] $g^2 = M^2_{\rho,\mathrm{phys}}/(2F^2_\pi)$. For the numerical evaluation of one-loop integrals, we make use of LoopTools [95,96], setting the renormalization scale to $\mu = 1$ GeV.

[3]The ϕ resonance, on the other hand, is much heavier than the ρ and ω mesons. In the absence of lattice data for the ϕ mass on our ensembles, we thus employ the physical value $M_{\phi,\mathrm{phys}}$ [91] in our fits.

$$M_{\pi,\mathrm{phys}} = M_{\pi,\mathrm{iso}} = 134.8(3)\ \mathrm{MeV}, \tag{20}$$

i.e., we employ $\sqrt{t_{0,\mathrm{phys}}}M_{\pi,\mathrm{phys}} = 0.09881(59)$. Here, we neglect the uncertainty of $M_{\pi,\mathrm{iso}}$ in MeV since it is completely subdominant compared to that of $\sqrt{t_{0,\mathrm{phys}}}$, which enters in the unit conversion and is propagated into the fits (see below). For the pion masses we use on our ensembles, see Appendix A.

Two of the major benefits of the approach presented in this subsection as compared to the two-step procedure described in the next one are the following: On the one hand, performing a fit across several ensembles significantly decreases the errors on the resulting radii. On the other hand, it leads to a much larger number of degrees of freedom for the fit. This increases the stability against lowering the applied momentum cut considerably. These advantages have already been noticed in our publication on the isovector electromagnetic form factors, Ref. [47], and apply in a similar manner to the data presented in this paper.

We perform several such fits, using different models to describe the lattice-spacing and/or finite-volume dependence and, at the same time, applying various cuts in the pion mass ($M_\pi \leq 0.23$ GeV and $M_\pi \leq 0.27$ GeV) and momentum transfer ($Q^2 \leq 0.3, \ldots, 0.6$ GeV^2), in order to estimate the corresponding systematic uncertainties. The variations of the results due to the cuts are in most cases much smaller than their statistical errors. In any case, these variations will be included in our systematic errors by means of a model average (*cf.* Sec. V below). Moreover, the p values of all our direct fits remain on an acceptable level (*cf.* Appendix E). We conclude that we do not observe any sign of a breakdown of the BχPT expansions in the aforementioned range of pion masses and momentum transfers.

We adopt two different models for lattice artifacts, either based on an additive or a multiplicative *Ansatz* [47],

$$G_E^{\mathrm{add}}(Q^2) = G_E^{\chi}(Q^2) + G_E^a a^2 Q^2 + G_E^L t_0 Q^2 e^{-M_\pi L}, \tag{21}$$

$$G_M^{\mathrm{add}}(Q^2) = G_M^{\chi}(Q^2) + G_M^a \frac{a^2}{t_0} + \kappa_L M_\pi \left(1 - \frac{2}{M_\pi L}\right) e^{-M_\pi L} + G_M^L t_0 Q^2 e^{-M_\pi L}, \tag{22}$$

$$G_E^{\mathrm{mult}}(Q^2) = G_E^{\chi}(Q^2) + \frac{G_E^a a^2 Q^2 + G_E^L t_0 Q^2 e^{-M_\pi L}}{t_0(M_\rho^2 + Q^2)}, \tag{23}$$

$$G_M^{\mathrm{mult}}(Q^2) = G_M^{\chi}(Q^2) + \frac{G_M^a a^2/t_0 + G_M^L t_0 Q^2 e^{-M_\pi L}}{t_0(M_\rho^2 + Q^2)} + \kappa_L M_\pi \left(1 - \frac{2}{M_\pi L}\right) e^{-M_\pi L}. \tag{24}$$

The precise form of the multiplicative model has been altered compared to the one used in Ref. [47], where the correction terms directly multiplied $G_{E,M}^{\chi}(Q^2)$. With our updated, more precise data we have found that such terms containing both $G_{E,M}^{a,L}$ and the LECs [via $G_{E,M}^{\chi}(Q^2)$] lead to instabilities in the determination of $G_{E,M}^{a,L}$. This is most probably due to the fit becoming nonlinear in the fit parameters. By contrast, our new model in Eqs. (23) and (24) is, from a technical point of view, also purely additive and thus linear in the fit parameters, while still capturing the essential contribution of $G_{E,M}^{\chi}(Q^2)$ to the falloff of the form factors with rising momentum transfer.[4] Fits leaving κ_L as a free parameter are unstable, and we therefore fix κ_L to the value from heavy-baryon chiral perturbation theory [99],

$$\kappa_L = -\frac{m_{N,\mathrm{phys}} g_A^2}{4\pi F_\pi^2}\tau_3. \tag{25}$$

Here, $\tau_3 = +1$ for the proton and $\tau_3 = -1$ for the neutron. Following Eq. (D1), this implies that $\tau_3^{u-d} = +2$ and $\tau_3^{u+d-2s} = 0$. In total, we have seven different fit models: one without any parametrization of lattice artifacts, three including discretization and/or finite-volume effects with the additive model of Eqs. (21) and (22), and three corresponding ones using the multiplicative prescription of Eqs. (23) and (24). The results for all of them are collected in Appendix E.

The inclusion of a term describing lattice artifacts requires the use of Gaussian priors for the relevant coefficients to stabilize the fits. For this purpose, we first perform fits to ensembles at $M_\pi \approx 0.28$ GeV only (N101, H105, N451, N200, S201, and J303; *cf.* Table I). Here, we have relatively precise data in a wide range of lattice spacings and volumes. For these fits, we use a cut in Q^2 at 0.6 GeV^2 and a simultaneous description of the lattice-spacing and finite-volume dependence. The coefficients for the correction terms as determined from the fits, together with their associated errors, are then employed as priors for the final fits to the ensembles satisfying the aforementioned cuts in the pion mass. The only exception are the coefficients G_E^a parametrizing the lattice-spacing dependence of the isovector electric form factor: our data for G_E^{u-d} is sufficiently precise even at low pion masses to allow a determination of G_E^a, so that we can leave it as a free parameter.

Since the number of configurations and hence the number of jackknife samples differ between ensembles (*cf.* Table I), we use parametric bootstrap to resample the distributions on each ensemble. With all mean values for the form factors entering a specific fit, the nucleon and the pion mass, as well as their covariance matrix, we draw 10 000 random samples from a corresponding multivariate

[4]Note that because we employ M_ρ in place of M_ω on our ensembles, the expressions in Eqs. (23) and (24) are valid for the isovector and isoscalar channels alike.

Gaussian distribution. The covariance matrix one can build from these samples is consistent with the original covariance matrix. Moreover, the parametric bootstrap procedure enables us to account for the errors of the scale parameters t_0^{sym}/a^2 and $\sqrt{t_{0,\mathrm{phys}}}$, as well as M_ρ/M_π, which are external to this analysis. Hence, we create an independent random Gaussian distribution for $\sqrt{t_{0,\mathrm{phys}}}$, for t_0^{sym}/a^2 at each value of β, and for M_ρ/M_π on each ensemble.

From the fits in the isovector and isoscalar channels, we reconstruct the form factors and all derived observables for the proton and neutron. For this purpose, we build the appropriate linear combinations of the BχPT formulas and plug in the LECs as determined from the fits to the isovector and isoscalar form factors. This is the more natural approach both from the perspective of lattice QCD and of chiral perturbation theory: The form factors in the isospin basis are our primary[5] lattice observables, while the proton and neutron form factors can only be obtained indirectly as linear combinations of them [*cf.* Eq. (D1)]. For the BχPT fits, the isospin basis is also advantageous because of the clear separation of the contributing resonances in the isovector and isoscalar channels, so that there are no common fit parameters between the two of them.

The quality of the direct fits is illustrated in Fig. 4 for our two most chiral ensembles E250 and E300. The fits shown here correspond to the additive model of Eqs. (21) and (22) employed to parametrize discretization and finite-volume effects, with $M_{\pi,\mathrm{cut}} = 0.23$ GeV and $Q^2_{\mathrm{cut}} = 0.6$ GeV^2. In general, the fits describe the data very well. We observe that the error of the fits is significantly reduced compared to the data points on E250, but only slightly on E300. The latter is also the case on all other ensembles entering the displayed fits (D200, D450, and C101, which are not shown in Fig. 4). We conclude that the error reduction on E250 is due to the global fit, i.e., the inclusion of several ensembles in one fit, with the data at larger pion masses being more precise than near $M_{\pi,\mathrm{phys}}$.

For the electric form factors on E250, we find a slight deviation between the fit and the data, which is mostly absent in all other cases. Nevertheless, the p values of the shown fits are acceptable, with $p > 0.15$ in both channels, because the data points are highly correlated, so that actually fewer degrees of freedom deviate than it naively appears from the plots in Fig. 4. Also, the fits are more consistent with the data on most of the other ensembles. We take this as an indication that the form factors on E250 are more heavily affected by correlated statistical fluctuations which are not sufficiently suppressed by our choice of window parameters in the summation method. In Appendix C, we discuss this point in more detail, concluding that it is in fact not caused by residual excited-state contamination. Regarding the isovector form factors, the fact that the fit lies somewhat below the data for G_E^{u-d} and somewhat above for G_M^{u-d} on E250, but to a much lesser degree so on ensembles with heavier pion masses, has already been noticed in Ref. [47], and is qualitatively confirmed by this updated study.

Note that the curves shown in Fig. 4 only correspond to one specific model and are thus not be interpreted as our definitive results for the form factors. These can be found in Fig. 7 for the proton and neutron.

B. Crosscheck with z expansion

As an alternative to the direct fits, one can treat the parametrization of the Q^2 dependence and the chiral, continuum, and infinite-volume extrapolation as two separate steps. A model-independent description of the Q^2 dependence of the form factors can be achieved by the z expansion [100],

$$\frac{G_E(Q^2)}{G_E(0)} = \sum_{k=0}^{n} a_k z(Q^2)^k, \tag{26}$$

$$G_M(Q^2) = \sum_{k=0}^{n} b_k z(Q^2)^k, \tag{27}$$

with

$$z(Q^2) = \frac{\sqrt{\tau_{\mathrm{cut}} + Q^2} - \sqrt{\tau_{\mathrm{cut}} - \tau_0}}{\sqrt{\tau_{\mathrm{cut}} + Q^2} + \sqrt{\tau_{\mathrm{cut}} - \tau_0}}. \tag{28}$$

The parameter τ_0 (not to be confused with the gradient flow scale t_0, hence the slightly uncommon nomenclature) is the value of $-Q^2$ which is mapped to $z = 0$. In this work, we employ $\tau_0 = 0$. On each ensemble, we set $\tau_{\mathrm{cut}} = 9M_\pi^2$ for the isoscalar channel and $\tau_{\mathrm{cut}} = 4M_\pi^2$ for the remaining channels, respectively, where M_π is the pion mass on the respective ensemble (*cf.* Appendix A). For the purpose of the z-expansion analysis, we use the form factors of the proton and neutron obtained as described in Appendix D. In analogy to the direct fits, we fit the normalized ratio $G_E(Q^2)/G_E(0)$ and enforce the normalization by fixing $a_0 = 1$. For the exceptional case of the neutron, where $G_E^n(0) = 0$, we do not normalize $G_E^n(Q^2)$, exclude the point at $Q^2 = 0$, and set $a_0 = 0$.

Using the same strategy to set priors on the coefficients a_k and b_k as in our earlier publication Ref. [47], we observe with our updated, more precise data that such priors impose too strict constraints on the Q^2 behavior of the form factors. In particular, the fits with priors tend to follow more closely the data points at large Q^2 than those at low Q^2, which is undesirable for an extraction of the radii and the magnetic moment. Hence, we resort to fits without priors, going up to order $n = 2$. This represents a compromise between the fit

[5]The form factors in the isospin basis are also secondary quantities in the sense that they are functions of gauge averages due to the reweighting and the ratio method [*cf.* Eq. (13)].

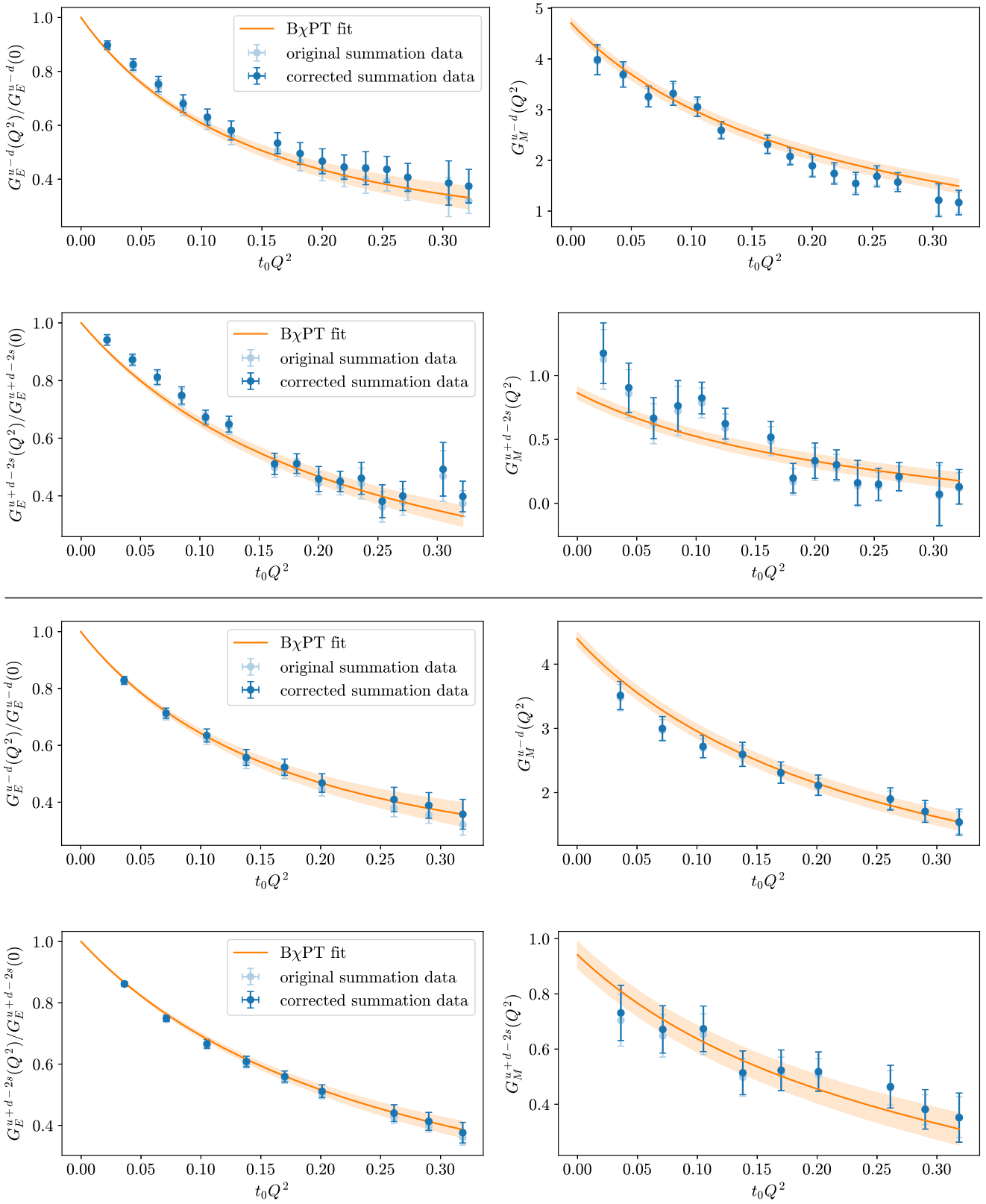

FIG. 4. Isovector and isoscalar electromagnetic form factors on the ensembles E250 (upper panel) and E300 (lower panel) as a function of Q^2. Our original lattice data as obtained from the summation method using the window average are represented by the faint blue points, while the opaque ones have been corrected for the continuum and infinite-volume limit. The orange curves and bands depict direct fits with $M_{\pi,\mathrm{cut}} = 0.23$ GeV and $Q^2_{\mathrm{cut}} = 0.6$ GeV^2, evaluated at the pion mass of the respective ensemble, zero lattice spacing, and infinite volume.

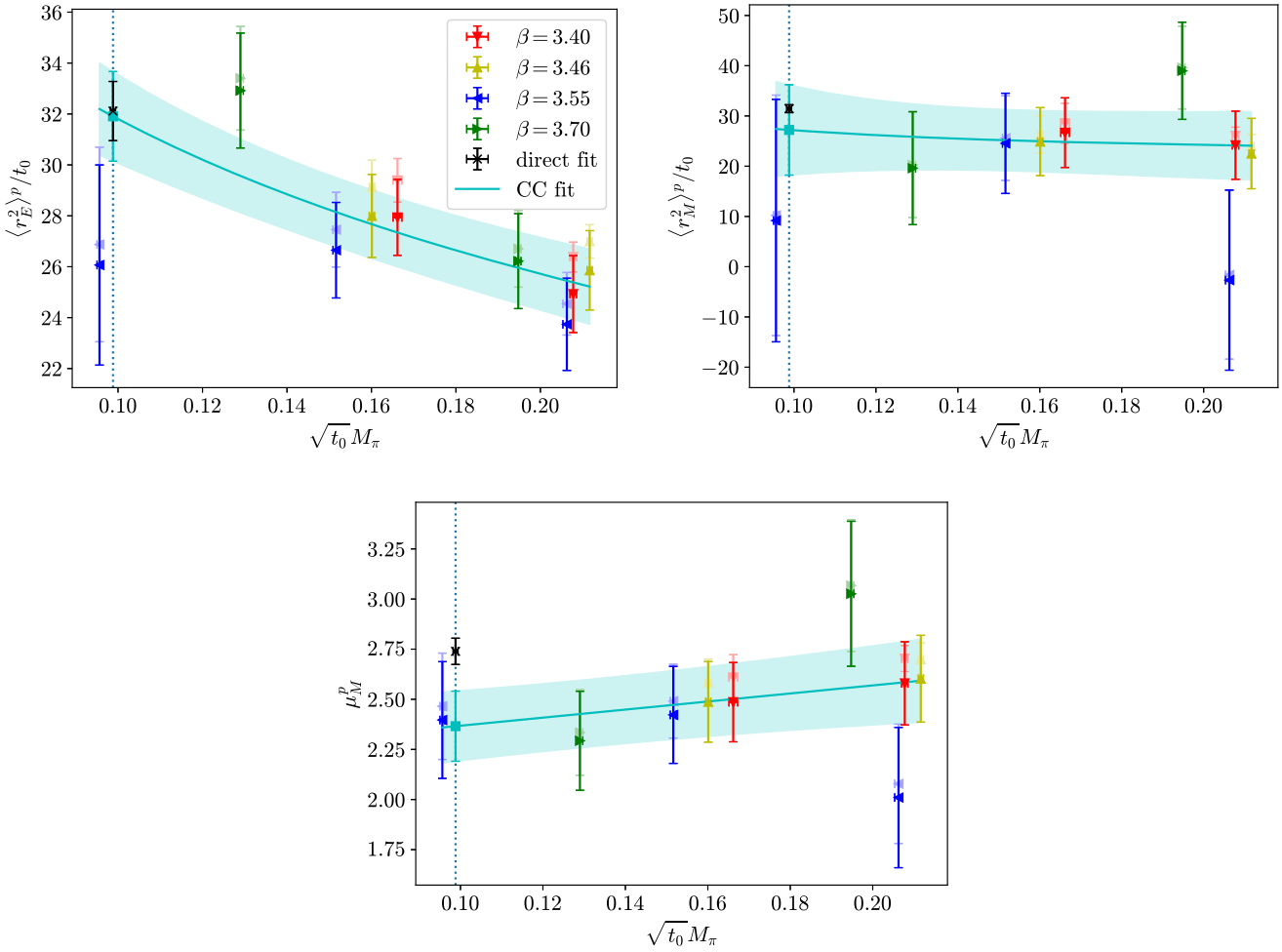

FIG. 5. Electromagnetic radii and magnetic moment of the proton as a function of the pion mass. The faint symbols represent our original lattice data obtained from a z expansion with $Q^2_{\text{cut}} = 0.6$ GeV^2, while the opaque ones have been corrected for the continuum limit. The cyan lines and bands depict an extrapolation fit (CC fit) according to Eqs. (29)–(31). Its results at the physical point are shown as cyan squares and the model-averaged results of the direct fits as black crosses [*cf.* Eqs. (42)–(44)], with a dotted vertical line at the physical pion mass (in units of $\sqrt{t_0}$) to guide the eye.

function not being unduly stiff and avoiding overfitting especially on ensembles with a bad resolution in Q^2.

The errors on the nucleon and pion masses as well as those from the scale setting are included in the analysis using the same parametric bootstrap procedure as for the direct fits. In order to account for the correlation between G_E and G_M, the two form factors are fitted simultaneously even though they do not share any common fit parameters. However, the different channels (proton, neutron, isovector, and isoscalar) are treated separately, in order to mirror the analysis with the direct fits as closely as possible.

We find that the z expansion describes the data generally very well. In particular for G_M, however, the form factor is in some cases very flat around $Q^2 = 0$. This seems to be partly due to fluctuations in the data, against which the z expansion is not sufficiently stable. Consequently, it can be assumed that the magnetic moments and radii determined from these fits are considerably too small.

Using the z expansion, we obtain a set of results for the electromagnetic radii and the magnetic moment on each ensemble. They are listed in Appendix F for two different cuts in the momentum transfer ($Q^2 \leq 0.6$ GeV^2 and $Q^2 \leq 0.7$ GeV^2). We note that the lowest cut in Q^2 which is applicable for all ensembles required for a chiral and continuum extrapolation is in fact roughly 0.6 GeV^2. The ensembles dedicated to the study of finite-volume effects (H105 and S201) do not even have enough data points to permit a z expansion with these momentum cuts. As the finite-volume dependence is not sufficiently constrained by the z-expansion data on the remaining ensembles, we neglect it for the purpose of this crosscheck.

For the chiral and continuum extrapolation of the above datasets, we employ fit formulas inspired by heavy-baryon chiral perturbation theory (HBχPT) [31]. We only take the leading-order dependence on the pion mass into account, since any higher-order coefficients are very poorly

constrained by our data, and add terms $\propto a^2$ in order to account for discretization effects. This leads us to the following *Ansätze* for the isovector, proton, and neutron channels,

$$\frac{\langle r_E^2\rangle}{t_0} = A + D\ln(\sqrt{t_0}M_\pi) + E\frac{a^2}{t_0}, \tag{29}$$

$$\frac{\langle r_M^2\rangle}{t_0} = A + \frac{D}{\sqrt{t_0}M_\pi} + E\frac{a^2}{t_0}, \tag{30}$$

$$\mu_M = A + B\sqrt{t_0}M_\pi + E\frac{a^2}{t_0}. \tag{31}$$

The terms in the one-loop HBχPT expressions for the electromagnetic radii and the magnetic moment with the pion-mass dependence shown in Eqs. (29)–(31) do not contribute in the isoscalar channel [31,90,101]. In the absence of any concrete higher-order HBχPT results, we employ the following *Ansatz* for all three isoscalar observables,

$$A + Ct_0M_\pi^2 + E\frac{a^2}{t_0}. \tag{32}$$

The extrapolated results at the physical point are collected in Appendix G for two different cuts each in the pion mass ($M_\pi \leq 0.27$ GeV and $M_\pi \leq 0.3$ GeV) and the momentum transfer ($Q^2 \leq 0.6$ GeV^2 and $Q^2 \leq 0.7$ GeV^2). The numbers for $\langle r_E^2\rangle$ are, with the slight exception of the neutron, stable within their errors and compare well to the results of the direct fits [*cf.* Eqs. (36), (39), (42), and (45) below]. The magnetic radii exhibit somewhat more variation while having a considerably larger error compared with the direct fits. This is mostly due to the latter fitting G_E and G_M together with common fit parameters, thus leveraging the knowledge that both form factors are governed by the same underlying physics. For the magnetic moments, the agreement with the direct fits tends to be worse than for the radii: they are (except in the isoscalar channel) significantly smaller in magnitude than those obtained from the direct fits [*cf.* Eqs. (38), (41), (44), and (47)], which are in turn well compatible with the experimentally very precisely known values (*cf.* Fig. 8).

For illustration, we display in Fig. 5 the extrapolation for the proton using $M_{\pi,\mathrm{cut}} = 0.3$ GeV and $Q^2_{\mathrm{cut}} = 0.6$ GeV^2. We note that individual ensembles can deviate rather strongly from the fit curve, which is most apparent for the magnetic observables on J303 and N200. This is probably due to the low momentum resolution on these two ensembles, which implies a long extrapolation to $Q^2 = 0$, where the radius and the magnetic moment are defined, but no lattice data is available. We also note that the relative weights in the extrapolation fit do not reflect the number of Q^2 points entering the z expansion, which is different on each ensemble. In this sense the two-step process, first performing z-expansion fits and subsequently extrapolating, masks the relative paucity of data points at small momentum transfer for some ensembles.

We conclude that the direct fits are superior to the analysis using a z-expansion followed by a chiral and continuum extrapolation, in particular for the description of the magnetic form factor: they are more stable against fluctuations on individual momenta or ensembles and take more information about the physical properties of the form factors into account, which helps in reducing the errors. In cases where the two-step procedure based on the z-expansion is stable and trustworthy, both methods give consistent results. Therefore, we do not find any evidence that the functional forms employed by the direct BχPT fits introduce a systematic bias. We also remark that there is no meaningful possibility of averaging the results from the direct BχPT fits with those from the z expansion because the latter are, in particular for the magnetic quantities, much less precise and simply not competitive.

V. MODEL AVERAGE AND FINAL RESULTS

For the reasons stated above, we favor the analysis based on the direct fits and hence restrict our presentation of the final results to this method. Within this approach, we have no strong *a priori* preference for one specific setup, and thus determine our final results and total errors from averages over different fit models and kinematic cuts. For this purpose, we employ weights derived from the AIC [102,103].

The applicability of the AIC in its original form is called into question in the presence of Bayesian priors for some fit parameters or when only subsets of data are fitted as a result of applying kinematical cuts. Therefore, we apply the Bayesian Akaike information criterion (BAIC) proposed in Ref. [104]. It reads

$$\mathrm{BAIC}_i = \chi^2_{\mathrm{noaug,min},i} + 2n_{f,i} + 2n_{c,i}, \tag{33}$$

where $\chi^2_{\mathrm{noaug,min},i}$ denotes the minimum of the χ^2 function for the ith model excluding the contribution of the priors. $n_{f,i}$ is the corresponding number of fit parameters and $n_{c,i}$ the number of cut data points. This criterion takes the goodness of fit into account, while at the same time penalizing a reduction of the degrees of freedom that may result either from the introduction of further fit parameters or from cutting away data points. For the proton and neutron observables, which are derived from two separate fits to the isovector and isoscalar form factors, the BAIC is obtained as the sum of the BAIC values of both fits (which would be the BAIC resulting from a combined fit with the cross-correlations between the two channels set to zero[6]).

[6]Estimating these correlations is not feasible because the size of the resulting covariance matrices would be much larger than the number of available configurations on some ensembles.

For the weighting of the different models, one can use [104–106]

$$w_i^{\mathrm{BAIC}} = \frac{e^{-\mathrm{BAIC}_i/2}}{\sum_j e^{-\mathrm{BAIC}_j/2}}. \tag{34}$$

When computing these weights for our set of models, it turns out that the BAIC strongly prefers the fits with the least stringent cut in Q^2. This is due to the relatively large number of data points which is cut away by lowering Q^2_{cut} in a fit across several ensembles. The effect is enhanced by our two most chiral ensembles E250 and E300, which feature a comparatively large density of Q^2 points. Since the radii and the magnetic moment are defined in terms of the low-Q^2 behavior of the form factors, a stricter cut in Q^2 is theoretically better motivated for an extraction of these quantities. Hence, we employ Eq. (34) for each value of Q^2_{cut} at a time to weight the remaining variations, i.e., the pion-mass cut and the modelling of lattice artifacts. Using these separately normalized BAICs, we finally apply a flat weight function to the estimates originating from the different Q^2_{cut}. This prescription, which we dub $\overline{\mathrm{BAIC}}$, ensures that the stricter cuts in Q^2, and thus our low-momentum data, have a strong influence on our final results.

In order to estimate the statistical and systematic uncertainties of our model averages, we adopt the procedure from Ref. [107], which we briefly sketch in the following. To this end, one treats the model-averaged quantity as a random variable with a cumulative distribution function (CDF) adding up from the weighted CDFs of the individual models,

$$P^x(y) = \sum_{i=1}^{N_M} \frac{w_i^{\overline{\mathrm{BAIC}}}}{N_B} \sum_{n=1}^{N_B} \Theta(y - x_{i,n}). \tag{35}$$

Here, the outer sum runs over our $N_M = 4 \times 2 \times 7 = 56$ models with the associated weights $w_i^{\overline{\mathrm{BAIC}}}$ computed as explained above. The inner sum runs over the $N_B = 10000$ bootstrap samples obtained from our resampled analysis (*cf.* Sec. IV A). Θ denotes the Heaviside step function and $x_{i,n}$ the estimate for the observable x on the nth sample and using the ith model. Due to the large number of bootstrap samples N_B, the distribution in Eq. (35) is effectively smoothed in spite of being a sum of step functions. The final value and the total error are easily read off from this distribution as the median and the quantiles which would correspond to the central 1σ of an effective Gaussian distribution, respectively. In order to isolate the statistical and systematic errors, one can scale the width of the bootstrap distributions entering Eq. (35) by a factor of λ. Under the assumption that such a rescaling of the errors of the individual model results only affects the statistical, but not the systematic error, one can separate these two contributions as demonstrated in Ref. [107]. We use $\lambda = 2$ as in Ref. [107], but we remark that the results of this method are essentially independent of the choice of λ for our data as long as $\lambda \gtrsim 2$.

The collection of results for the electromagnetic radii and the magnetic moment of the proton together with the CDF obtained as explained above is displayed in Fig. 6. One can see that approximately the expected fraction of results lie within the 68% quantiles of the averaged distribution. Moreover, the symmetrized errors as shown by the gray bands agree well with the (generally nonsymmetric) quantiles of the distributions, which are indicated by the dashed lines. Since this statement holds for all four channels, we quote the symmetrized errors together with our final results,

$$\langle r_E^2 \rangle^{u-d} = (0.785 \pm 0.022(\mathrm{stat}) \pm 0.026(\mathrm{syst}))\ \mathrm{fm}^2, \tag{36}$$

$$\langle r_M^2 \rangle^{u-d} = (0.663 \pm 0.011(\mathrm{stat}) \pm 0.008(\mathrm{syst}))\ \mathrm{fm}^2, \tag{37}$$

$$\mu_M^{u-d} = 4.62 \pm 0.10(\mathrm{stat}) \pm 0.07(\mathrm{syst}), \tag{38}$$

$$\langle r_E^2 \rangle^{u+d-2s} = (0.554 \pm 0.018(\mathrm{stat}) \pm 0.013(\mathrm{syst}))\ \mathrm{fm}^2, \tag{39}$$

$$\langle r_M^2 \rangle^{u+d-2s} = (0.657 \pm 0.030(\mathrm{stat}) \pm 0.031(\mathrm{syst}))\ \mathrm{fm}^2, \tag{40}$$

$$\mu_M^{u+d-2s} = 2.47 \pm 0.11(\mathrm{stat}) \pm 0.10(\mathrm{syst}), \tag{41}$$

$$\langle r_E^2 \rangle^{p} = (0.672 \pm 0.014(\mathrm{stat}) \pm 0.018(\mathrm{syst}))\ \mathrm{fm}^2, \tag{42}$$

$$\langle r_M^2 \rangle^{p} = (0.658 \pm 0.012(\mathrm{stat}) \pm 0.008(\mathrm{syst}))\ \mathrm{fm}^2, \tag{43}$$

$$\mu_M^{p} = 2.739 \pm 0.063(\mathrm{stat}) \pm 0.018(\mathrm{syst}), \tag{44}$$

$$\langle r_E^2 \rangle^{n} = (-0.115 \pm 0.013(\mathrm{stat}) \pm 0.007(\mathrm{syst}))\ \mathrm{fm}^2, \tag{45}$$

$$\langle r_M^2 \rangle^{n} = (0.667 \pm 0.011(\mathrm{stat}) \pm 0.016(\mathrm{syst}))\ \mathrm{fm}^2, \tag{46}$$

$$\mu_M^{n} = -1.893 \pm 0.039(\mathrm{stat}) \pm 0.058(\mathrm{syst}). \tag{47}$$

We find that we can obtain the magnetic radii of the proton and neutron to a very similar precision to their respective electric radii.

We have compared the above numbers to the results of two alternative averaging strategies: the BAIC weights of (34) applied to all variations, i.e., also the cut in Q^2, or a naive (flat) average imposing a p-value cut at 1%. For the latter, we have used the average statistical uncertainty, and

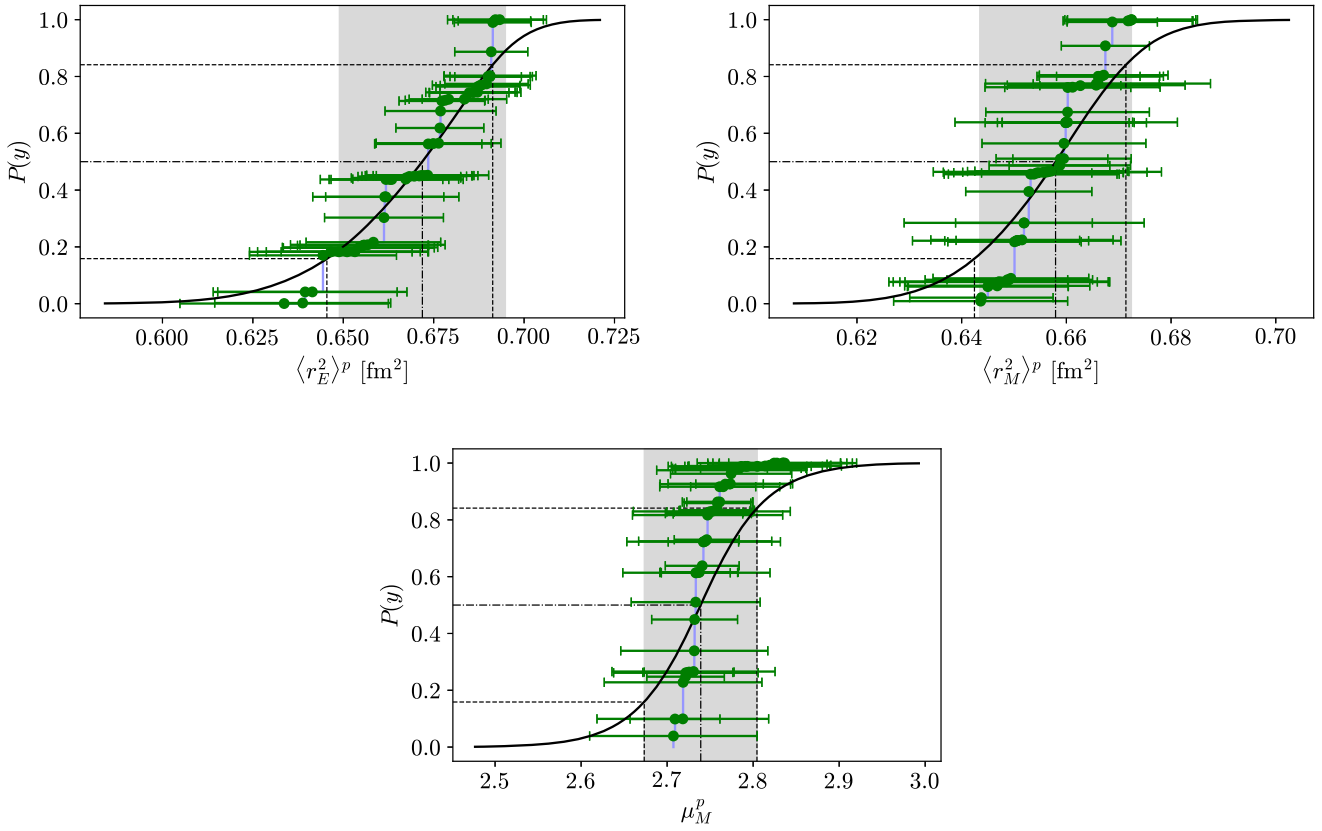

FIG. 6. Cumulative distribution function of the electromagnetic radii and the magnetic moment of the proton for all fitted models. The green points depict the central values and errors of the individual fit results. The thick black line shows the weighted CDF according to Eq. (35). For comparison, we also include a CDF based on the central values only, i.e., $P^x(y) = \sum_{i=1}^{N_M} w_i^{\overline{\mathrm{BAIC}}} \Theta(y - x_i)$, which is displayed by the light blue line. The dashed-dotted and dashed lines indicate the median and the central 68% quantiles, respectively. The gray bands, on the other hand, depict the symmetrized errors quoted in Eqs. (42)–(44).

the variance determined from the spread of the fit results as a systematic error estimate [108]. While this method is robust, it is also very conservative and susceptible to overestimating the true errors. The "plain" BAIC, on the other hand, drastically underestimates the systematic error for observables which display a non-negligible dependence on Q^2_{cut}. For these reasons, we adopt the model averaging procedure $\overline{\mathrm{BAIC}}$ explained above. We note, however, that the results of all three methods are compatible within errors.

In analogy to the radii and the magnetic moments, one can also average the form factors evaluated at the physical point and at particular values of Q^2 over the model variations. The results are plotted in Fig. 7 for the proton and neutron and are directly compared to experimental data. For the proton, one can observe a moderate deviation in the slope of the electric form factor between our result and that of the A1 collaboration [3] over the whole range of Q^2. As shown in the inset, the slope of our electric form factor at low Q^2 is much closer to that of the PRad experiment [13] than to that of Ref. [3]. The magnetic form factor, on the other hand, agrees well with that of Ref. [3]. For the neutron, we compare with the collected experimental world data [109], which are largely compatible with our curves within our quoted errors. Only the slope of our magnetic form factor differs somewhat from experiment. Furthermore, our results reproduce within their errors the experimental values of the magnetic moments both of the proton and of the neutron [91].

Our updated radii and magnetic moment in the isovector channel [*cf.* Eqs. (36)–(38)] agree well with our previously published results [47], with similar errors on the electric radius and the magnetic moment, and an improved error on the magnetic radius.

In Fig. 8, we compare our results for the proton and neutron [*cf.* Eqs. (42)–(47)] to recent lattice determinations and to the experimental values. We remark that the only other complete lattice study including disconnected contributions is Ref. [45], which, however, does not perform a continuum and infinite-volume extrapolation. Our estimates for the electric radii of the proton and neutron are larger in magnitude than the results of Refs. [44–46], while Ref. [38] quotes an even larger central value for $\sqrt{\langle r_E^2 \rangle^p}$. We stress that any difference between our estimate and previous lattice calculations is not related to our preference for direct fits to the form factors, as opposed to the more traditional analysis via the z expansion. In fact, the

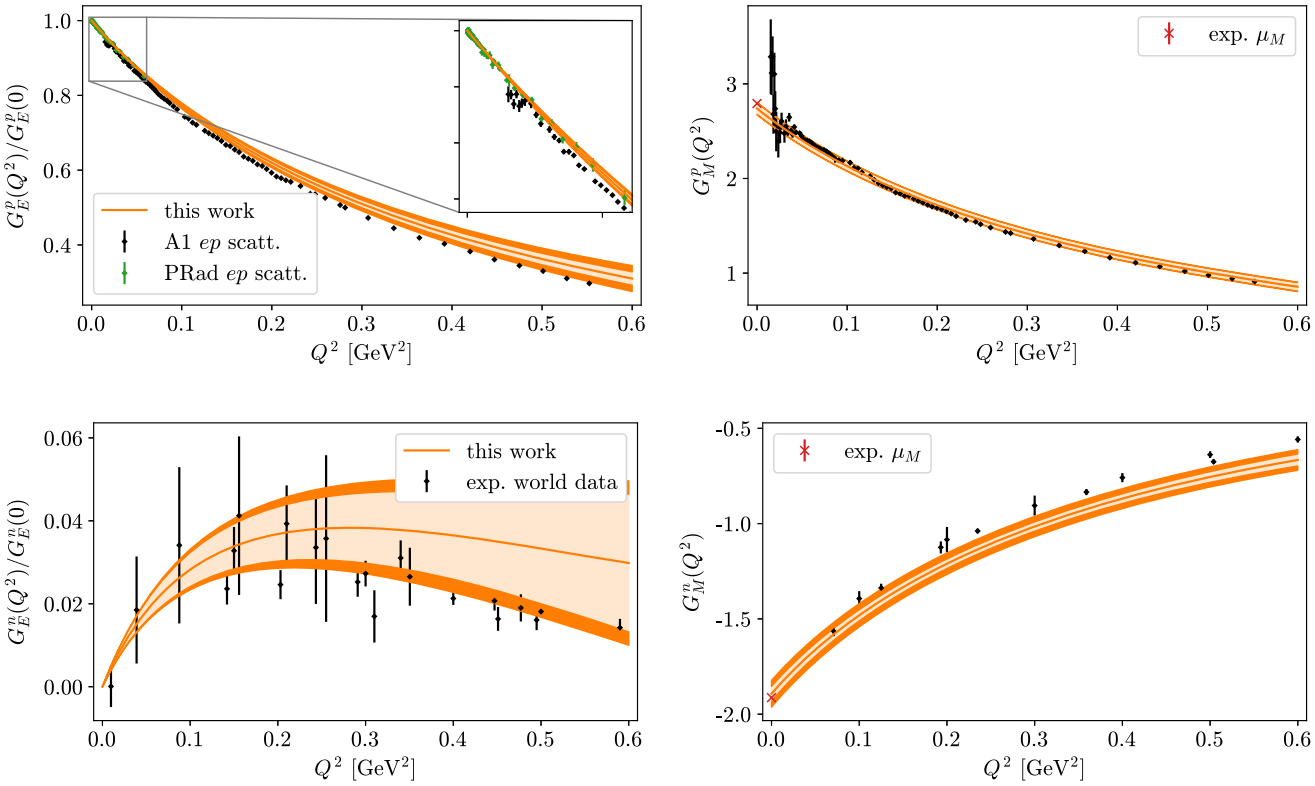

FIG. 7. Electromagnetic form factors of the proton and neutron at the physical point as a function of Q^2. The orange curves and bands correspond to our final results with their full uncertainties obtained as model averages over the different direct fits. The light orange bands indicate the statistical uncertainties only. For the proton, the black diamonds represent the experimental ep-scattering data from A1 [3] obtained using Rosenbluth separation, and the green diamonds the corresponding data from PRad [13]. For the neutron, the black diamonds show the experimental world data collected in Ref. [109]. The experimental values of the magnetic moments [91] are depicted by red crosses.

z-expansion approach yields similar values for our data. Furthermore, we obtain results for the magnetic moments of the proton and neutron, as well as for $\sqrt{\langle r_M^2\rangle^n}$, which are considerably larger in magnitude than that of Refs. [37,45], while being compatible with that of Ref. [44]. This improves the agreement with the experimental values [91]. In the case of the magnetic moments, the latter are very precisely known and are reproduced by our estimates within our quoted uncertainties. For $\sqrt{\langle r_M^2\rangle^n}$, we observe nevertheless a 3.2σ tension between our result and the experimental average by the Particle Data Group (PDG) (after combining all errors in quadrature). On the level of the form factor G_M^n evaluated at any particular value of Q^2, however, the discrepancy is much smaller, as can be seen from Fig. 7 (bottom right). For $\sqrt{\langle r_M^2\rangle^p}$, our result is only about 1.2 combined standard deviations larger than that of Ref. [45]. We note that our results for the isoscalar radii [*cf.* Eqs. (39) and (40)] are larger than those of Ref. [45] by a greater amount, while μ_M^{u+d-2s} compares well between our study and Ref. [45].

For the electric and magnetic radii of the proton, the experimental situation is much less clear than for the magnetic moment. As is the case for most of the other recent lattice calculations [44–46], our result for $\sqrt{\langle r_E^2\rangle^p}$ is much closer to the PDG value [91], which is completely dominated by muonic hydrogen spectroscopy, than to the A1 ep-scattering result [3]: While we only observe a very mild 1.5σ tension with the former, we disagree at the 3.7σ level with the latter (after combining all errors in quadrature). We note that we achieve an even better 0.6σ agreement with the recent ep-scattering experiment by PRad [13], which has also yielded a small electric radius of the proton. For $\sqrt{\langle r_M^2\rangle^p}$, on the other hand, our estimate is well compatible with the value inferred from the A1 experiment by the analyses [3,27] and exhibits a sizable 2.8σ tension with the other collected world data [27]. As can be seen from Fig. 7 (top right), the good agreement with A1 is not only observed in the magnetic radius, but also for the Q^2 dependence of the magnetic form factor over the whole range of Q^2 under study. We note that the dispersive analysis of the Mainz/A1 and PRad data in Ref. [17] has yielded a significantly larger magnetic radius [$\sqrt{\langle r_M^2\rangle^p} = (0.847 \pm 0.004(\text{stat}) \pm 0.004(\text{syst}))$ fm] than the z-expansion-based analysis of the Mainz/A1 data in Ref. [27]. The former value also exhibits a 3.4σ tension with our result, which is partly due to its substantially smaller error compared to Ref. [27]. Possible

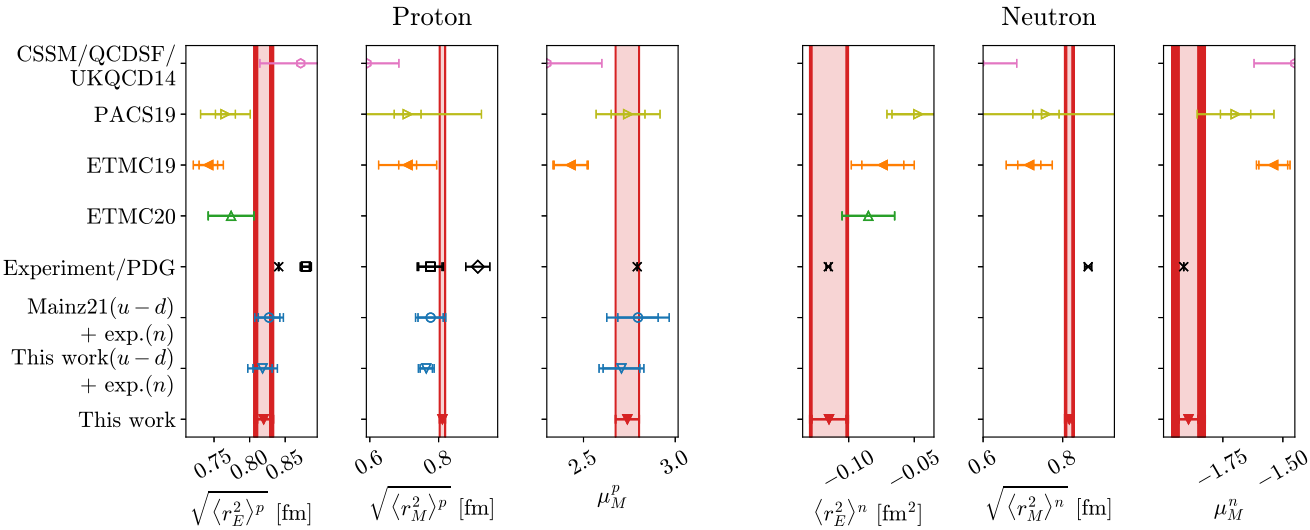

FIG. 8. Comparison of our best estimates (red downward-pointing triangle) for the electromagnetic radii and the magnetic moments of the proton and neutron with other lattice calculations, i.e., Mainz21 [47] (blue circle), ETMC20 [46] (green upward-pointing triangle), ETMC19 [45] (orange leftward-pointing triangle), PACS19 [44] (yellow rightward-pointing triangle), and CSSM/QCDSF/UKQCD14 [37,38] (pink hexagon). Only studies with filled markers, i.e., ETMC19 and this work, include disconnected contributions and hence represent a full lattice calculation. The Mainz21 values for the proton have been computed by combining their isovector results with the PDG values for the neutron [91]. We also show this estimate using our updated isovector results from this work (blue downward-pointing triangle). The experimental values for the neutron and for μ_M^p are taken from PDG [91] (black cross). The two data points for $\sqrt{\langle r_E^2\rangle^p}$ represent the values from PDG [91] (cross) and Mainz/A1 [3] (square), respectively. The two data points for $\sqrt{\langle r_M^2\rangle^p}$, on the other hand, depict the reanalysis of Ref. [27] either using the world data excluding that of Ref. [3] (diamond) or using only that of Ref. [3] (square). For ease of comparison, the red bands show our final results with the full uncertainty, with the light bands indicating the statistical errors.

reasons for this discrepancy include unaccounted-for isospin-breaking effects.

Our statistical and systematic error estimates for the electric radii and magnetic moments are commensurate with the other lattice studies, while being substantially smaller for the magnetic radii. We remark that the missing data point at $Q^2 = 0$ complicates the extraction of the magnetic low-Q^2 observables in most recent lattice determinations, especially for z-expansion fits on individual ensembles. The direct approach has, additionally to combining information from several ensembles and from G_E and G_M, less freedom and by itself allows for considerably less variation in the form factors at low Q^2. We believe this to be responsible, in large part, for the small errors we find in the magnetic radii.

VI. CONCLUSIONS

In this paper, we have investigated the electromagnetic form factors of the proton and neutron in lattice QCD with $2+1$ flavors of dynamical quarks at the physical point including both quark-connected and -disconnected contributions. For the precise and effective computation of the latter, we have made use of a split-even estimator, i.e., the one-end trick [68,71,72]. Systematic effects due to excited states have been accounted for by using the summation method with a conservative choice for the window in the minimal source-sink separation over which the summation fits have been averaged. By matching our lattice results with the predictions from covariant baryon chiral perturbation theory, we have performed simultaneous fits to the Q^2-, pion-mass, lattice-spacing, and finite-volume dependence of the form factors in the isospin basis. From these fits, the electromagnetic radii and magnetic moments of the proton and neutron have been extracted. We thus obtain the first complete lattice results for these quantities which have a full error budget, i.e., all relevant systematic effects are taken into account. Our final estimates can be found in Eqs. (36)–(47).

As an important benchmark, we reproduce the experimentally very precisely known magnetic moments within our quoted uncertainties. Our result for the electric (charge) radius of the proton is much closer to the value extracted from muonic hydrogen spectroscopy [6] and recent ep-scattering experiments [13] than to the A1 ep-scattering result [3]. For the magnetic radius, on the other hand, our estimate is compatible with the analyses [3,27] of the A1 data, while being in tension with the other collected world data [27]. In summary, we contribute additional evidence to suggest that lattice calculations agree with the emerging consensus about the experimental value of the electric proton radius [110–112]. Meanwhile, the results for the magnetic proton radius require further investigation.

For lattice studies of the electromagnetic form factors, the excited-state contamination remains an important source of systematic uncertainty. Using the summation method, the

signal gets lost in the exponentially growing noise very quickly after the plateau region is reached. This renders firm statements about the exact location of the plateau impossible. A promising strategy to tackle this issue, besides drastically increasing statistics at large source-sink separations, is to perform a dedicated study of the excitation spectrum. To improve on the systematic error due to the continuum and infinite-volume extrapolation, a larger range of lattice spacings and volumes at or near the physical pion mass is necessary. Because of concerns regarding the algorithmic stability of our simulations, the production of coarse and light ensembles is not feasible in our current setup. We are, however, working on the production of a fine ensemble at the physical pion mass, which would help to further constrain both the chiral interpolation and the continuum extrapolation. Moreover, its large volume implies a high density of Q^2 points, which is crucial for an accurate extraction of the radii. We plan to update our analysis including this new ensemble in a future publication.

ACKNOWLEDGMENTS

This research is partly supported by the Deutsche Forschungsgemeinschaft (DFG, German Research Foundation) through Project HI 2048/1-2 (Project No. 399400745) and through the Cluster of Excellence "Precision Physics, Fundamental Interactions and Structure of Matter" (PRISMA$^+$ EXC 2118/1) funded within the German Excellence Strategy (Project No. 39083149). Calculations for this project were partly performed on the HPC clusters "Clover" and "HIMster2" at the Helmholtz Institute Mainz. Other parts were conducted using the supercomputer "Mogon 2" offered by Johannes Gutenberg University Mainz [113], which is a member of the AHRP (Alliance for High Performance Computing in Rhineland Palatinate, [114]) and the Gauss Alliance e.V. The authors also gratefully acknowledge the John von Neumann Institute for Computing (NIC) and the Gauss Centre for Supercomputing e.V. [115] for funding this project by providing computing time on the GCS Supercomputer JUWELS at Jülich Supercomputing Centre (JSC) through Projects No. CHMZ21, No. CHMZ36, No. NUCSTRUCLFL, and No. GCSNUCL2PT. Our programs use the QDP++ library [116] and deflated SAP + GCR solver from the OpenQCD package [56], while the contractions have been explicitly checked using the Quark Contraction Tool [117]. We thank Simon Kuberski for providing the improved reweighting factors [60] for the gauge ensembles used in our calculation. Moreover, we are grateful to our colleagues in the CLS initiative for sharing the gauge field configurations on which this work is based.

APPENDIX A: PION AND NUCLEON MASSES

In Table II, we tabulate the nucleon masses on the gauge ensembles listed in Table I which we employ in the kinematical prefactors entering the effective form factors and in the definition of Q^2, as well as the corresponding pion masses used for the extrapolation to the physical point and for setting τ_{cut} in the z-expansion fits.

TABLE II. Pion and nucleon masses used in this study (in units of $\sqrt{t_0}$). The quoted errors include the error of $\sqrt{t_0^{\mathrm{sym}}}/a$ [82].

ID	$\sqrt{t_0}M_\pi$	$\sqrt{t_0}M_N$
C101	0.1662(10)	0.7160(35)
N101	0.20777(78)	0.7555(22)
H105	0.2073(19)	0.7704(35)
D450	0.16010(62)	0.7160(40)
N451	0.21167(60)	0.7728(22)
E250	0.09560(59)	0.6882(21)
D200	0.15162(74)	0.7261(23)
N200	0.20626(93)	0.7796(27)
S201	0.2163(13)	0.8323(49)
E300	0.12898(70)	0.7151(23)
J303	0.19476(64)	0.7667(22)

Note that the values differ from the ones used in our earlier studies [47,118]. With significantly increased statistics on many ensembles, we now aim for an analysis which is as self-contained as possible. Hence, the nucleon and pion masses are extracted from the two-point functions of the nucleon and pion at zero momentum, respectively, employing a setup that matches the one of our main analysis as closely as possible.

For the nucleon, we use $\Gamma^p = \frac{1}{2}(1+\gamma_0)$ and the highest available statistics in terms of sources. Since we want to utilize much larger source-sink separations than for the construction of the disconnected part of the three-point function, however, we need to ensure that boundary effects are sufficiently suppressed on oBC ensembles. Hence, we impose a minimal temporal distance of 4 fm that the source of the nucleon propagating towards the boundary has to keep from the latter. Afterwards, we average the two-point functions of the forward- and backward-propagating nucleon. On periodic boundary condition ensembles, such a constraint is obviously not required, and all sources can be used for the forward- as well as the backward-propagating nucleon. On the oBC ensemble S201, all sources are placed on a single timeslice which is less than 4 fm from the lower temporal boundary of the lattice, so that only the forward-propagating nucleon can be used.

The two-point functions of the pion have only been measured on a subset of the sources employed for the nucleon because they are already much more precise.

APPENDIX B: ADDITIONAL CROSSCHECKS ON THE EXCITED-STATE ANALYSIS

In this appendix, we provide additional crosschecks on our excited-state analysis in order to ensure that ground-state dominance is reached by our preferred procedure which is described in Sec. III.

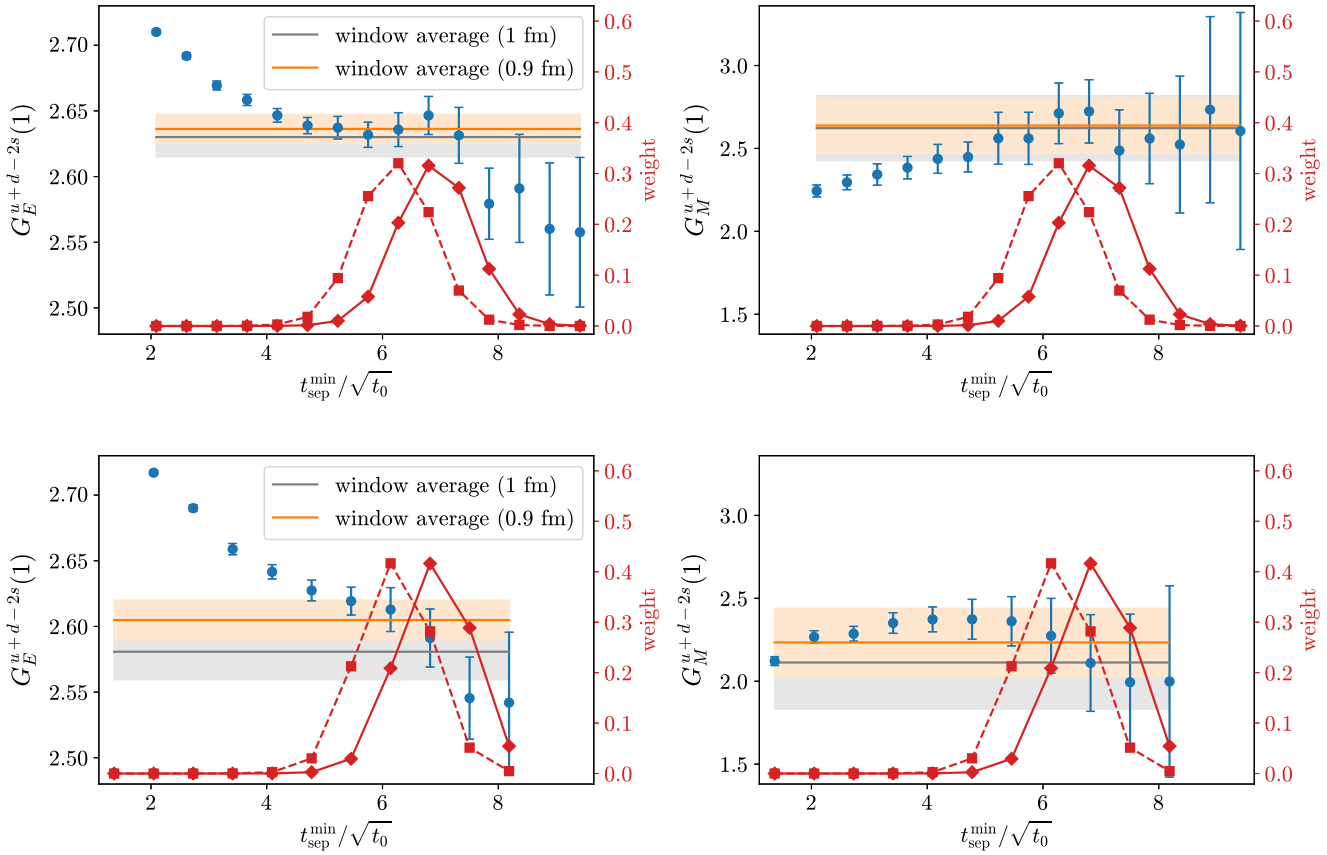

FIG. 9. Extension of Fig. 3 with a different choice of window parameters. Upper panel: D450, lower panel: E300. The gray band corresponds to the result obtained with the weights shown by the diamonds connected by the solid line (centered at 1 fm, our preferred choice). The orange band corresponds to the result obtained with the weights shown by the squares connected by the dashed line (centered at 0.9 fm, as in Refs. [62,63]).

1. Summation method

As mentioned in Sec. III, the choice of the parameters defining the window average in Eq. (18) is not unique. In Fig. 9, we compare two different options corresponding to windows centered at $t_{\rm sep}^{\rm min} \approx 0.9$ and 1 fm, respectively. We observe that both windows lead to compatible (in most cases actually very well compatible) results. Furthermore, the window located at larger $t_{\rm sep}^{\rm min}$, which is the one we have chosen for our main analysis, is not only more conservative regarding the suppression of excited states but also yields a larger error.

Another tunable parameter of the summation method is the number of timeslices $t_{\rm skip}$ omitted at both ends of the operator insertion time [*cf.* Eq. (16)]. Contrary to the naive expectation, a larger value of $t_{\rm skip}$ actually leads to a larger excited-state contamination in the summed ratio at fixed $t_{\rm sep}$. This is due to the factor $\propto \exp[-\Delta(t_{\rm sep}-t_{\rm skip})]$ in the two-state truncated version of the summation method[7] [47],

$$
\begin{aligned}
S_{E,M}(Q^2;t_{\rm sep}) = r_{00}(Q^2)\left[1-\frac{\rho(Q^2)}{2}e^{-\Delta(Q^2)t_{\rm sep}}-\frac{\rho(0)}{2}e^{-\Delta(0)t_{\rm sep}}\right]\frac{1}{a}(t_{\rm sep}+a-2t_{\rm skip}) \\
+\left[r_{01}(Q^2)+r_{00}(Q^2)\frac{\rho(Q^2)}{2}\right]\frac{e^{-\Delta(Q^2)(t_{\rm skip}-a)}-e^{-\Delta(Q^2)(t_{\rm sep}-t_{\rm skip})}}{e^{a\Delta(Q^2)}-1} \\
+\left[r_{10}(Q^2)+r_{00}(Q^2)\frac{\rho(0)}{2}\right]\frac{e^{-\Delta(0)(t_{\rm skip}-a)}-e^{-\Delta(0)(t_{\rm sep}-t_{\rm skip})}}{e^{a\Delta(0)}-1} \\
+r_{11}(Q^2)\frac{e^{-\Delta(Q^2)(t_{\rm skip}-a)-\Delta(0)(t_{\rm sep}-t_{\rm skip})}-e^{-\Delta(Q^2)(t_{\rm sep}-t_{\rm skip})-\Delta(0)(t_{\rm skip}-a)}}{e^{a\Delta(Q^2)}-e^{a\Delta(0)}}+\ldots
\end{aligned}
\tag{B1}
$$

[7]This expression can be obtained by summing Eq. (B2) below over t according to Eq. (16).

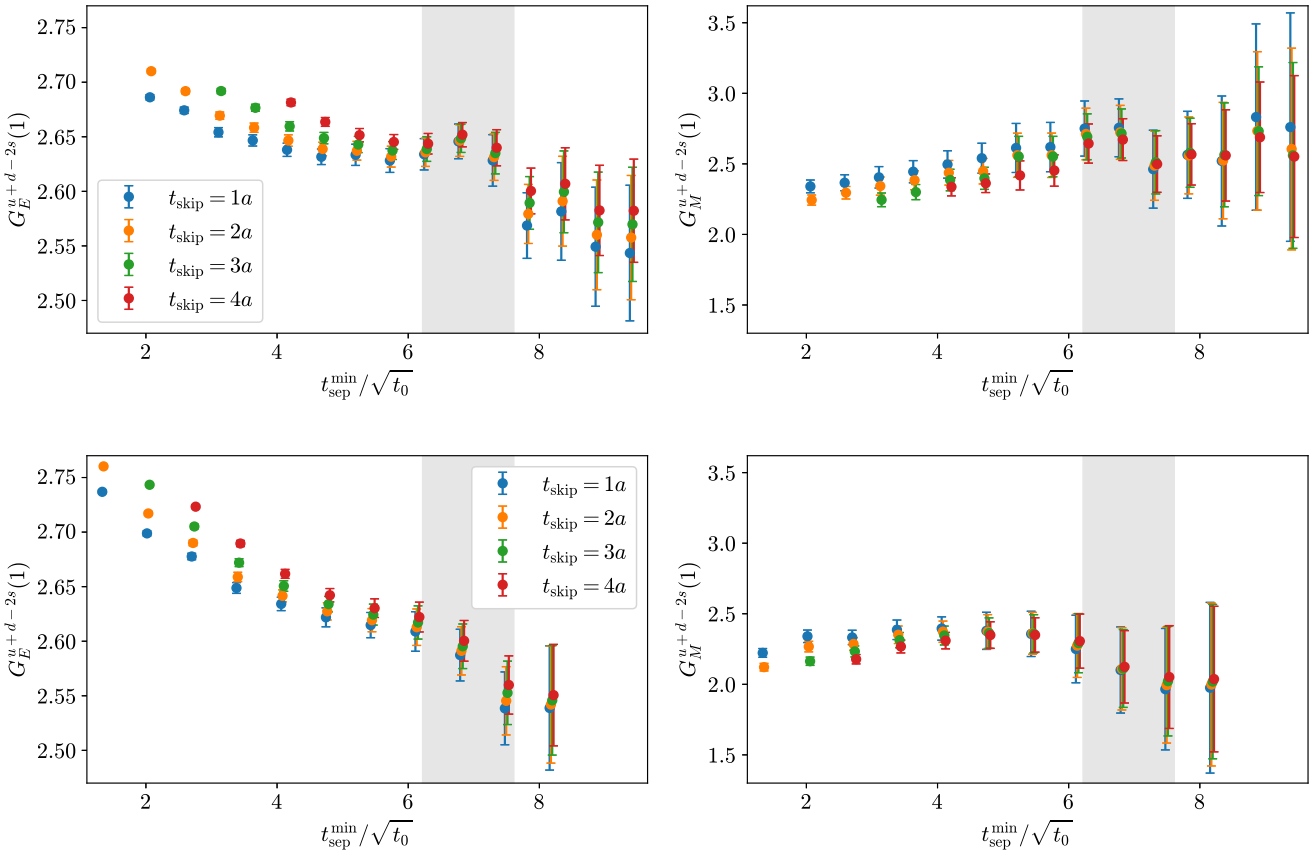

FIG. 10. Extension of 3 (which only shows $t_{\mathrm{skip}} = 2a$) to other values of t_{skip}. Upper panel: D450, lower panel: E300. The vertical gray bands indicate the interval $t_{\mathrm{sep}}^{\mathrm{min}} \in [t_w^{\mathrm{low}}, t_w^{\mathrm{up}}]$ in which the window of (18) has its largest support.

Here, $\Delta(Q^2)$ and $\Delta(0)$ are energy gaps, while the factors $\rho(Q^2)$ and $\rho(0)$ are defined in terms of the overlaps in the two-point functions entering the ratio Eq. (13) [for the exact definition of the latter, see below Eq. (B3)]. $r_{00}(Q^2) = G_{E,M}(Q^2)$ is the ground-state form factor.

If the limit $t_{\mathrm{sep}} \to \infty$ is taken at fixed t_{skip}, all extractions should, independently of t_{skip}, converge to the same ground-state form factor. Both aforementioned trends are actually observed in stability plots for the results of the summation method as a function of $t_{\mathrm{sep}}^{\mathrm{min}}$ and t_{skip}, which can be found in Fig. 10. In the region where the window of (18) has its largest support (indicated in gray in Fig. 10), all (not unreasonably large) values of t_{skip} already agree well. Therefore, using only one value of t_{skip} is perfectly adequate to obtain a reliable estimate of the ground-state form factors and their uncertainties. It can also be seen from Fig. 10 that the errors tend to get smaller with rising t_{skip} because less of the somewhat more noisy data at the borders of the insertion time are employed to build the summed ratios. Consequently, $t_{\mathrm{skip}} = 2a$ appears to be a good compromise between not increasing the excited-state contamination in the summed ratio due to the effect mentioned before and excluding some of the potentially slightly less reliable data close to the source or sink. This is the value we have employed for our main analysis.

2. Two-state fits

Even if the results of the summation method with the window average tuned as explained above appear to yield very conservative error estimates, a comparison with a completely different approach is desirable in order to exclude any systematic bias introduced by relying exclusively on the summation method. Therefore, we perform two-state fits to the effective form factors according to

$$G_{E,M}^{\mathrm{eff}}(Q^2; t_{\mathrm{sep}}, t) = r_{00}(Q^2)\left\{1 + \frac{\rho(Q^2)}{2}\left[e^{-\Delta(Q^2)(t_{\mathrm{sep}}-t)} - e^{-\Delta(Q^2)t_{\mathrm{sep}}}\right] + \frac{\rho(0)}{2}\left[e^{-\Delta(0)t} - e^{-\Delta(0)t_{\mathrm{sep}}}\right]\right\}$$
$$+ r_{01}(Q^2)e^{-\Delta(Q^2)t} + r_{10}(Q^2)e^{-\Delta(0)(t_{\mathrm{sep}}-t)} + r_{11}(Q^2)e^{-\Delta(Q^2)t}e^{-\Delta(0)(t_{\mathrm{sep}}-t)}, \tag{B2}$$

in order to extract the ground-state form factors $r_{00}(Q^2) = G_{E,M}(Q^2)$. We fit the electric and magnetic effective form factors together, with the energy gaps $\Delta(Q^2)$, $\Delta(0)$ and the overlap factors $\rho(Q^2)$, $\rho(0)$ as common fit parameters.

To achieve stable fits, priors on the energy gaps and also on the overlap factors are required. To determine these, we perform two-state fits to the two-point functions,

$$\langle C_2(\mathbf{p}';t_{\mathrm{sep}})\rangle = c_0(\mathbf{p}'^2)e^{-E_0(\mathbf{p}')t_{\mathrm{sep}}} + c_1(\mathbf{p}'^2)e^{-E_1(\mathbf{p}')t_{\mathrm{sep}}}. \quad \text{(B3)}$$

From these fits, we extract the energy gaps $\Delta(Q^2) = \sum_{\tilde{\mathbf{p}}\in\mathfrak{p}}[E_1(\tilde{\mathbf{p}}^2) - E_0(\tilde{\mathbf{p}}^2)]/\sum_{\tilde{\mathbf{p}}\in\mathfrak{p}} 1$ and the overlap factors $\rho(Q^2) = \sum_{\tilde{\mathbf{p}}\in\mathfrak{p}}[c_1(\tilde{\mathbf{p}}^2)/c_0(\tilde{\mathbf{p}}^2)]/\sum_{\tilde{\mathbf{p}}\in\mathfrak{p}} 1$, i.e., we average over equivalent three-momenta. The systematic uncertainty originating from the choice of fit ranges is accounted for by

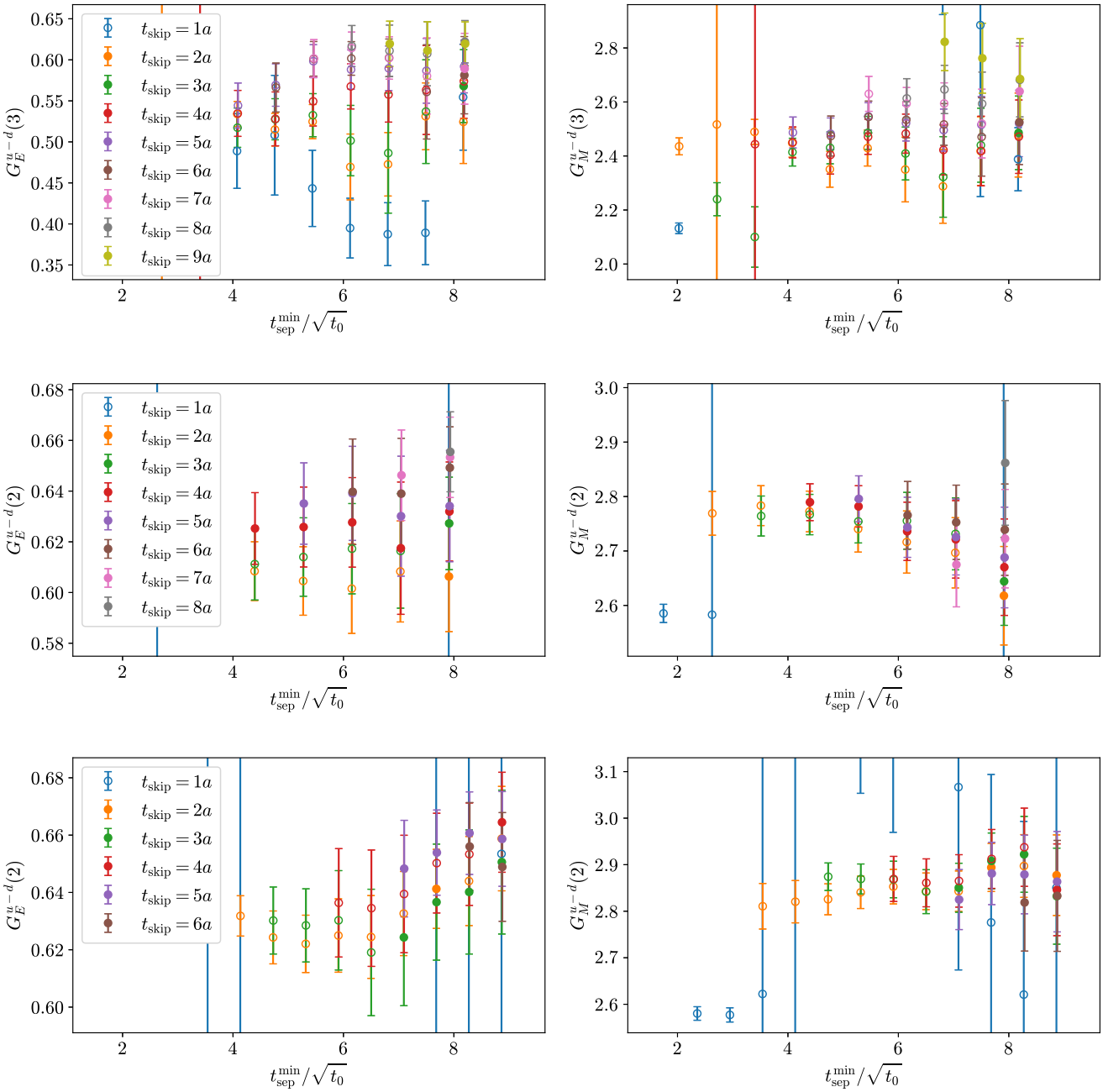

FIG. 11. Isovector electromagnetic form factors at $Q^2 \approx 0.2$ GeV^2 on the ensembles E300 (upper panel), D200 (middle panel), and C101 (lower panel) as a function of the minimal source-sink separation entering the fits to (B2) and for different numbers of timeslices skipped from the borders. Open circles refer to fits with a p value less than 5%. Seemingly missing points lie, due to convergence issues, outside of the plotted range.

averaging over all reasonable options using AIC weights [*cf.* Eqs. (33) and (34)] and adding Gaussian noise to the jackknife distribution according to the systematic covariance matrix [the second term in Eq. (7) in Ref. [119], which is a straightforward generalization of Eq. (7) in Ref. [104]]. Both the two-state fits to the two-point functions and those to the effective form factors are performed using the VarPro method [120] to eliminate the need for initial guesses for the prefactors c_j and r_{jk}, respectively.

As the ρ factors, which are defined by the overlaps in the two-point function, only enter the spectral representation of the ratio used to derive Eq. (B2) via the expansion of the two-point function, we directly take the values obtained from the fits to Eq. (B3) as priors for them. Here, we increase the width of the priors by multiplying the error of ρ by a conservative factor of 3.

The energy gaps, on the other hand, also enter the terms in Eq. (B2) which originate from the expansion of the three-point function. Hence, the situation is less clear than for the ρ factors because the three-point function might have a stronger overlap with different excited states than the two-point function. This is intimately connected with the issue that our calculation, as almost certainly all other current lattice calculations of nucleon matrix elements, is not in the regime where a single excited state dominates the excited-state contamination. Since it is impossible to fit more than one excited state without putting unduly strict priors on the energy gaps (which would correspond to making an *a priori* assumption about what the states are which couple most strongly, and not really letting the data decide on this), the latter must be regarded as effective gaps summarizing the contribution of several excited states. Therefore, we employ relatively loose priors set to the range between $2M_\pi$ and the energy gap obtained from fitting the two-point function. This comes of course at the expense of less stable fits to the effective form factors. But we stress again that it is necessary in order to not introduce a systematic bias by assuming a particular value of the gap.

To determine the range of points which should enter the two-state fits to the effective form factors, we compare different choices of $t_{\mathrm{sep}}^{\mathrm{min}}$ and t_{skip} in Fig. 11. We find that both parameters need to be set to relatively large values in order to obtain stable fit results and p values which are acceptable at least in the majority of cases. Our final choices are $t_{\mathrm{sep}}^{\mathrm{min}} \gtrsim 6.9\sqrt{t_0}$, which corresponds to the peak of the window used in the summation method, and $t_{\mathrm{skip}} \gtrsim 2.6\sqrt{t_0} \approx 0.4$ fm. The latter is realized by $t_{\mathrm{skip}} = 8a$ on E300, $6a$ on D200, and $5a$ on C101. We remark that these

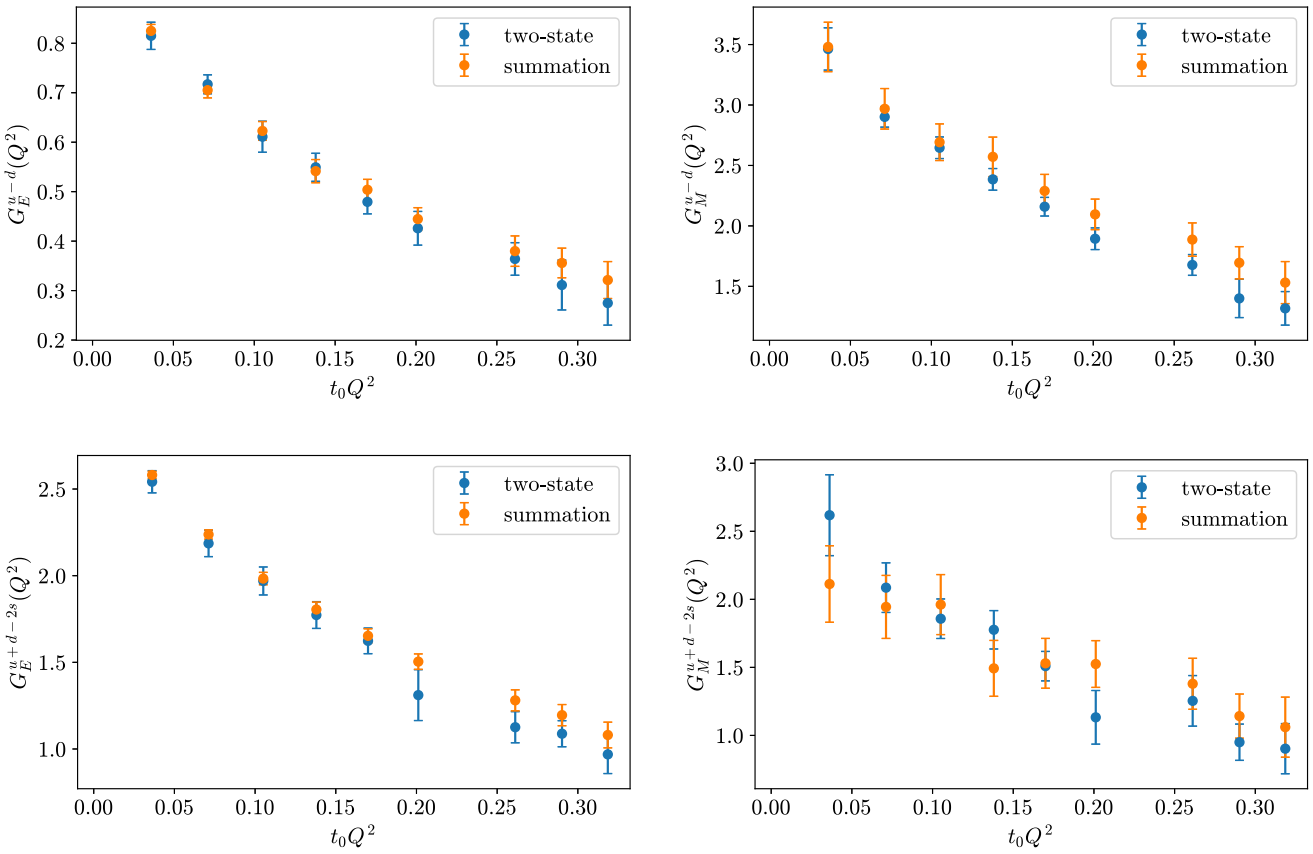

FIG. 12. Isovector and isoscalar electromagnetic form factors on the ensemble E300 as a function of Q^2. The blue points originate from two-state fits to the effective form factors according to Eq. (B2), while the orange ones have been obtained from the summation method using the window average.

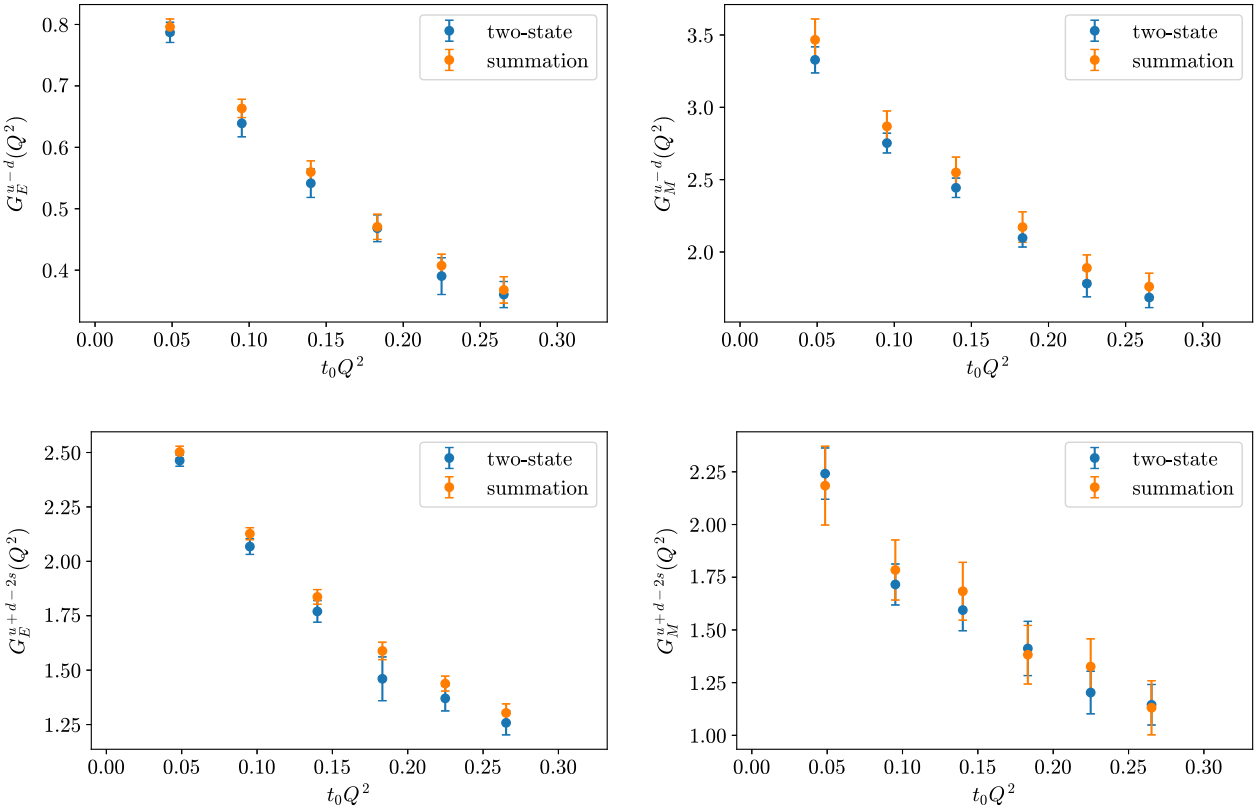

FIG. 13. Same as Fig. 12 for ensemble D200.

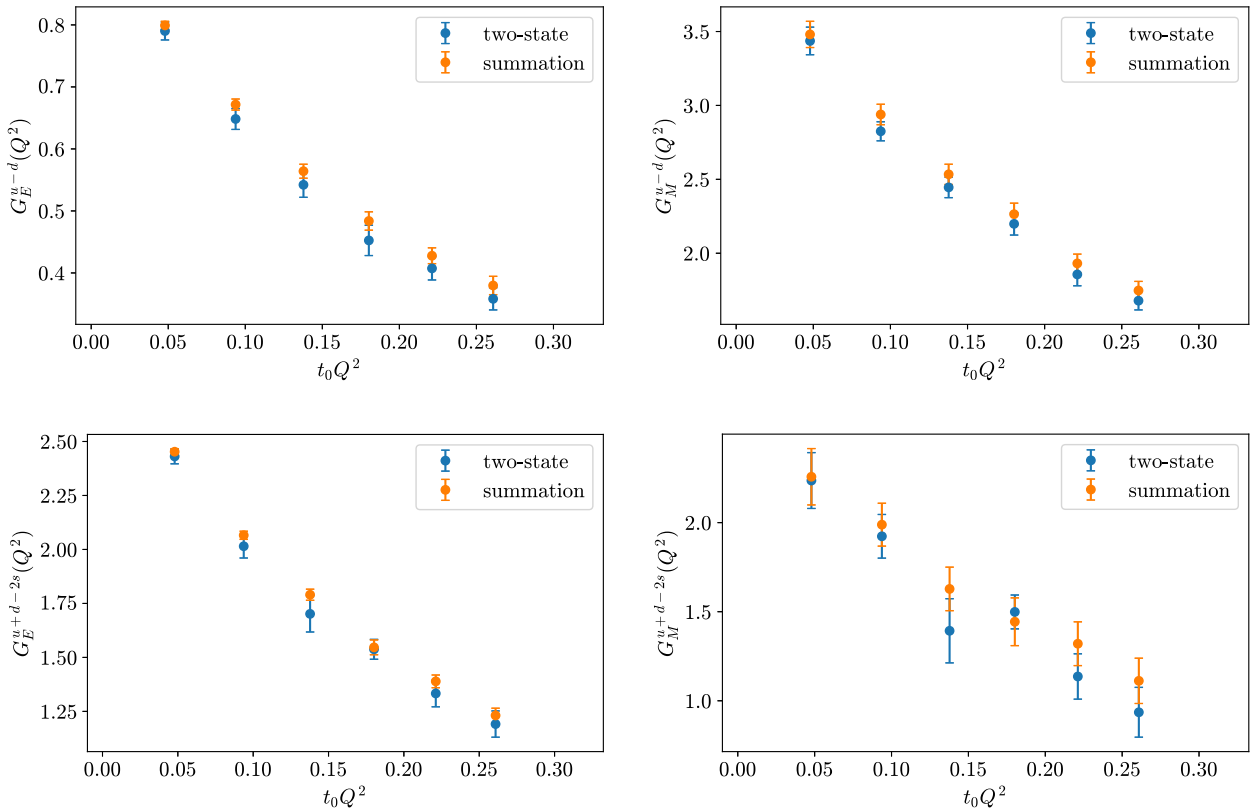

FIG. 14. Same as Fig. 12 for ensemble C101.

values correspond to omitting about half of the data points even at our largest source-sink separation.

In Figs. 12–14, we show plots of the Q^2 dependence of G_E and G_M on the ensembles E300, D200, and C101, comparing the two-state and the summation method. These plots reveal that the two-state fits in general yield smaller errors than the summation method, in particular for the magnetic form factor. We remark that many other lattice studies of nucleon form factors have observed a similar trend in the errors [86]. Besides, the comparison in Figs. 12–14 does not permit the conclusion that either method introduces a directed, systematic bias.

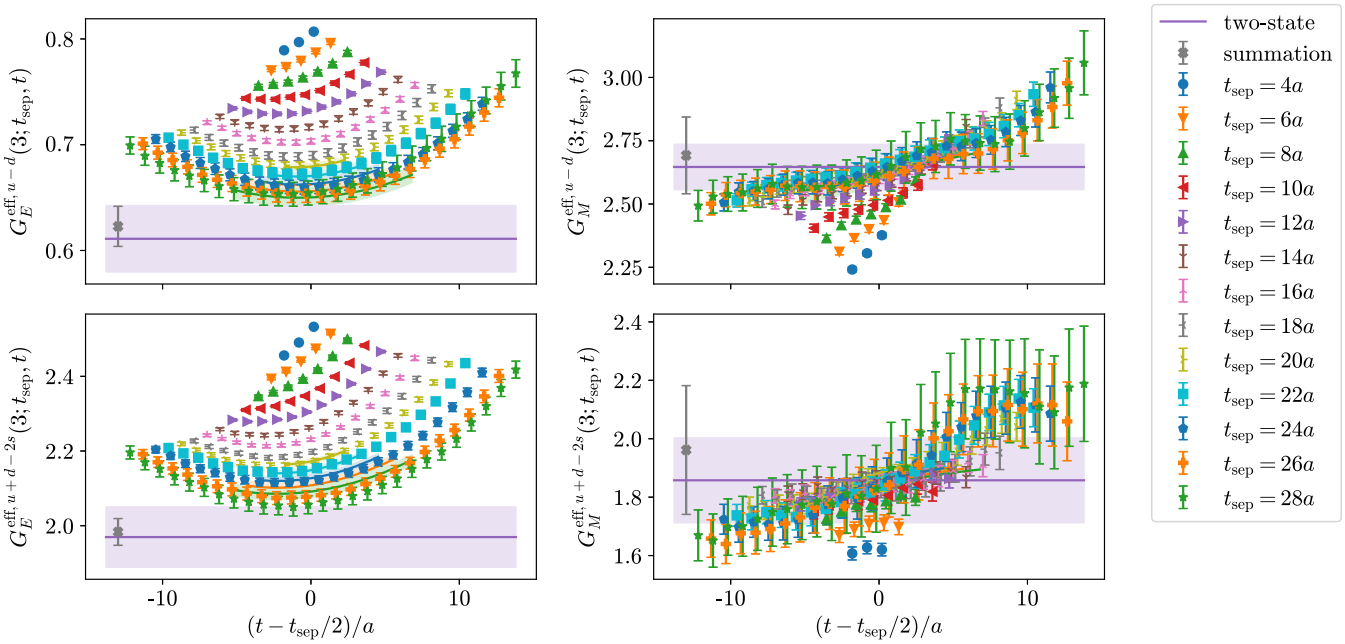

FIG. 15. Isovector and isoscalar effective form factors for ensemble E300 and $Q^2 \approx 0.196$ GeV^2. The data points are horizontally displaced for better visibility. The curves represent the two-state fits in their respective fit intervals, and the horizontal bands their extrapolation to $t_{\mathrm{sep}}, t \to \infty$.

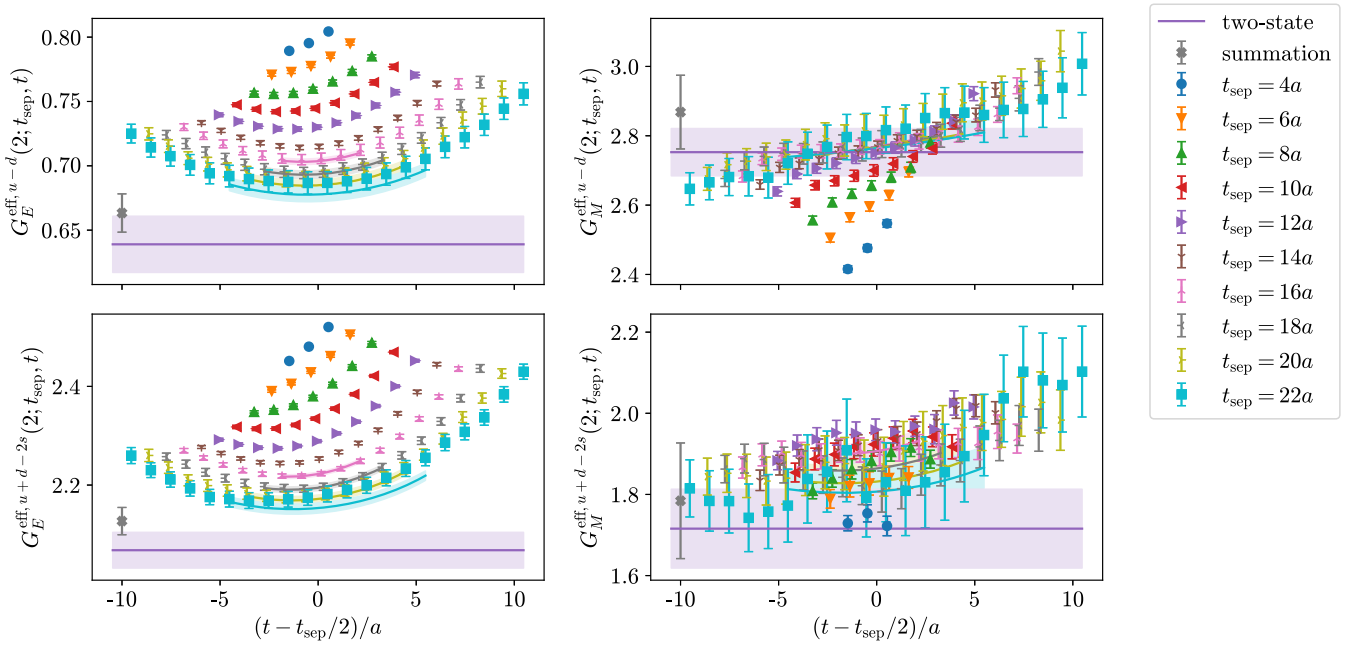

FIG. 16. Same as Fig. 15 for ensemble D200 and $Q^2 \approx 0.177$ GeV^2.

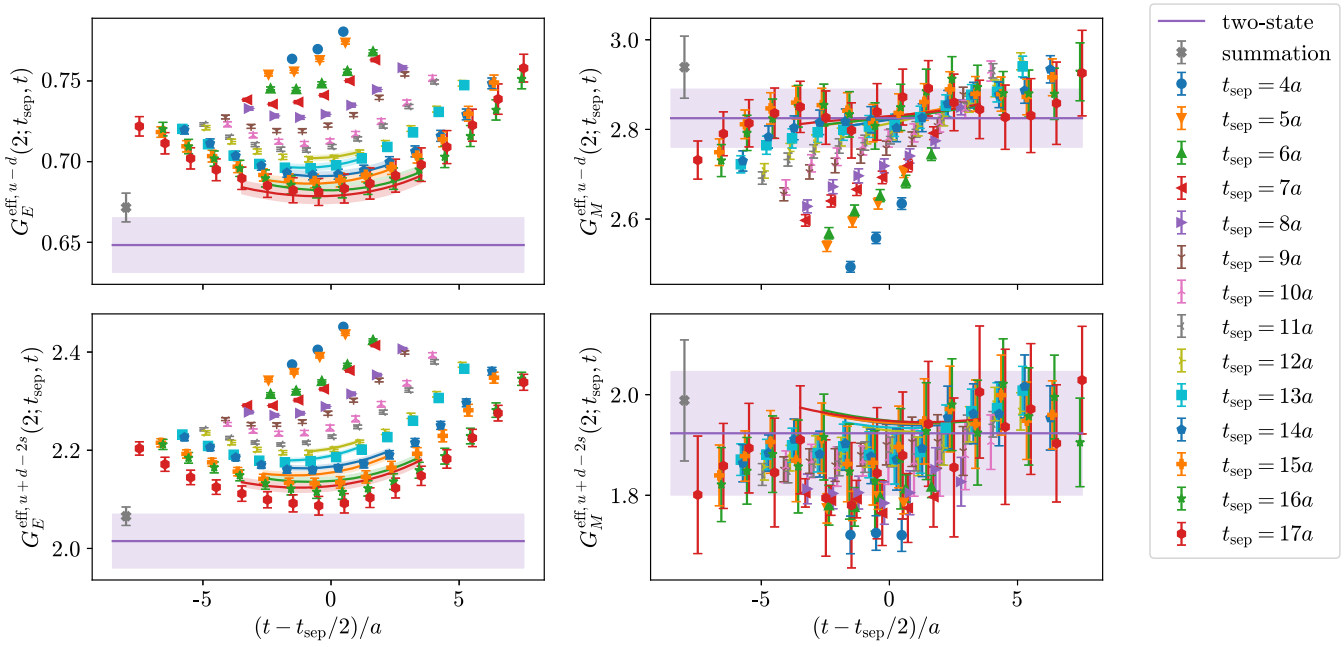

FIG. 17. Same as Fig. 15 for ensemble C101 and $Q^2 \approx 0.174$ GeV^2.

To further quantify the effect on the resulting radii of choosing either the summation method or the two-state fits for the extraction of the ground-state form factors, we have performed BχPT fits on individual ensembles (the ones mentioned above) for both datasets. This may not be the exact same method used to obtain our final results, but it employs the same functional forms and permits a relatively straightforward comparison of the two datasets on the level of individual ensembles. We stress that for the purpose of the subsequent comparison, we have subjected both datasets to exactly the same procedure. While we observe some variations in the results and the correlated difference of the radii extracted either from the summation or the two-state data can be larger than 1σ, there is absolutely no clear pattern to see. On the contrary, the variations appear to be completely random in nature.

Any judgment about the reliability of a method to extract the ground-state form factors should also be based on plots of the effective form factors themselves. These can be found in Figs. 15–17 for the three aforementioned ensembles and $Q^2 \approx 0.2$ GeV^2. They show that the two-state fits in many cases miss the data (even if the p value is decent) and/or lead to an unrealistically large correction compared to the largest source-sink separation we have computed. They also demonstrate that the summation method yields entirely plausible values for the ground-state form factors.

To summarize the discussion, we did not find any indication that the summation method introduces a systematic bias compared to two-state fits. In contrast to the former, the latter require the use of priors. We have observed that the choice of the location as well as of the width of the priors on the energy gaps strongly influences both the central values of the resulting ground-state form factors and their errors. Furthermore, with the relatively broad priors which we have finally adopted, we observe some instabilities in the two-state fits, mostly on ensembles with less statistics than the ones shown here and at higher momenta than those included in the analysis. The opportunity to avoid the use of priors in this very sensitive and crucial step of the analysis is our main reason for preferring the summation method.

APPENDIX C: FORM FACTORS ON E250

As mentioned in the main text describing Fig. 4, the form factors on our near-physical pion mass ensemble E250 seem to exhibit more pronounced statistical fluctuations than on other ensembles. Here, we investigate this point in more detail.

In Fig. 18, the isoscalar effective form factors are shown for the first nonvanishing momentum on E250. It is obvious that the largest two source-sink separations ($t_{\mathrm{sep}} = 20a$ and $22a$) represent an upwards fluctuation. In the electric form factor, this is particularly clear because excited-state effects always have a positive sign here, so that the effective form factor is expected to monotonically decrease with rising t_{sep}. Moreover, doubling the statistics for the disconnected part from the original 398 to now 796 configurations has had (almost) no effect on the largest two source-sink separations as far as the errors are concerned, while reducing the errors of the disconnected contribution substantially for the lower values of t_{sep}. This indicates likewise that fluctuations are still dominant for the largest two source-sink separations.

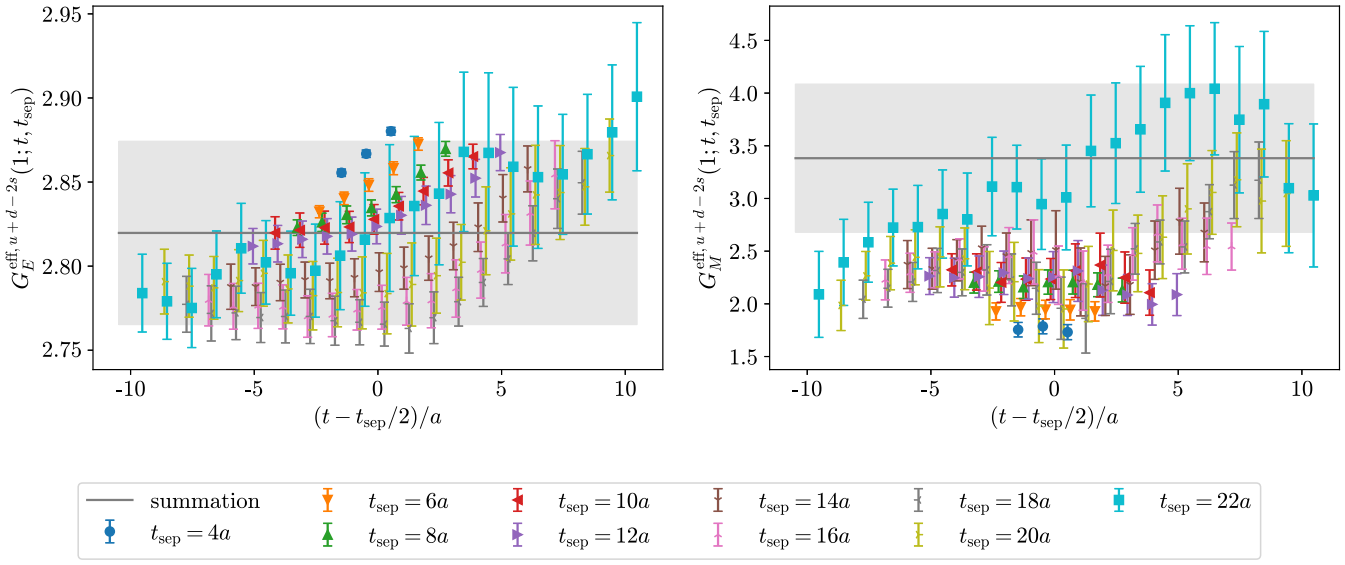

FIG. 18. Isoscalar effective form factors at the first nonvanishing momentum on the ensemble E250 ($Q^2 \approx 0.041$ GeV^2). The meaning of the points and bands is analogous to Fig. 2.

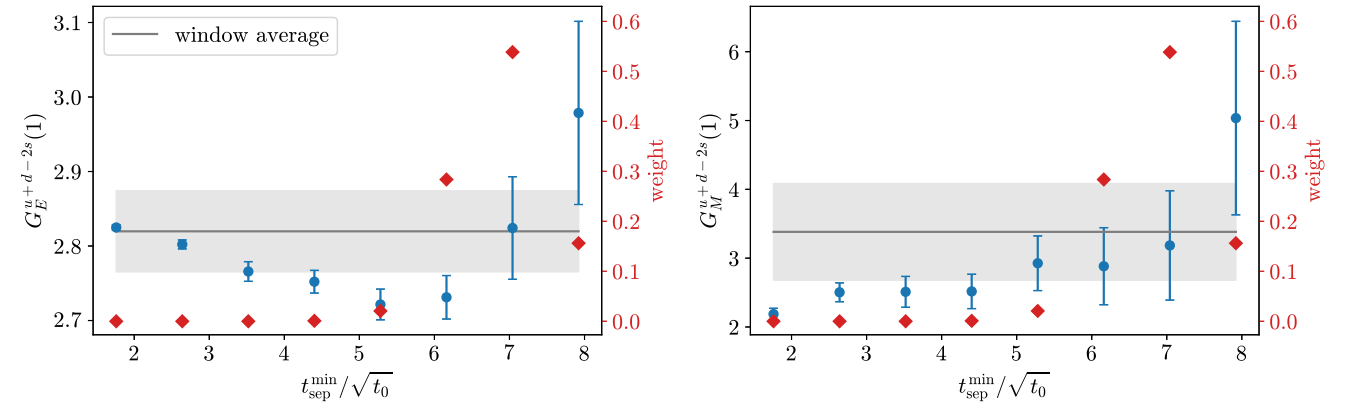

FIG. 19. Isoscalar electromagnetic form factors at the first nonvanishing momentum on the ensemble E250 as a function of the minimal source-sink separation entering the summation fit. The meaning of the points and bands is analogous to Fig. 3.

The upwards fluctuation is also clearly visible in the $t_{\mathrm{sep}}^{\mathrm{min}}$ plots for the form factors extracted from the summation method (*cf.* Fig. 19). Here, mostly the extractions with the largest two values of $t_{\mathrm{sep}}^{\mathrm{min}}$ are affected, as in these cases the influence of the effective form factors at large t_{sep} on the summation fit becomes sizable. Due to our choice for the window, these points have a significant effect on the averaged result as well. This means that on E250, the window average with our values for the parameters $t_w^{\mathrm{up,low}}$ is not able to suppress this statistical fluctuation sufficiently. On the other hand, excited-state effects are also expected to be stronger at lower pion masses. Hence, it does not appear reasonable to adjust the window to lower values of $t_{\mathrm{sep}}^{\mathrm{min}}$ on E250. Besides, the lowest point for G_E^{u+d-2s} in Fig. 19 is still within 2σ of our averaged result, so that these two values are not incompatible with each other, and our error is not grossly underestimated.

As can be seen from Fig. 4, our direct fits are stable against such fluctuations on single ensembles: the fit curves lie below the data at the first ~6 Q^2 points for the isoscalar form factors on E250, i.e., the fit follows much more closely the trend determined by the other ensembles than this obvious fluctuation on E250.

APPENDIX D: FORM FACTOR DATA

In Tables III–XIII, we present the results of extracting the electromagnetic form factors with the summation method using the window average, as described in Sec. III, for every gauge ensemble listed in Table I. The effective form

TABLE III. Electric and magnetic form factors on C101.

Q^2 [GeV^2]	$\hat{G}_E^{u-d}$	G_M^{u-d}	$\hat{G}_E^{u+d-2s}$	G_M^{u+d-2s}	$\hat{G}_E^{p}$	G_M^{p}	G_E^{n}	G_M^{n}
0.089	0.7991(66)	3.480(89)	0.8175(44)	2.26(16)	0.8075(45)	2.116(61)	0.0092(33)	−1.368(40)
0.174	0.6715(89)	2.939(69)	0.6885(63)	1.99(12)	0.6777(60)	1.804(48)	0.0096(47)	−1.137(31)
0.256	0.564(11)	2.534(68)	0.5968(86)	1.63(12)	0.5792(78)	1.538(47)	0.0189(58)	−0.996(32)
0.335	0.484(15)	2.264(75)	0.516(11)	1.44(13)	0.495(11)	1.367(52)	0.0140(79)	−0.886(35)
0.412	0.428(13)	1.931(63)	0.4630(98)	1.32(12)	0.4376(93)	1.180(43)	0.0164(65)	−0.748(31)
0.485	0.380(15)	1.748(62)	0.410(11)	1.11(13)	0.392(11)	1.061(43)	0.0174(73)	−0.692(32)
0.627	0.318(20)	1.513(81)	0.329(17)	1.06(16)	0.324(15)	0.945(56)	0.0050(99)	−0.566(39)
0.695	0.276(21)	1.470(82)	0.301(17)	0.89(15)	0.292(16)	0.887(54)	0.011(10)	−0.584(40)
0.761	0.245(24)	1.35(10)	0.262(21)	0.93(21)	0.254(19)	0.826(70)	0.003(11)	−0.517(54)
0.825	0.234(25)	1.275(98)	0.231(24)	0.70(22)	0.232(21)	0.754(70)	−0.001(12)	−0.523(53)
0.888	0.258(49)	1.07(16)	0.272(41)	0.43(33)	0.272(40)	0.60(11)	0.011(21)	−0.483(82)

TABLE IV. Electric and magnetic form factors on N101.

Q^2 [GeV^2]	$\hat{G}_E^{u-d}$	G_M^{u-d}	$\hat{G}_E^{u+d-2s}$	G_M^{u+d-2s}	$\hat{G}_E^{p}$	G_M^{p}	G_E^{n}	G_M^{n}
0.089	0.8090(52)	3.583(70)	0.8372(29)	2.42(10)	0.8227(36)	2.189(46)	0.0128(24)	−1.405(32)
0.175	0.6753(63)	3.065(55)	0.7129(34)	1.997(82)	0.6940(43)	1.866(36)	0.0174(29)	−1.199(25)
0.258	0.5763(78)	2.657(51)	0.6199(43)	1.711(84)	0.5980(53)	1.612(34)	0.0206(35)	−1.045(24)
0.338	0.4790(92)	2.311(58)	0.5360(60)	1.56(11)	0.5058(66)	1.400(42)	0.0263(41)	−0.908(28)
0.415	0.4277(91)	2.074(52)	0.4802(59)	1.349(77)	0.4538(65)	1.265(32)	0.0259(40)	−0.806(25)
0.491	0.381(12)	1.882(52)	0.4385(65)	1.153(75)	0.4102(81)	1.136(32)	0.0264(53)	−0.739(25)
0.635	0.296(14)	1.534(62)	0.358(10)	1.039(95)	0.327(11)	0.936(42)	0.0321(58)	−0.593(27)
0.704	0.272(16)	1.456(59)	0.3345(99)	0.982(91)	0.303(11)	0.885(41)	0.0290(67)	−0.574(25)
0.772	0.249(17)	1.383(77)	0.295(13)	1.14(12)	0.269(13)	0.879(50)	0.0252(73)	−0.504(37)
0.838	0.238(19)	1.281(76)	0.279(16)	0.90(10)	0.257(14)	0.789(49)	0.0262(87)	−0.495(33)
0.903	0.239(32)	1.30(11)	0.265(21)	1.05(14)	0.257(24)	0.828(71)	0.021(13)	−0.470(45)

TABLE V. Electric and magnetic form factors on H105.

Q^2 [GeV^2]	$\hat{G}_E^{u-d}$	G_M^{u-d}	$\hat{G}_E^{u+d-2s}$	G_M^{u+d-2s}	$\hat{G}_E^{p}$	G_M^{p}	G_E^{n}	G_M^{n}
0.196	0.632(29)	2.71(20)	0.660(17)	1.58(25)	0.646(20)	1.59(12)	0.013(12)	−1.112(88)
0.378	0.428(29)	2.31(17)	0.482(18)	1.32(16)	0.452(21)	1.298(95)	0.022(12)	−0.923(78)
0.548	0.304(39)	1.75(16)	0.369(24)	1.39(22)	0.330(27)	1.12(10)	0.033(16)	−0.649(71)
0.708	0.147(51)	1.30(25)	0.274(38)	0.95(32)	0.214(38)	0.75(15)	0.058(23)	−0.53(11)
0.859	0.165(41)	1.08(16)	0.246(30)	0.72(19)	0.208(33)	0.650(97)	0.035(16)	−0.436(74)
1.003	0.126(41)	0.64(14)	0.199(36)	0.65(20)	0.160(35)	0.425(91)	0.035(17)	−0.223(65)
1.402	0.028(68)	0.03(29)	−0.012(66)	0.20(33)	0.002(56)	0.04(18)	−0.033(35)	−0.00(13)
1.526	0.06(13)	−0.91(42)	−0.04(10)	−0.40(68)	−0.004(96)	−0.60(28)	−0.054(53)	0.28(20)
1.645	−0.061(97)	−0.42(36)	−0.06(11)	0.14(60)	−0.067(88)	−0.22(25)	−0.017(55)	0.28(17)

TABLE VI. Electric and magnetic form factors on D450.

Q^2 [GeV^2]	$\hat{G}_E^{u-d}$	G_M^{u-d}	$\hat{G}_E^{u+d-2s}$	G_M^{u+d-2s}	$\hat{G}_E^{p}$	G_M^{p}	G_E^{n}	G_M^{n}
0.065	0.8520(75)	3.73(13)	0.8767(50)	2.62(20)	0.8657(52)	2.305(85)	0.0083(37)	−1.411(58)
0.127	0.727(10)	3.26(11)	0.7668(64)	2.15(17)	0.7489(71)	1.973(72)	0.0164(47)	−1.269(50)
0.188	0.631(13)	2.92(11)	0.6768(85)	1.85(16)	0.6561(90)	1.738(71)	0.0192(60)	−1.153(51)
0.247	0.566(14)	2.69(10)	0.628(11)	1.92(17)	0.597(10)	1.667(67)	0.0268(72)	−1.016(49)
0.304	0.506(15)	2.403(90)	0.557(10)	1.52(15)	0.534(11)	1.444(59)	0.0247(66)	−0.972(44)
0.360	0.458(17)	2.211(93)	0.506(11)	1.39(15)	0.487(12)	1.316(63)	0.0260(74)	−0.880(43)
0.468	0.392(21)	1.746(92)	0.445(15)	1.13(18)	0.420(16)	1.020(64)	0.025(10)	−0.715(46)

(Table continued)

TABLE VI. *(Continued)*

Q^2 [GeV^2]	$\hat{G}_E^{u-d}$	G_M^{u-d}	$\hat{G}_E^{u+d-2s}$	G_M^{u+d-2s}	$\hat{G}_E^{p}$	G_M^{p}	G_E^{n}	G_M^{n}
0.520	0.363(21)	1.706(92)	0.392(15)	1.16(15)	0.381(15)	1.019(62)	0.0150(95)	−0.676(43)
0.571	0.305(24)	1.71(11)	0.349(18)	1.13(19)	0.329(18)	1.041(74)	0.024(11)	−0.641(49)
0.621	0.284(23)	1.60(10)	0.345(19)	1.11(18)	0.314(18)	0.990(70)	0.027(11)	−0.604(46)
0.670	0.315(36)	1.41(14)	0.341(30)	0.66(24)	0.333(28)	0.801(94)	0.017(19)	−0.613(64)
0.718	0.262(31)	1.20(11)	0.296(24)	0.83(18)	0.279(24)	0.714(72)	0.016(14)	−0.512(58)
0.765	0.249(29)	1.14(12)	0.276(22)	0.71(17)	0.266(23)	0.673(76)	0.014(13)	−0.474(54)
0.858	0.125(72)	1.12(25)	0.303(60)	1.47(40)	0.221(53)	0.78(17)	0.065(33)	−0.37(12)
0.902	0.178(42)	1.14(18)	0.249(33)	0.82(31)	0.206(32)	0.70(12)	0.028(19)	−0.436(77)
0.947	0.143(43)	1.09(18)	0.284(40)	0.41(34)	0.210(35)	0.62(12)	0.043(21)	−0.516(91)
0.990	0.129(49)	0.59(20)	0.226(46)	0.37(32)	0.171(41)	0.33(13)	0.033(26)	−0.320(95)
1.033	0.128(61)	0.75(21)	0.194(51)	0.72(40)	0.160(49)	0.47(14)	0.019(27)	−0.35(12)
1.075	0.118(58)	0.87(24)	0.263(54)	0.61(35)	0.199(48)	0.53(16)	0.048(27)	−0.36(11)
1.117	−0.013(88)	0.64(39)	0.178(96)	0.39(56)	0.065(78)	0.34(26)	0.026(43)	−0.32(17)
1.199	−0.004(91)	0.47(38)	0.210(95)	0.32(58)	0.117(80)	0.20(26)	0.035(48)	−0.35(18)
1.239	0.08(10)	0.52(36)	0.158(98)	−0.08(65)	0.129(88)	0.15(25)	−0.037(47)	−0.45(18)

TABLE VII. Electric and magnetic form factors on N451.

Q^2 [GeV^2]	$\hat{G}_E^{u-d}$	G_M^{u-d}	$\hat{G}_E^{u+d-2s}$	G_M^{u+d-2s}	$\hat{G}_E^{p}$	G_M^{p}	G_E^{n}	G_M^{n}
0.114	0.7753(62)	3.509(66)	0.7930(40)	2.461(90)	0.7843(46)	2.169(41)	0.0089(26)	−1.336(30)
0.222	0.6211(78)	2.939(55)	0.6520(45)	2.034(76)	0.6362(53)	1.813(35)	0.0157(35)	−1.126(25)
0.326	0.5147(94)	2.508(54)	0.5555(60)	1.649(80)	0.5344(64)	1.530(34)	0.0189(46)	−0.973(25)
0.426	0.447(13)	2.220(60)	0.4911(82)	1.540(92)	0.4683(92)	1.365(39)	0.0219(54)	−0.861(29)
0.522	0.389(12)	1.971(55)	0.4346(84)	1.419(79)	0.4102(85)	1.223(36)	0.0210(59)	−0.752(24)
0.615	0.340(14)	1.779(60)	0.393(11)	1.210(89)	0.366(10)	1.094(39)	0.0246(69)	−0.685(27)
0.792	0.284(23)	1.537(91)	0.330(17)	1.02(11)	0.305(18)	0.942(56)	0.0209(97)	−0.593(42)
0.877	0.229(22)	1.307(85)	0.302(19)	0.89(11)	0.265(18)	0.800(53)	0.036(10)	−0.504(38)
0.960	0.214(32)	1.27(14)	0.281(24)	1.16(21)	0.246(26)	0.822(92)	0.030(12)	−0.453(67)
1.040	0.195(33)	1.16(14)	0.276(27)	1.00(21)	0.235(26)	0.735(86)	0.039(14)	−0.427(64)
1.119	0.147(57)	0.95(21)	0.246(52)	0.35(28)	0.198(50)	0.54(14)	0.047(22)	−0.404(92)

TABLE VIII. Electric and magnetic form factors on E250.

Q^2 [GeV^2]	$\hat{G}_E^{u-d}$	G_M^{u-d}	$\hat{G}_E^{u+d-2s}$	G_M^{u+d-2s}	$\hat{G}_E^{p}$	G_M^{p}	G_E^{n}	G_M^{n}
0.041	0.894(16)	3.96(28)	0.939(18)	3.38(70)	0.919(14)	2.51(21)	0.022(11)	−1.41(16)
0.081	0.818(20)	3.67(23)	0.869(19)	2.58(56)	0.844(16)	2.36(15)	0.030(11)	−1.35(14)
0.119	0.742(27)	3.24(18)	0.807(25)	1.87(47)	0.771(23)	1.94(13)	0.029(13)	−1.31(11)
0.158	0.666(30)	3.30(21)	0.742(29)	2.17(58)	0.694(23)	2.02(15)	0.027(19)	−1.27(15)
0.195	0.612(27)	3.04(16)	0.665(23)	2.36(35)	0.633(20)	1.91(11)	0.016(16)	−1.125(91)
0.232	0.559(31)	2.58(14)	0.639(25)	1.76(33)	0.592(23)	1.582(99)	0.029(18)	−1.015(76)
0.303	0.505(33)	2.30(15)	0.498(34)	1.46(34)	0.497(27)	1.36(11)	−0.005(21)	−0.925(75)
0.338	0.464(33)	2.07(13)	0.498(30)	0.50(31)	0.475(27)	1.095(97)	0.010(19)	−0.951(68)
0.372	0.432(38)	1.89(19)	0.443(40)	0.92(38)	0.444(32)	1.09(12)	−0.001(26)	−0.78(10)
0.406	0.407(35)	1.74(17)	0.433(30)	0.83(31)	0.428(28)	1.00(12)	0.001(22)	−0.747(84)
0.439	0.400(53)	1.54(18)	0.443(53)	0.42(50)	0.428(43)	0.81(14)	0.022(32)	−0.74(11)
0.472	0.393(36)	1.68(17)	0.362(53)	0.39(34)	0.376(36)	0.90(11)	−0.016(29)	−0.733(89)
0.504	0.360(39)	1.57(14)	0.379(45)	0.58(29)	0.368(34)	0.844(98)	0.010(26)	−0.699(73)
0.567	0.333(73)	1.22(30)	0.469(88)	0.17(72)	0.402(66)	0.65(21)	0.048(50)	−0.60(14)
0.598	0.319(47)	1.17(21)	0.373(45)	0.35(37)	0.347(41)	0.65(13)	0.015(25)	−0.48(12)
0.629	0.273(44)	1.23(21)	0.288(49)	0.93(47)	0.279(40)	0.76(14)	0.006(27)	−0.48(13)
0.659	0.274(54)	1.25(20)	0.325(66)	0.17(45)	0.296(50)	0.62(13)	0.038(34)	−0.59(12)

(Table continued)

TABLE VIII. *(Continued)*

Q^2 [GeV^2]	$\hat{G}_E^{u-d}$	G_M^{u-d}	$\hat{G}_E^{u+d-2s}$	G_M^{u+d-2s}	$\hat{G}_E^{p}$	G_M^{p}	G_E^{n}	G_M^{n}
0.689	0.273(53)	1.17(25)	0.323(67)	0.13(66)	0.300(49)	0.56(18)	0.018(37)	−0.52(14)
0.718	0.208(50)	1.07(22)	0.291(58)	0.45(47)	0.247(44)	0.57(15)	0.056(33)	−0.46(12)
0.747	0.189(72)	0.59(25)	0.30(10)	0.57(66)	0.238(68)	0.39(18)	0.057(53)	−0.21(16)
0.805	0.106(66)	0.64(24)	0.256(76)	−0.18(76)	0.163(57)	0.22(20)	0.094(47)	−0.35(16)
0.833	0.202(84)	0.78(29)	0.242(91)	−0.77(82)	0.243(69)	0.26(23)	0.035(51)	−0.52(17)
0.860	0.210(70)	0.68(32)	0.307(86)	0.15(71)	0.261(67)	0.34(23)	0.050(42)	−0.28(17)
0.888	0.075(75)	0.30(37)	0.371(90)	0.44(91)	0.237(69)	0.32(26)	0.118(50)	−0.14(23)
0.942	0.015(75)	0.38(28)	0.16(10)	−0.16(88)	0.088(72)	0.11(23)	0.063(52)	−0.26(18)
0.969	0.050(89)	1.10(47)	0.20(12)	0.2(1.2)	0.113(82)	0.52(36)	0.056(60)	−0.39(25)
1.022	0.12(16)	0.34(51)	0.17(18)	−0.3(1.6)	0.11(14)	0.16(43)	0.040(95)	−0.29(33)
1.048	0.04(11)	0.26(33)	0.06(16)	0.1(1.1)	0.06(11)	0.15(29)	0.040(79)	−0.19(22)
1.073	−0.07(12)	0.16(37)	0.14(15)	−0.7(1.1)	0.03(11)	−0.05(30)	0.078(91)	−0.19(23)
1.099	−0.04(13)	0.41(45)	−0.07(20)	−0.2(1.2)	−0.07(13)	0.07(38)	−0.05(10)	−0.49(27)
1.124	−0.14(13)	0.20(47)	−0.01(20)	0.9(1.2)	−0.10(13)	0.32(36)	0.06(10)	−0.05(29)

TABLE IX. Electric and magnetic form factors on D200.

Q^2 [GeV^2]	$\hat{G}_E^{u-d}$	G_M^{u-d}	$\hat{G}_E^{u+d-2s}$	G_M^{u+d-2s}	$\hat{G}_E^{p}$	G_M^{p}	G_E^{n}	G_M^{n}
0.091	0.801(13)	3.47(14)	0.8390(58)	2.18(19)	0.8201(78)	2.094(91)	0.0192(63)	−1.379(65)
0.177	0.668(14)	2.87(11)	0.7131(80)	1.78(14)	0.6904(96)	1.725(66)	0.0221(68)	−1.147(49)
0.261	0.563(18)	2.55(11)	0.616(10)	1.68(14)	0.590(12)	1.551(64)	0.0257(81)	−1.000(51)
0.341	0.474(20)	2.17(11)	0.533(12)	1.38(14)	0.504(14)	1.316(65)	0.0284(96)	−0.857(49)
0.419	0.410(18)	1.890(90)	0.482(11)	1.33(13)	0.448(12)	1.162(56)	0.0360(87)	−0.725(43)
0.494	0.370(21)	1.761(93)	0.437(14)	1.13(13)	0.406(15)	1.070(59)	0.034(10)	−0.691(41)
0.638	0.293(32)	1.66(12)	0.381(22)	0.93(17)	0.339(25)	0.990(75)	0.043(12)	−0.663(56)
0.707	0.306(33)	1.37(11)	0.353(22)	0.94(14)	0.331(25)	0.846(70)	0.024(13)	−0.532(47)
0.774	0.261(38)	1.50(17)	0.347(30)	1.20(23)	0.305(30)	0.95(11)	0.046(16)	−0.553(71)
0.839	0.286(38)	1.33(17)	0.335(31)	1.12(24)	0.311(30)	0.85(11)	0.025(17)	−0.480(70)
0.904	0.202(68)	0.84(23)	0.243(58)	0.49(35)	0.222(56)	0.51(15)	0.013(30)	−0.33(10)

TABLE X. Electric and magnetic form factors on N200.

Q^2 [GeV^2]	$\hat{G}_E^{u-d}$	G_M^{u-d}	$\hat{G}_E^{u+d-2s}$	G_M^{u+d-2s}	$\hat{G}_E^{p}$	G_M^{p}	G_E^{n}	G_M^{n}
0.159	0.731(14)	3.12(13)	0.7317(77)	2.19(17)	0.7313(97)	1.925(83)	0.0011(69)	−1.189(57)
0.308	0.576(18)	2.69(11)	0.580(10)	1.85(14)	0.578(12)	1.651(69)	0.0025(81)	−1.035(48)
0.449	0.493(25)	2.23(12)	0.493(16)	1.40(15)	0.493(18)	1.345(78)	0.001(11)	−0.880(55)
0.584	0.350(36)	1.67(15)	0.386(22)	1.20(18)	0.369(26)	1.034(96)	0.021(14)	−0.632(65)
0.712	0.303(32)	1.52(14)	0.326(22)	1.18(16)	0.315(24)	0.959(86)	0.014(13)	−0.564(60)
0.834	0.352(42)	1.63(18)	0.331(30)	1.09(19)	0.342(33)	1.00(11)	−0.009(16)	−0.635(75)
1.066	0.279(81)	0.83(30)	0.206(61)	0.62(34)	0.248(66)	0.51(19)	−0.026(28)	−0.33(13)
1.176	0.297(96)	0.98(36)	0.291(81)	0.54(35)	0.293(83)	0.57(22)	−0.010(30)	−0.42(15)
1.283	−0.07(17)	1.24(94)	0.17(17)	1.9(1.1)	−0.00(14)	0.92(62)	0.165(77)	−0.36(36)
1.387	0.10(18)	0.92(84)	0.30(19)	1.68(99)	0.19(17)	0.74(56)	0.071(60)	−0.20(31)

factors of the proton and neutron are put together from the isovector and isoscalar combinations according to

$$G_{E,M}^{\mathrm{eff},p} = \frac{1}{6}\left(G_{E,M}^{\mathrm{eff},u+d-2s} + 3G_{E,M}^{\mathrm{eff},u-d}\right),$$
$$G_{E,M}^{\mathrm{eff},n} = \frac{1}{6}\left(G_{E,M}^{\mathrm{eff},u+d-2s} - 3G_{E,M}^{\mathrm{eff},u-d}\right). \tag{D1}$$

To obtain the corresponding numbers in the tables below, we subsequently apply the summation method and the window average. The electric form factors are normalized by $G_E(0)$, except for the neutron, where $G_E^n(0) = 0$. To clarify the notation, we have marked the table columns to which the normalization has been applied with a hat.

TABLE XI. Electric and magnetic form factors on S201.

Q^2 [GeV^2]	$\hat{G}_E^{u-d}$	G_M^{u-d}	$\hat{G}_E^{u+d-2s}$	G_M^{u+d-2s}	$\hat{G}_E^{p}$	G_M^{p}	G_E^{n}	G_M^{n}
0.347	0.482(45)	2.31(27)	0.554(26)	1.31(30)	0.518(31)	1.39(16)	0.035(20)	−0.91(13)
0.657	0.390(49)	1.40(20)	0.399(33)	1.35(33)	0.400(37)	0.91(14)	0.012(21)	−0.551(86)
0.940	0.47(17)	2.23(57)	0.44(10)	1.81(57)	0.47(13)	1.42(36)	−0.017(53)	−0.80(23)
1.202	0.31(23)	1.70(92)	0.11(16)	2.4(1.1)	0.19(18)	1.23(62)	0.028(76)	−0.47(35)

TABLE XII. Electric and magnetic form factors on E300.

Q^2 [GeV^2]	$\hat{G}_E^{u-d}$	G_M^{u-d}	$\hat{G}_E^{u+d-2s}$	G_M^{u+d-2s}	$\hat{G}_E^{p}$	G_M^{p}	G_E^{n}	G_M^{n}
0.067	0.825(13)	3.48(20)	0.8602(71)	2.11(28)	0.8422(86)	2.09(13)	0.0183(61)	−1.390(85)
0.132	0.705(16)	2.97(17)	0.7459(89)	1.94(23)	0.725(10)	1.80(11)	0.0211(72)	−1.167(70)
0.196	0.623(19)	2.69(15)	0.661(12)	1.96(22)	0.639(13)	1.67(10)	0.0197(89)	−1.023(65)
0.257	0.541(23)	2.57(16)	0.602(14)	1.49(21)	0.571(16)	1.54(10)	0.029(11)	−1.036(70)
0.316	0.504(21)	2.29(14)	0.551(14)	1.53(18)	0.527(15)	1.399(89)	0.0245(97)	−0.891(58)
0.374	0.445(23)	2.10(13)	0.501(15)	1.52(17)	0.472(16)	1.297(82)	0.030(11)	−0.802(54)
0.486	0.380(31)	1.89(14)	0.427(20)	1.38(19)	0.402(23)	1.172(89)	0.021(13)	−0.710(59)
0.540	0.356(30)	1.69(13)	0.398(20)	1.14(16)	0.375(22)	1.037(83)	0.020(13)	−0.659(59)
0.593	0.321(37)	1.53(17)	0.360(25)	1.06(22)	0.341(28)	0.94(11)	0.016(15)	−0.591(75)
0.645	0.267(35)	1.55(16)	0.322(26)	1.06(21)	0.294(27)	0.95(10)	0.027(16)	−0.600(69)
0.695	0.293(53)	1.43(19)	0.327(37)	1.19(26)	0.310(39)	0.92(12)	0.020(24)	−0.512(86)
0.745	0.231(45)	1.36(18)	0.296(34)	1.17(23)	0.264(36)	0.87(11)	0.033(17)	−0.487(77)
0.794	0.223(44)	1.33(17)	0.276(33)	0.96(22)	0.249(34)	0.83(11)	0.026(19)	−0.491(72)
0.889	0.202(91)	1.15(37)	0.340(71)	1.11(41)	0.273(73)	0.76(23)	0.070(36)	−0.38(15)
0.935	0.159(56)	1.11(23)	0.260(45)	0.89(29)	0.208(45)	0.70(15)	0.045(23)	−0.405(97)
0.981	0.129(60)	1.06(25)	0.192(48)	0.61(34)	0.165(49)	0.63(17)	0.030(25)	−0.41(10)
1.026	0.102(69)	1.32(30)	0.176(59)	0.90(34)	0.140(57)	0.81(19)	0.029(30)	−0.50(12)
1.070	0.090(70)	0.52(29)	0.154(60)	1.14(41)	0.121(58)	0.46(20)	0.033(29)	−0.06(12)
1.113	0.055(67)	0.63(26)	0.110(55)	0.67(34)	0.082(54)	0.43(17)	0.023(28)	−0.18(11)
1.156	0.18(11)	1.23(47)	0.21(10)	0.86(51)	0.20(10)	0.76(30)	0.004(44)	−0.46(19)
1.240	0.06(10)	0.96(41)	0.184(92)	0.63(50)	0.121(87)	0.59(27)	0.042(45)	−0.36(16)
1.282	−0.00(10)	0.85(51)	0.15(12)	0.53(55)	0.08(10)	0.52(32)	0.071(49)	−0.33(21)

TABLE XIII. Electric and magnetic form factors on J303.

Q^2 [GeV^2]	$\hat{G}_E^{u-d}$	G_M^{u-d}	$\hat{G}_E^{u+d-2s}$	G_M^{u+d-2s}	$\hat{G}_E^{p}$	G_M^{p}	G_E^{n}	G_M^{n}
0.149	0.726(15)	3.27(14)	0.7569(80)	2.17(18)	0.741(10)	1.999(87)	0.0149(70)	−1.279(58)
0.289	0.554(18)	2.53(11)	0.596(10)	1.68(13)	0.575(12)	1.547(67)	0.0204(80)	−0.987(46)
0.422	0.469(25)	2.29(12)	0.494(14)	1.44(15)	0.481(17)	1.389(73)	0.011(11)	−0.904(51)
0.548	0.418(36)	2.12(16)	0.452(24)	1.36(19)	0.435(27)	1.289(98)	0.016(14)	−0.829(67)
0.669	0.377(30)	1.73(13)	0.372(20)	1.15(16)	0.376(23)	1.059(81)	−0.002(12)	−0.674(54)
0.784	0.334(38)	1.52(15)	0.315(26)	1.12(18)	0.329(29)	0.952(92)	−0.003(16)	−0.574(63)
1.003	0.320(70)	1.15(26)	0.145(46)	1.06(31)	0.242(53)	0.76(17)	−0.050(28)	−0.39(11)
1.107	0.295(78)	1.27(31)	0.185(58)	1.31(34)	0.245(63)	0.87(20)	−0.016(28)	−0.41(12)
1.208	0.34(13)	1.02(50)	0.32(11)	1.10(56)	0.33(11)	0.69(32)	−0.010(39)	−0.32(21)
1.306	0.09(11)	0.57(43)	0.028(76)	1.11(50)	0.057(83)	0.47(27)	0.010(41)	−0.11(18)
1.401	0.66(54)	1.5(1.8)	0.27(38)	2.6(2.1)	0.57(48)	1.3(1.3)	−0.08(13)	0.09(52)

APPENDIX E: DIRECT BχPT FITS

In Tables XIV–XVII, we summarize the results for the physical values of the electromagnetic radii and the magnetic moment obtained from the direct BχPT fits as explained in Sec. IV A, applying various cuts in the pion mass ($M_\pi \leq 0.23$ GeV and $M_\pi \leq 0.27$ GeV) and the momentum transfer ($Q^2 \leq 0.3, \ldots, 0.6$ GeV^2). The entries with and without an asterisk in the third column refer to the multiplicative model of Eqs. (23) and (24) and the additive model of Eqs. (21) and (22), respectively. All variations

TABLE XIV. Results for the direct BχPT fits to the isovector electromagnetic form factors.

$M_{\pi,\mathrm{cut}}$ [GeV]	Q^2_{cut} [GeV^2]	Correction	$\langle r_E^2\rangle$ [fm^2]	$\langle r_M^2\rangle$ [fm^2]	μ_M	p value	$\overline{\mathrm{BAIC}}$ weight
0.23	0.3	None	0.793(19)	0.651(13)	4.610(76)	0.188	0.0463
0.23	0.3	a^2	0.758(28)	0.653(18)	4.58(12)	0.214	0.0319
0.23	0.3	$^*a^2$	0.742(36)	0.656(15)	4.51(15)	0.274	0.0663
0.23	0.3	$M_\pi L$	0.791(20)	0.654(15)	4.644(76)	0.165	0.00610
0.23	0.3	$^*M_\pi L$	0.795(21)	0.654(16)	4.640(76)	0.167	0.00798
0.23	0.3	$a^2, M_\pi L$	0.752(30)	0.657(22)	4.61(12)	0.199	0.00400
0.23	0.3	$^*a^2, ^*M_\pi L$	0.737(40)	0.661(19)	4.53(15)	0.252	0.00855
0.23	0.4	None	0.803(16)	0.6558(93)	4.625(70)	0.172	0.0247
0.23	0.4	a^2	0.767(23)	0.659(15)	4.59(11)	0.251	0.0574
0.23	0.4	$^*a^2$	0.747(31)	0.660(12)	4.52(14)	0.305	0.110
0.23	0.4	$M_\pi L$	0.804(17)	0.654(13)	4.661(70)	0.139	0.00373
0.23	0.4	$^*M_\pi L$	0.808(18)	0.655(13)	4.658(70)	0.147	0.00610
0.23	0.4	$a^2, M_\pi L$	0.759(26)	0.660(21)	4.62(12)	0.220	0.00596
0.23	0.4	$^*a^2, ^*M_\pi L$	0.742(36)	0.662(17)	4.54(15)	0.266	0.0119
0.23	0.5	None	0.810(13)	0.6675(73)	4.665(66)	0.115	0.0897
0.23	0.5	a^2	0.793(19)	0.668(14)	4.66(11)	0.114	0.0317
0.23	0.5	$^*a^2$	0.776(27)	0.672(10)	4.58(14)	0.147	0.0844
0.23	0.5	$M_\pi L$	0.808(15)	0.669(12)	4.702(67)	0.0950	0.00938
0.23	0.5	$^*M_\pi L$	0.813(16)	0.671(12)	4.695(66)	0.101	0.0153
0.23	0.5	$a^2, M_\pi L$	0.784(22)	0.672(21)	4.69(11)	0.103	0.00350
0.23	0.5	$^*a^2, ^*M_\pi L$	0.770(32)	0.679(16)	4.59(15)	0.136	0.0110
0.23	0.6	None	0.810(12)	0.6662(70)	4.653(65)	0.171	0.0728
0.23	0.6	a^2	0.791(18)	0.667(14)	4.64(11)	0.182	0.0378
0.23	0.6	$^*a^2$	0.773(26)	0.671(10)	4.56(14)	0.224	0.0970
0.23	0.6	$M_\pi L$	0.810(14)	0.662(11)	4.688(65)	0.141	0.0112
0.23	0.6	$^*M_\pi L$	0.814(16)	0.665(11)	4.686(65)	0.148	0.0160
0.23	0.6	$a^2, M_\pi L$	0.784(21)	0.665(20)	4.68(11)	0.156	0.00391
0.23	0.6	$^*a^2, ^*M_\pi L$	0.769(31)	0.673(16)	4.59(14)	0.196	0.0105
0.27	0.3	None	0.790(18)	0.650(12)	4.666(73)	0.112	0.0499
0.27	0.3	a^2	0.776(25)	0.642(16)	4.72(11)	0.0959	0.00840
0.27	0.3	$^*a^2$	0.766(31)	0.648(13)	4.70(13)	0.106	0.0103
0.27	0.3	$M_\pi L$	0.788(19)	0.653(15)	4.702(73)	0.0854	0.00407
0.27	0.3	$^*M_\pi L$	0.791(20)	0.654(15)	4.697(73)	0.0862	0.00486
0.27	0.3	$a^2, M_\pi L$	0.770(27)	0.645(20)	4.76(11)	0.0751	0.000651
0.27	0.3	$^*a^2, ^*M_\pi L$	0.762(35)	0.652(17)	4.73(14)	0.0818	0.000822
0.27	0.4	None	0.804(15)	0.6548(88)	4.682(67)	0.0956	0.0169
0.27	0.4	a^2	0.785(20)	0.648(13)	4.73(10)	0.0944	0.00447
0.27	0.4	$^*a^2$	0.775(26)	0.653(10)	4.72(13)	0.103	0.00534
0.27	0.4	$M_\pi L$	0.803(16)	0.654(13)	4.721(67)	0.0649	0.00120
0.27	0.4	$^*M_\pi L$	0.807(18)	0.656(13)	4.717(67)	0.0681	0.00172
0.27	0.4	$a^2, M_\pi L$	0.779(23)	0.647(19)	4.77(11)	0.0670	0.000268
0.27	0.4	$^*a^2, ^*M_\pi L$	0.773(32)	0.654(15)	4.75(13)	0.0729	0.000348
0.27	0.5	None	0.812(13)	0.6630(70)	4.716(63)	0.0209	0.00294
0.27	0.5	a^2	0.800(16)	0.650(12)	4.813(97)	0.0219	0.000827
0.27	0.5	$^*a^2$	0.793(22)	0.6586(88)	4.79(12)	0.0209	0.000709
0.27	0.5	$M_\pi L$	0.809(14)	0.668(12)	4.758(63)	0.0143	0.000165
0.27	0.5	$^*M_\pi L$	0.813(16)	0.670(12)	4.747(63)	0.0154	0.000258
0.27	0.5	$a^2, M_\pi L$	0.793(19)	0.653(18)	4.851(99)	0.0156	4.48×10^{-5}
0.27	0.5	$^*a^2, ^*M_\pi L$	0.789(28)	0.665(15)	4.82(13)	0.0154	4.81×10^{-5}
0.27	0.6	None	0.813(12)	0.6588(65)	4.694(61)	0.0184	0.000389
0.27	0.6	a^2	0.797(16)	0.643(13)	4.81(11)	0.0233	0.000210

(Table continued)

TABLE XIV. *(Continued)*

$M_{\pi,\mathrm{cut}}$ [GeV]	Q^2_{cut} [GeV^2]	Correction	$\langle r_E^2\rangle$ [fm^2]	$\langle r_M^2\rangle$ [fm^2]	μ_M	p value	$\overline{\mathrm{BAIC}}$ weight
0.27	0.6	$^*a^2$	0.790(22)	0.6537(92)	4.78(14)	0.0201	0.000128
0.27	0.6	$M_\pi L$	0.812(13)	0.661(11)	4.737(61)	0.0112	1.87×10^{-5}
0.27	0.6	$^*M_\pi L$	0.816(15)	0.663(11)	4.727(62)	0.0122	2.89×10^{-5}
0.27	0.6	$a^2, M_\pi L$	0.791(19)	0.643(19)	4.85(11)	0.0151	9.38×10^{-6}
0.27	0.6	$^*a^2, ^*M_\pi L$	0.788(28)	0.658(15)	4.81(15)	0.0133	6.51×10^{-6}

TABLE XV. Results for the direct BχPT fits to the isoscalar electromagnetic form factors.

$M_{\pi,\mathrm{cut}}$ [GeV]	Q^2_{cut} [GeV^2]	Correction	$\langle r_E^2\rangle$ [fm^2]	$\langle r_M^2\rangle$ [fm^2]	μ_M	p value	$\overline{\mathrm{BAIC}}$ weight
0.23	0.3	None	0.561(19)	0.656(32)	2.42(11)	0.140	0.0397
0.23	0.3	a^2	0.550(20)	0.615(42)	2.58(16)	0.183	0.0133
0.23	0.3	$^*a^2$	0.537(22)	0.592(35)	2.72(18)	0.198	0.0181
0.23	0.3	$M_\pi L$	0.558(19)	0.666(34)	2.42(11)	0.143	0.00680
0.23	0.3	$^*M_\pi L$	0.558(21)	0.656(36)	2.42(11)	0.120	0.00451
0.23	0.3	$a^2, M_\pi L$	0.546(21)	0.625(47)	2.57(16)	0.187	0.00215
0.23	0.3	$^*a^2, ^*M_\pi L$	0.530(25)	0.588(40)	2.73(18)	0.180	0.00211
0.23	0.4	None	0.571(18)	0.675(26)	2.452(94)	0.168	0.0234
0.23	0.4	a^2	0.557(18)	0.623(34)	2.64(15)	0.274	0.0312
0.23	0.4	$^*a^2$	0.542(20)	0.599(30)	2.76(16)	0.284	0.0342
0.23	0.4	$M_\pi L$	0.568(18)	0.689(30)	2.443(94)	0.187	0.00829
0.23	0.4	$^*M_\pi L$	0.568(20)	0.680(31)	2.445(95)	0.150	0.00406
0.23	0.4	$a^2, M_\pi L$	0.552(19)	0.637(42)	2.61(15)	0.290	0.00690
0.23	0.4	$^*a^2, ^*M_\pi L$	0.535(23)	0.598(36)	2.75(17)	0.263	0.00444
0.23	0.5	None	0.572(17)	0.676(25)	2.459(82)	0.398	0.00785
0.23	0.5	a^2	0.562(17)	0.621(33)	2.67(14)	0.527	0.00934
0.23	0.5	$^*a^2$	0.546(19)	0.601(29)	2.75(15)	0.529	0.00861
0.23	0.5	$M_\pi L$	0.567(17)	0.690(28)	2.447(82)	0.440	0.00359
0.23	0.5	$^*M_\pi L$	0.569(19)	0.682(30)	2.446(84)	0.379	0.00173
0.23	0.5	$a^2, M_\pi L$	0.555(18)	0.636(41)	2.63(15)	0.557	0.00243
0.23	0.5	$^*a^2, ^*M_\pi L$	0.539(22)	0.601(36)	2.73(16)	0.508	0.00121
0.23	0.6	None	0.573(17)	0.675(25)	2.441(78)	0.437	0.00700
0.23	0.6	a^2	0.563(17)	0.620(33)	2.65(13)	0.548	0.00700
0.23	0.6	$^*a^2$	0.550(19)	0.605(30)	2.70(14)	0.516	0.00372
0.23	0.6	$M_\pi L$	0.569(17)	0.686(28)	2.427(78)	0.455	0.00207
0.23	0.6	$^*M_\pi L$	0.570(19)	0.679(30)	2.428(80)	0.414	0.00127
0.23	0.6	$a^2, M_\pi L$	0.558(18)	0.632(40)	2.62(14)	0.550	0.00112
0.23	0.6	$^*a^2, ^*M_\pi L$	0.544(22)	0.603(37)	2.69(16)	0.491	0.000443
0.27	0.3	None	0.557(18)	0.672(29)	2.39(11)	0.0952	0.0680
0.27	0.3	a^2	0.541(20)	0.653(39)	2.44(15)	0.129	0.0330
0.27	0.3	$^*a^2$	0.527(22)	0.623(34)	2.55(16)	0.119	0.0368
0.27	0.3	$M_\pi L$	0.555(18)	0.680(31)	2.39(10)	0.0877	0.00918
0.27	0.3	$^*M_\pi L$	0.556(19)	0.669(33)	2.40(11)	0.0786	0.00763
0.27	0.3	$a^2, M_\pi L$	0.537(21)	0.663(45)	2.43(15)	0.125	0.00466
0.27	0.3	$^*a^2, ^*M_\pi L$	0.521(25)	0.615(39)	2.56(16)	0.107	0.00413
0.27	0.4	None	0.566(16)	0.682(25)	2.398(91)	0.119	0.0388
0.27	0.4	a^2	0.551(17)	0.655(34)	2.48(13)	0.181	0.0333
0.27	0.4	$^*a^2$	0.536(20)	0.627(30)	2.57(15)	0.172	0.0374
0.27	0.4	$M_\pi L$	0.564(17)	0.695(28)	2.389(90)	0.124	0.0103
0.27	0.4	$^*M_\pi L$	0.565(18)	0.685(30)	2.394(91)	0.102	0.00595
0.27	0.4	$a^2, M_\pi L$	0.546(19)	0.670(42)	2.45(14)	0.188	0.00721
0.27	0.4	$^*a^2, ^*M_\pi L$	0.529(23)	0.623(37)	2.57(16)	0.155	0.00458

(Table continued)

TABLE XV. *(Continued)*

$M_{\pi,\mathrm{cut}}$ [GeV]	Q^2_{cut} [GeV^2]	Correction	$\langle r_E^2\rangle$ [fm^2]	$\langle r_M^2\rangle$ [fm^2]	μ_M	p value	$\overline{\mathrm{BAIC}}$ weight
0.27	0.5	None	0.569(16)	0.685(24)	2.404(77)	0.355	0.0723
0.27	0.5	a^2	0.558(16)	0.656(33)	2.50(12)	0.430	0.0366
0.27	0.5	$^*a^2$	0.542(19)	0.630(30)	2.56(13)	0.423	0.0492
0.27	0.5	$M_\pi L$	0.565(16)	0.698(27)	2.392(77)	0.378	0.0254
0.27	0.5	$^*M_\pi L$	0.567(18)	0.690(29)	2.395(79)	0.328	0.0133
0.27	0.5	$a^2, M_\pi L$	0.551(17)	0.673(41)	2.47(13)	0.459	0.0114
0.27	0.5	$^*a^2, ^*M_\pi L$	0.535(22)	0.630(37)	2.55(14)	0.402	0.00700
0.27	0.6	None	0.571(16)	0.686(24)	2.394(73)	0.347	0.0705
0.27	0.6	a^2	0.559(16)	0.656(37)	2.49(14)	0.439	0.0580
0.27	0.6	$^*a^2$	0.544(20)	0.634(34)	2.53(15)	0.401	0.0458
0.27	0.6	$M_\pi L$	0.569(16)	0.697(27)	2.382(74)	0.356	0.0228
0.27	0.6	$^*M_\pi L$	0.570(18)	0.690(29)	2.386(76)	0.320	0.0125
0.27	0.6	$a^2, M_\pi L$	0.554(18)	0.670(46)	2.46(15)	0.446	0.0121
0.27	0.6	$^*a^2, ^*M_\pi L$	0.539(23)	0.632(41)	2.52(16)	0.377	0.00572

TABLE XVI. Results for the proton from the direct BχPT fits.

$M_{\pi,\mathrm{cut}}$ [GeV]	Q^2_{cut} [GeV^2]	Correction	$\langle r_E^2\rangle$ [fm^2]	$\langle r_M^2\rangle$ [fm^2]	μ_M	$\overline{\mathrm{BAIC}}$ weight
0.23	0.3	None	0.677(15)	0.652(13)	2.709(52)	0.0597
0.23	0.3	a^2	0.654(21)	0.647(19)	2.722(84)	0.0138
0.23	0.3	$^*a^2$	0.639(25)	0.645(15)	2.707(97)	0.0390
0.23	0.3	$M_\pi L$	0.675(16)	0.656(15)	2.726(52)	0.00135
0.23	0.3	$^*M_\pi L$	0.676(17)	0.655(16)	2.724(52)	0.00117
0.23	0.3	$a^2, M_\pi L$	0.649(22)	0.652(23)	2.734(86)	0.000279
0.23	0.3	$^*a^2, ^*M_\pi L$	0.634(29)	0.649(19)	2.72(10)	0.000586
0.23	0.4	None	0.687(12)	0.6587(96)	2.721(45)	0.0198
0.23	0.4	a^2	0.662(16)	0.653(17)	2.733(75)	0.0611
0.23	0.4	$^*a^2$	0.644(20)	0.650(13)	2.719(92)	0.129
0.23	0.4	$M_\pi L$	0.686(12)	0.659(13)	2.738(45)	0.00106
0.23	0.4	$^*M_\pi L$	0.688(14)	0.659(14)	2.737(45)	0.000845
0.23	0.4	$a^2, M_\pi L$	0.656(18)	0.656(22)	2.744(77)	0.00141
0.23	0.4	$^*a^2, ^*M_\pi L$	0.639(24)	0.652(17)	2.731(95)	0.00180
0.23	0.5	None	0.691(10)	0.6688(86)	2.742(41)	0.0840
0.23	0.5	a^2	0.677(12)	0.660(16)	2.774(70)	0.0354
0.23	0.5	$^*a^2$	0.661(16)	0.660(12)	2.747(87)	0.0867
0.23	0.5	$M_\pi L$	0.688(11)	0.672(12)	2.759(41)	0.00402
0.23	0.5	$^*M_\pi L$	0.691(13)	0.672(13)	2.755(41)	0.00314
0.23	0.5	$a^2, M_\pi L$	0.670(14)	0.666(21)	2.783(73)	0.00101
0.23	0.5	$^*a^2, ^*M_\pi L$	0.655(21)	0.666(17)	2.752(91)	0.00159
0.23	0.6	None	0.691(11)	0.6675(84)	2.733(40)	0.103
0.23	0.6	a^2	0.677(12)	0.660(16)	2.761(70)	0.0536
0.23	0.6	$^*a^2$	0.661(16)	0.660(12)	2.732(85)	0.0731
0.23	0.6	$M_\pi L$	0.690(12)	0.666(12)	2.748(40)	0.00469
0.23	0.6	$^*M_\pi L$	0.692(13)	0.667(12)	2.748(40)	0.00412
0.23	0.6	$a^2, M_\pi L$	0.671(15)	0.660(21)	2.773(72)	0.000887
0.23	0.6	$^*a^2, ^*M_\pi L$	0.657(21)	0.661(17)	2.742(89)	0.000941
0.27	0.3	None	0.673(15)	0.653(12)	2.732(50)	0.110
0.27	0.3	a^2	0.658(19)	0.644(17)	2.768(76)	0.00900
0.27	0.3	$^*a^2$	0.647(22)	0.644(14)	2.775(87)	0.0123
0.27	0.3	$M_\pi L$	0.672(16)	0.657(15)	2.750(50)	0.00122

(Table continued)

TABLE XVI. *(Continued)*

$M_{\pi,\mathrm{cut}}$ [GeV]	Q^2_{cut} [GeV^2]	Correction	$\langle r_E^2\rangle$ [fm^2]	$\langle r_M^2\rangle$ [fm^2]	μ_M	$\overline{\mathrm{BAIC}}$ weight
0.27	0.3	$^*M_\pi L$	0.673(17)	0.657(15)	2.748(50)	0.00121
0.27	0.3	$a^2, M_\pi L$	0.653(20)	0.648(21)	2.784(77)	9.86×10^{-5}
0.27	0.3	$^*a^2, ^*M_\pi L$	0.641(26)	0.647(18)	2.791(90)	0.000110
0.27	0.4	None	0.685(11)	0.6588(91)	2.741(43)	0.0225
0.27	0.4	a^2	0.668(14)	0.649(15)	2.776(67)	0.00509
0.27	0.4	$^*a^2$	0.655(18)	0.649(12)	2.786(81)	0.00682
0.27	0.4	$M_\pi L$	0.684(12)	0.660(12)	2.758(43)	0.000422
0.27	0.4	$^*M_\pi L$	0.686(13)	0.660(13)	2.758(43)	0.000350
0.27	0.4	$a^2, M_\pi L$	0.663(16)	0.651(20)	2.793(69)	6.60×10^{-5}
0.27	0.4	$^*a^2, ^*M_\pi L$	0.651(22)	0.649(16)	2.805(84)	5.45×10^{-5}
0.27	0.5	None	0.6900(92)	0.6661(80)	2.759(39)	0.0253
0.27	0.5	a^2	0.679(11)	0.651(14)	2.823(63)	0.00361
0.27	0.5	$^*a^2$	0.667(15)	0.654(11)	2.824(77)	0.00416
0.27	0.5	$M_\pi L$	0.687(10)	0.672(12)	2.778(39)	0.000499
0.27	0.5	$^*M_\pi L$	0.690(12)	0.672(12)	2.773(39)	0.000410
0.27	0.5	$a^2, M_\pi L$	0.672(14)	0.656(19)	2.837(65)	6.11×10^{-5}
0.27	0.5	$^*a^2, ^*M_\pi L$	0.662(20)	0.660(15)	2.834(81)	4.02×10^{-5}
0.27	0.6	None	0.692(10)	0.6627(77)	2.746(38)	0.00555
0.27	0.6	a^2	0.678(11)	0.645(15)	2.819(71)	0.00246
0.27	0.6	$^*a^2$	0.667(15)	0.651(12)	2.814(89)	0.00119
0.27	0.6	$M_\pi L$	0.691(11)	0.666(12)	2.765(38)	8.66×10^{-5}
0.27	0.6	$^*M_\pi L$	0.693(13)	0.667(12)	2.761(38)	7.33×10^{-5}
0.27	0.6	$a^2, M_\pi L$	0.673(13)	0.647(21)	2.835(74)	2.29×10^{-5}
0.27	0.6	$^*a^2, ^*M_\pi L$	0.663(20)	0.654(16)	2.828(93)	7.54×10^{-6}

TABLE XVII. Results for the neutron from the direct BχPT fits.

$M_{\pi,\mathrm{cut}}$ [GeV]	Q^2_{cut} [GeV^2]	Correction	$\langle r_E^2\rangle$ [fm^2]	$\langle r_M^2\rangle$ [fm^2]	μ_M	$\overline{\mathrm{BAIC}}$ weight
0.23	0.3	None	−0.116(11)	0.650(16)	−1.901(28)	0.0597
0.23	0.3	a^2	−0.104(13)	0.662(20)	−1.863(41)	0.0138
0.23	0.3	$^*a^2$	−0.103(15)	0.672(18)	−1.800(55)	0.0390
0.23	0.3	$M_\pi L$	−0.117(11)	0.651(18)	−1.918(28)	0.00135
0.23	0.3	$^*M_\pi L$	−0.118(12)	0.654(18)	−1.916(28)	0.00117
0.23	0.3	$a^2, M_\pi L$	−0.103(13)	0.664(25)	−1.878(42)	0.000279
0.23	0.3	$^*a^2, ^*M_\pi L$	−0.104(17)	0.679(23)	−1.810(58)	0.000586
0.23	0.4	None	−0.116(12)	0.652(11)	−1.904(30)	0.0198
0.23	0.4	a^2	−0.105(13)	0.668(16)	−1.854(47)	0.0611
0.23	0.4	$^*a^2$	−0.102(16)	0.676(14)	−1.799(58)	0.129
0.23	0.4	$M_\pi L$	−0.118(12)	0.647(15)	−1.923(30)	0.00106
0.23	0.4	$^*M_\pi L$	−0.120(13)	0.650(15)	−1.922(30)	0.000845
0.23	0.4	$a^2, M_\pi L$	−0.104(14)	0.665(23)	−1.873(48)	0.00141
0.23	0.4	$^*a^2, ^*M_\pi L$	−0.103(18)	0.679(20)	−1.813(61)	0.00180
0.23	0.5	None	−0.119(12)	0.6657(81)	−1.922(30)	0.0840
0.23	0.5	a^2	−0.115(13)	0.679(14)	−1.885(45)	0.0354
0.23	0.5	$^*a^2$	−0.115(16)	0.690(11)	−1.832(58)	0.0867
0.23	0.5	$M_\pi L$	−0.120(12)	0.664(13)	−1.943(30)	0.00402
0.23	0.5	$^*M_\pi L$	−0.122(12)	0.668(13)	−1.940(30)	0.00314
0.23	0.5	$a^2, M_\pi L$	−0.114(14)	0.680(22)	−1.905(46)	0.00101
0.23	0.5	$^*a^2, ^*M_\pi L$	−0.116(17)	0.698(19)	−1.841(61)	0.00159

(Table continued)

TABLE XVII. *(Continued)*

$M_{\pi,\mathrm{cut}}$ [GeV]	Q^2_{cut} [GeV^2]	Correction	$\langle r_E^2\rangle$ [fm^2]	$\langle r_M^2\rangle$ [fm^2]	μ_M	$\overline{\mathrm{BAIC}}$ weight
0.23	0.6	None	−0.119(10)	0.6644(75)	−1.920(29)	0.103
0.23	0.6	a^2	−0.114(12)	0.678(13)	−1.879(44)	0.0536
0.23	0.6	$^*a^2$	−0.112(16)	0.687(11)	−1.831(58)	0.0731
0.23	0.6	$M_\pi L$	−0.120(11)	0.657(13)	−1.939(29)	0.00469
0.23	0.6	$^*M_\pi L$	−0.122(11)	0.662(12)	−1.938(29)	0.00412
0.23	0.6	$a^2, M_\pi L$	−0.113(13)	0.673(21)	−1.902(45)	0.000887
0.23	0.6	$^*a^2, ^*M_\pi L$	−0.113(17)	0.689(18)	−1.846(62)	0.000941
0.27	0.3	None	−0.117(10)	0.645(14)	−1.934(28)	0.110
0.27	0.3	a^2	−0.117(12)	0.640(17)	−1.956(37)	0.00900
0.27	0.3	$^*a^2$	−0.120(15)	0.653(15)	−1.924(49)	0.0123
0.27	0.3	$M_\pi L$	−0.117(10)	0.648(17)	−1.952(28)	0.00122
0.27	0.3	$^*M_\pi L$	−0.117(11)	0.651(17)	−1.949(28)	0.00121
0.27	0.3	$a^2, M_\pi L$	−0.116(13)	0.641(22)	−1.975(39)	9.86×10^{-5}
0.27	0.3	$^*a^2, ^*M_\pi L$	−0.121(16)	0.661(20)	−1.938(52)	0.000110
0.27	0.4	None	−0.119(11)	0.649(11)	−1.941(29)	0.0225
0.27	0.4	a^2	−0.117(12)	0.647(13)	−1.951(42)	0.00509
0.27	0.4	$^*a^2$	−0.120(15)	0.659(12)	−1.930(51)	0.00682
0.27	0.4	$M_\pi L$	−0.119(12)	0.646(15)	−1.962(29)	0.000422
0.27	0.4	$^*M_\pi L$	−0.121(12)	0.650(15)	−1.960(29)	0.000350
0.27	0.4	$a^2, M_\pi L$	−0.117(13)	0.643(20)	−1.976(43)	6.60×10^{-5}
0.27	0.4	$^*a^2, ^*M_\pi L$	−0.122(16)	0.660(18)	−1.950(53)	5.45×10^{-5}
0.27	0.5	None	−0.122(11)	0.6585(78)	−1.957(29)	0.0253
0.27	0.5	a^2	−0.121(12)	0.648(11)	−1.989(40)	0.00361
0.27	0.5	$^*a^2$	−0.126(14)	0.6648(95)	−1.970(50)	0.00416
0.27	0.5	$M_\pi L$	−0.122(11)	0.662(13)	−1.980(29)	0.000499
0.27	0.5	$^*M_\pi L$	−0.123(12)	0.666(13)	−1.974(29)	0.000410
0.27	0.5	$a^2, M_\pi L$	−0.121(12)	0.649(19)	−2.014(41)	6.11×10^{-5}
0.27	0.5	$^*a^2, ^*M_\pi L$	−0.127(15)	0.673(17)	−1.984(53)	4.02×10^{-5}
0.27	0.6	None	−0.1208(96)	0.6533(71)	−1.948(27)	0.00555
0.27	0.6	a^2	−0.119(12)	0.640(11)	−1.989(41)	0.00246
0.27	0.6	$^*a^2$	−0.123(15)	0.6580(85)	−1.970(56)	0.00119
0.27	0.6	$M_\pi L$	−0.122(10)	0.654(12)	−1.971(27)	8.66×10^{-5}
0.27	0.6	$^*M_\pi L$	−0.123(11)	0.657(12)	−1.966(28)	7.33×10^{-5}
0.27	0.6	$a^2, M_\pi L$	−0.119(13)	0.638(19)	−2.016(42)	2.29×10^{-5}
0.27	0.6	$^*a^2, ^*M_\pi L$	−0.125(16)	0.663(16)	−1.987(59)	7.54×10^{-6}

which are presented here are included in our model average (*cf.* Sec. V). Note that the results for the proton and neutron have been obtained from the fits in the isovector and isoscalar channels; for more details, we refer to Sec. IV A.

APPENDIX F: z-EXPANSION RESULTS

In Tables XVIII–XXI, we present the results for the electromagnetic radii and the magnetic moment obtained from z-expansion fits on individual ensembles as detailed in Sec. IV B, applying two different cuts in the momentum transfer ($Q^2 \leq 0.6$ GeV^2 and $Q^2 \leq 0.7$ GeV^2).

TABLE XVIII. Results for the z-expansion fits to the isovector electromagnetic form factors.

Ensemble	Q^2_{cut} [GeV^2]	$\langle r_E^2\rangle$ [fm^2]	$\langle r_M^2\rangle$ [fm^2]	μ_M	p value
C101	0.6	0.644(26)	0.580(75)	4.21(16)	0.225
C101	0.7	0.643(26)	0.686(57)	4.36(15)	0.0358

(Table continued)

TABLE XVIII. *(Continued)*

Ensemble	Q^2_{cut} [GeV^2]	$\langle r_E^2 \rangle$ [fm^2]	$\langle r_M^2 \rangle$ [fm^2]	μ_M	p value
N101	0.6	0.597(19)	0.546(31)	4.385(97)	0.496
N101	0.7	0.595(17)	0.540(28)	4.385(96)	0.672
D450	0.6	0.687(33)	0.564(63)	4.20(17)	0.00299
D450	0.7	0.691(33)	0.577(60)	4.23(16)	0.0114
N451	0.6	0.592(19)	0.479(50)	4.34(13)	0.363
N451	0.7	0.590(19)	0.497(38)	4.37(12)	0.571
E250	0.6	0.62(11)	0.16(41)	3.98(39)	0.779
E250	0.7	0.59(11)	0.35(36)	4.03(37)	0.812
D200	0.6	0.639(46)	0.63(15)	4.26(28)	0.839
D200	0.7	0.655(44)	0.77(12)	4.42(26)	0.423
N200	0.6	0.511(39)	−0.09(36)	3.27(47)	0.268
N200	0.7	0.511(39)	−0.09(36)	3.27(47)	0.268
E300	0.6	0.771(65)	0.56(19)	3.97(33)	0.570
E300	0.7	0.758(64)	0.62(17)	4.02(32)	0.595
J303	0.6	0.611(47)	0.87(15)	5.15(50)	0.320
J303	0.7	0.628(41)	0.59(13)	4.43(37)	0.136

TABLE XIX. Results for the z-expansion fits to the isoscalar electromagnetic form factors.

Ensemble	Q^2_{cut} [GeV^2]	$\langle r_E^2 \rangle$ [fm^2]	$\langle r_M^2 \rangle$ [fm^2]	μ_M	p value
C101	0.6	0.549(15)	0.46(13)	2.74(24)	0.507
C101	0.7	0.546(15)	0.542(91)	2.82(22)	0.399
N101	0.6	0.4861(92)	0.517(67)	2.94(15)	0.394
N101	0.7	0.4812(89)	0.530(57)	2.96(15)	0.281
D450	0.6	0.517(16)	0.59(13)	2.94(25)	0.587
D450	0.7	0.518(15)	0.57(12)	2.92(25)	0.706
N451	0.6	0.494(11)	0.541(65)	3.16(16)	0.298
N451	0.7	0.489(11)	0.499(47)	3.09(14)	0.231
E250	0.6	0.635(46)	1.08(42)	3.52(66)	0.257
E250	0.7	0.619(44)	1.18(38)	3.52(66)	0.377
D200	0.6	0.492(19)	0.36(29)	2.40(35)	0.458
D200	0.7	0.501(18)	0.39(21)	2.45(30)	0.428
N200	0.6	0.484(18)	0.24(33)	2.64(50)	0.0972
N200	0.7	0.484(18)	0.24(33)	2.64(50)	0.0972
E300	0.6	0.579(26)	0.21(31)	2.26(38)	0.495
E300	0.7	0.562(25)	0.30(27)	2.33(37)	0.397
J303	0.6	0.480(20)	0.60(27)	3.04(55)	0.574
J303	0.7	0.469(17)	0.51(15)	2.88(39)	0.671

TABLE XX. Results for the z-expansion fits to the proton electromagnetic form factors.

Ensemble	Q^2_{cut} [GeV^2]	$\langle r_E^2 \rangle$ [fm^2]	$\langle r_M^2 \rangle$ [fm^2]	μ_M	p value
C101	0.6	0.615(19)	0.598(83)	2.61(11)	0.683
C101	0.7	0.618(19)	0.678(70)	2.66(11)	0.0739
N101	0.6	0.552(14)	0.545(36)	2.703(65)	0.181
N101	0.7	0.552(13)	0.543(33)	2.701(64)	0.326
D450	0.6	0.609(23)	0.551(78)	2.58(12)	0.00248
D450	0.7	0.607(23)	0.551(77)	2.58(11)	0.00774
N451	0.6	0.565(15)	0.502(50)	2.699(82)	0.104
N451	0.7	0.566(15)	0.506(39)	2.702(74)	0.218
E250	0.6	0.562(80)	0.21(50)	2.47(27)	0.367

(Table continued)

TABLE XX. *(Continued)*

Ensemble	Q^2_{cut} [GeV^2]	$\langle r_E^2 \rangle$ [fm^2]	$\langle r_M^2 \rangle$ [fm^2]	μ_M	p value
E250	0.7	0.555(79)	0.17(49)	2.42(26)	0.536
D200	0.6	0.574(31)	0.54(18)	2.49(18)	0.644
D200	0.7	0.588(30)	0.68(14)	2.59(17)	0.255
N200	0.6	0.513(26)	−0.03(35)	2.08(30)	0.218
N200	0.7	0.513(26)	−0.03(35)	2.08(30)	0.218
E300	0.6	0.699(43)	0.42(22)	2.33(21)	0.733
E300	0.7	0.679(42)	0.49(20)	2.36(21)	0.545
J303	0.6	0.559(32)	0.83(17)	3.07(33)	0.176
J303	0.7	0.568(28)	0.57(13)	2.68(24)	0.150

TABLE XXI. Results for the z-expansion fits to the neutron electromagnetic form factors.

Ensemble	Q^2_{cut} [GeV^2]	$\langle r_E^2 \rangle$ [fm^2]	$\langle r_M^2 \rangle$ [fm^2]	μ_M	p value
C101	0.6	−0.031(13)	0.605(86)	−1.660(73)	0.227
C101	0.7	−0.031(12)	0.691(68)	−1.726(67)	0.0664
N101	0.6	−0.0392(69)	0.546(41)	−1.709(49)	0.454
N101	0.7	−0.0371(67)	0.551(38)	−1.717(49)	0.424
D450	0.6	−0.061(14)	0.45(10)	−1.576(76)	0.581
D450	0.7	−0.063(14)	0.473(96)	−1.577(75)	0.538
N451	0.6	−0.0274(76)	0.442(67)	−1.624(60)	0.870
N451	0.7	−0.0258(75)	0.468(48)	−1.640(54)	0.896
E250	0.6	−0.123(50)	−0.15(78)	−1.46(21)	0.893
E250	0.7	−0.114(49)	−0.25(74)	−1.43(20)	0.969
D200	0.6	−0.056(22)	0.73(15)	−1.75(12)	0.649
D200	0.7	−0.060(21)	0.88(12)	−1.83(12)	0.417
N200	0.6	0.003(19)	−0.22(49)	−1.18(21)	0.504
N200	0.7	0.003(19)	−0.22(49)	−1.18(21)	0.504
E300	0.6	−0.082(30)	0.65(20)	−1.59(14)	0.561
E300	0.7	−0.079(29)	0.70(19)	−1.62(14)	0.667
J303	0.6	−0.045(20)	0.92(16)	−2.05(21)	0.596
J303	0.7	−0.054(18)	0.61(14)	−1.74(16)	0.203

APPENDIX G: CHIRAL AND CONTINUUM EXTRAPOLATION

In Table XXII, we summarize the results for the physical values of the electromagnetic radii and the magnetic moment obtained from the HBχPT-inspired chiral and continuum extrapolation of the z-expansion data as explained in Sec. IV B, applying two different cuts each in the pion mass ($M_\pi \leq 0.27$ GeV and $M_\pi \leq 0.3$ GeV) and the momentum transfer ($Q^2 \leq 0.6$ GeV^2 and $Q^2 \leq 0.7$ GeV^2). Ensembles which are solely used to study finite-volume effects (H105 and S201) are excluded from all fits.

TABLE XXII. Results of the chiral and continuum extrapolation for the z-expansion extractions.

Channel	$M_{\pi,\text{cut}}$ [GeV]	Q^2_{cut} [GeV^2]	$\langle r_E^2 \rangle$ [fm^2]	$\langle r_M^2 \rangle$ [fm^2]	μ_M	p value
$u-d$	0.27	0.6	0.740(80)	0.38(27)	4.09(36)	0.562
$u-d$	0.27	0.7	0.727(79)	0.54(24)	4.02(34)	0.364
$u-d$	0.30	0.6	0.739(54)	0.65(16)	4.04(26)	0.0573
$u-d$	0.30	0.7	0.750(53)	0.81(14)	4.04(25)	0.0676
$u+d-2s$	0.27	0.6	0.557(31)	0.52(34)	2.43(46)	0.0557
$u+d-2s$	0.27	0.7	0.551(29)	0.52(29)	2.41(45)	0.247
$u+d-2s$	0.30	0.6	0.553(20)	0.44(23)	2.40(35)	0.167
$u+d-2s$	0.30	0.7	0.550(19)	0.47(17)	2.39(32)	0.350

(Table continued)

TABLE XXII. *(Continued)*

Channel	$M_{\pi,\mathrm{cut}}$ [GeV]	Q^2_{cut} [GeV^2]	$\langle r_E^2\rangle$ [fm^2]	$\langle r_M^2\rangle$ [fm^2]	μ_M	p value
p	0.27	0.6	0.643(56)	0.23(32)	2.33(24)	0.414
p	0.27	0.7	0.625(53)	0.37(29)	2.34(23)	0.453
p	0.30	0.6	0.668(37)	0.57(19)	2.37(17)	0.131
p	0.30	0.7	0.667(35)	0.70(17)	2.38(17)	0.150
n	0.27	0.6	−0.132(37)	0.54(33)	−1.65(16)	0.687
n	0.27	0.7	−0.125(36)	0.80(29)	−1.65(15)	0.272
n	0.30	0.6	−0.084(24)	0.75(20)	−1.57(12)	0.0648
n	0.30	0.7	−0.094(23)	0.93(17)	−1.59(11)	0.0634

[1] F. Wilczek, Origins of mass, Cent. Eur. J. Phys. **10**, 1021 (2012).
[2] J.-P. Karr, D. Marchand, and E. Voutier, The proton size, Nat. Rev. Phys. **2**, 601 (2020).
[3] J. C. Bernauer *et al.* (A1 Collaboration), Electric and magnetic form factors of the proton, Phys. Rev. C **90**, 015206 (2014).
[4] P. J. Mohr, B. N. Taylor, and D. B. Newell, CODATA recommended values of the fundamental physical constants: 2010, Rev. Mod. Phys. **84**, 1527 (2012).
[5] R. Pohl *et al.*, The size of the proton, Nature (London) **466**, 213 (2010).
[6] A. Antognini *et al.*, Proton structure from the measurement of 2S-2P transition frequencies of muonic hydrogen, Science **339**, 417 (2013).
[7] C. E. Carlson, The proton radius puzzle, Prog. Part. Nucl. Phys. **82**, 59 (2015).
[8] A. Beyer *et al.*, The Rydberg constant and proton size from atomic hydrogen, Science **358**, 79 (2017).
[9] N. Bezginov, T. Valdez, M. Horbatsch, A. Marsman, A. C. Vutha, and E. A. Hessels, A measurement of the atomic hydrogen lamb shift and the proton charge radius, Science **365**, 1007 (2019).
[10] A. Grinin, A. Matveev, D. C. Yost, L. Maisenbacher, V. Wirthl, R. Pohl, T. W. Hänsch, and T. Udem, Two-photon frequency comb spectroscopy of atomic hydrogen, Science **370**, 1061 (2020).
[11] H. Fleurbaey, S. Galtier, S. Thomas, M. Bonnaud, L. Julien, F. Biraben, F. Nez, M. Abgrall, and J. Guéna, New measurement of the $1S-3S$ transition frequency of hydrogen: Contribution to the proton charge radius puzzle, Phys. Rev. Lett. **120**, 183001 (2018).
[12] M. Mihovilovič *et al.*, The proton charge radius extracted from the initial-state radiation experiment at MAMI, Eur. Phys. J. A **57**, 107 (2021).
[13] W. Xiong *et al.*, A small proton charge radius from an electron-proton scattering experiment, Nature (London) **575**, 147 (2019).
[14] P. Mergell, U.-G. Meißner, and D. Drechsel, Dispersion-theoretical analysis of the nucleon electromagnetic form factors, Nucl. Phys. **A596**, 367 (1996).
[15] M. A. Belushkin, H.-W. Hammer, and U.-G. Meißner, Dispersion analysis of the nucleon form factors including meson continua, Phys. Rev. C **75**, 035202 (2007).
[16] M. Hoferichter, B. Kubis, J. Ruiz de Elvira, H.-W. Hammer, and U.-G. Meißner, On the $\pi\pi$ continuum in the nucleon form factors and the proton radius puzzle, Eur. Phys. J. A **52**, 331 (2016).
[17] Y.-H. Lin, H.-W. Hammer, and U.-G. Meißner, High-precision determination of the electric and magnetic radius of the proton, Phys. Lett. B **816**, 136254 (2021).
[18] Y.-H. Lin, H.-W. Hammer, and U.-G. Meißner, Dispersion-theoretical analysis of the electromagnetic form factors of the nucleon: Past, present and future, Eur. Phys. J. A **57**, 255 (2021).
[19] Y.-H. Lin, H.-W. Hammer, and U.-G. Meißner, New insights into the nucleon's electromagnetic structure, Phys. Rev. Lett. **128**, 052002 (2022).
[20] I. T. Lorenz, U.-G. Meißner, H.-W. Hammer, and Y.-B. Dong, Theoretical constraints and systematic effects in the determination of the proton form factors, Phys. Rev. D **91**, 014023 (2015).
[21] J. M. Alarcón, D. W. Higinbotham, and C. Weiss, Precise determination of the proton magnetic radius from electron scattering data, Phys. Rev. C **102**, 035203 (2020).
[22] S. Grieser, D. Bonaventura, P. Brand, C. Hargens, B. Hetz, L. Leßmann, C. Westphälinger, and A. Khoukaz, A cryogenic supersonic jet target for electron scattering experiments at MAGIX@MESA and MAMI, Nucl. Instrum. Methods Phys. Res., Sect. A **906**, 120 (2018).
[23] A. Gasparian *et al.* (PRad Collaboration), PRad-II: A new upgraded high precision measurement of the proton charge radius, arXiv:2009.10510.
[24] T. Suda, Low-energy electron scattering facilities in Japan, J. Phys. Conf. Ser. **2391**, 012004 (2022).
[25] E. Cline, J. Bernauer, E. J. Downie, and R. Gilman, MUSE: The MUon scattering experiment, SciPost Phys. Proc. **5**, 023 (2021).
[26] C. Quintans (AMBER collaboration), The new AMBER experiment at the CERN SPS, Few-Body Syst. **63**, 72 (2022).

[27] G. Lee, J. R. Arrington, and R. J. Hill, Extraction of the proton radius from electron-proton scattering data, Phys. Rev. D **92**, 013013 (2015).
[28] B. Ledroit and K. Aulenbacher, Collimation of target induced halo following MAGIX at MESA, J. Phys. Conf. Ser. **1350**, 012138 (2019).
[29] H. Fritzsch, M. Gell-Mann, and H. Leutwyler, Advantages of the color octet gluon picture, Phys. Lett. **47B**, 365 (1973).
[30] K. G. Wilson, Confinement of quarks, Phys. Rev. D **10**, 2445 (1974).
[31] M. Göckeler, T. R. Hemmert, R. Horsley, D. Pleiter, P. E. L. Rakow, A. Schäfer, and G. Schierholz (QCDSF Collaboration), Nucleon electromagnetic form factors on the lattice and in chiral effective field theory, Phys. Rev. D **71**, 034508 (2005).
[32] T. Yamazaki, Y. Aoki, T. Blum, H.-W. Lin, S. Ohta, S. Sasaki, R. Tweedie, and J. Zanotti (RBC and UKQCD Collaborations), Nucleon form factors with $2+1$ flavor dynamical domain-wall fermions, Phys. Rev. D **79**, 114505 (2009).
[33] S. N. Syritsyn *et al.* (LHPC Collaboration), Nucleon electromagnetic form factors from lattice QCD using $2+1$ flavor domain wall fermions on fine lattices and chiral perturbation theory, Phys. Rev. D **81**, 034507 (2010).
[34] J. D. Bratt *et al.* (LHPC Collaboration), Nucleon structure from mixed action calculations using $2+1$ flavors of asqtad sea and domain wall valence fermions, Phys. Rev. D **82**, 094502 (2010).
[35] C. Alexandrou, M. Constantinou, S. Dinter, V. Drach, K. Jansen, C. Kallidonis, and G. Koutsou, Nucleon form factors and moments of generalized parton distributions using N_f=2+1+1 twisted mass fermions, Phys. Rev. D **88**, 014509 (2013).
[36] T. Bhattacharya, S. D. Cohen, R. Gupta, A. Joseph, H.-W. Lin, and B. Yoon, Nucleon charges and electromagnetic form factors from $2+1+1$-flavor lattice QCD, Phys. Rev. D **89**, 094502 (2014).
[37] P. E. Shanahan, R. Horsley, Y. Nakamura, D. Pleiter, P. E. L. Rakow, G. Schierholz, H. Stüben, A. W. Thomas, R. D. Young, and J. M. Zanotti (CSSM and QCDSF/UKQCD Collaborations), Magnetic form factors of the octet baryons from lattice QCD and chiral extrapolation, Phys. Rev. D **89**, 074511 (2014).
[38] P. E. Shanahan, R. Horsley, Y. Nakamura, D. Pleiter, P. E. L. Rakow, G. Schierholz, H. Stüben, A. W. Thomas, R. D. Young, and J. M. Zanotti (CSSM and QCDSF/UKQCD Collaborations), Electric form factors of the octet baryons from lattice QCD and chiral extrapolation, Phys. Rev. D **90**, 034502 (2014).
[39] J. R. Green, J. W. Negele, A. V. Pochinsky, S. N. Syritsyn, M. Engelhardt, and S. Krieg, Nucleon electromagnetic form factors from lattice QCD using a nearly physical pion mass, Phys. Rev. D **90**, 074507 (2014).
[40] S. Capitani, M. Della Morte, D. Djukanovic, G. von Hippel, J. Hua, B. Jäger, B. Knippschild, H. B. Meyer, T. D. Rae, and H. Wittig, Nucleon electromagnetic form factors in two-flavor QCD, Phys. Rev. D **92**, 054511 (2015).
[41] C. Alexandrou, M. Constantinou, K. Hadjiyiannakou, K. Jansen, C. Kallidonis, G. Koutsou, and A. Vaquero Aviles-Casco, Nucleon electromagnetic form factors using lattice simulations at the physical point, Phys. Rev. D **96**, 034503 (2017).
[42] N. Hasan, J. Green, S. Meinel, M. Engelhardt, S. Krieg, J. Negele, A. Pochinsky, and S. Syritsyn, Computing the nucleon charge and axial radii directly at $Q^2 = 0$ in lattice QCD, Phys. Rev. D **97**, 034504 (2018).
[43] K.-I. Ishikawa, Y. Kuramashi, S. Sasaki, N. Tsukamoto, A. Ukawa, and T. Yamazaki (PACS Collaboration), Nucleon form factors on a large volume lattice near the physical point in $2+1$ flavor QCD, Phys. Rev. D **98**, 074510 (2018).
[44] E. Shintani, K.-I. Ishikawa, Y. Kuramashi, S. Sasaki, and T. Yamazaki (PACS Collaboration), Nucleon form factors and root-mean-square radii on a $(10.8\ \mathrm{fm})^4$ lattice at the physical point, Phys. Rev. D **99**, 014510 (2019); **102**, 019902(E) (2020).
[45] C. Alexandrou, S. Bacchio, M. Constantinou, J. Finkenrath, K. Hadjiyiannakou, K. Jansen, G. Koutsou, and A. V. Aviles-Casco, Proton and neutron electromagnetic form factors from lattice QCD, Phys. Rev. D **100**, 014509 (2019).
[46] C. Alexandrou, K. Hadjiyiannakou, G. Koutsou, K. Ottnad, and M. Petschlies, Model-independent determination of the nucleon charge radius from lattice QCD, Phys. Rev. D **101**, 114504 (2020).
[47] D. Djukanovic, T. Harris, G. von Hippel, P. M. Junnarkar, H. B. Meyer, D. Mohler, K. Ottnad, T. Schulz, J. Wilhelm, and H. Wittig, Isovector electromagnetic form factors of the nucleon from lattice QCD and the proton radius puzzle, Phys. Rev. D **103**, 094522 (2021).
[48] K.-I. Ishikawa, Y. Kuramashi, S. Sasaki, E. Shintani, and T. Yamazaki (PACS Collaboration), Calculation of derivative of nucleon form factors in $N_f = 2+1$ lattice QCD at $M_\pi = 138$ MeV on a $(5.5\ \mathrm{fm})^3$ volume, Phys. Rev. D **104**, 074514 (2021).
[49] M. Bruno *et al.*, Simulation of QCD with $N_\mathrm{f} = 2+1$ flavors of non-perturbatively improved Wilson fermions, J. High Energy Phys. 02 (2015) 043.
[50] D. Djukanovic, G. von Hippel, H. B. Meyer, K. Ottnad, M. Salg, and H. Wittig, companion Letter, Precision calculation of the electromagnetic radii of the proton and neutron from lattice QCD, Phys. Rev. Lett. **132**, 211901 (2024).
[51] B. Sheikholeslami and R. Wohlert, Improved continuum limit lattice action for QCD with Wilson fermions, Nucl. Phys. **B259**, 572 (1985).
[52] J. Bulava and S. Schaefer, Improvement of $N_f = 3$ lattice QCD with Wilson fermions and tree-level improved gauge action, Nucl. Phys. **B874**, 188 (2013).
[53] M. Lüscher and P. Weisz, On-shell improved lattice gauge theories, Commun. Math. Phys. **97**, 59 (1985); **98**, 433(E) (1985).
[54] S. Schaefer, R. Sommer, and F. Virotta, Critical slowing down and error analysis in lattice QCD simulations, Nucl. Phys. **B845**, 93 (2011).
[55] M. Lüscher and S. Schaefer, Lattice QCD without topology barriers, J. High Energy Phys. 07 (2011) 036.
[56] M. Lüscher and S. Schaefer, Lattice QCD with open boundary conditions and twisted-mass reweighting, Comput. Phys. Commun. **184**, 519 (2013).
[57] F. Palombi and M. Lüscher, Fluctuations and reweighting of the quark determinant on large lattices, Proc. Sci. LATTICE2008 (**2008**) 049 [arXiv:0810.0946].

[58] I. Horváth, A. D. Kennedy, and S. Sint, A new exact method for dynamical fermion computations with non-local actions, Nucl. Phys. B, Proc. Suppl. **73**, 834 (1999).

[59] M. A. Clark and A. D. Kennedy, Accelerating dynamical-fermion computations using the rational hybrid Monte Carlo algorithm with multiple pseudofermion fields, Phys. Rev. Lett. **98**, 051601 (2007).

[60] S. Kuberski, Low-mode deflation for twisted-mass and RHMC reweighting in lattice QCD, Comput. Phys. Commun. **300**, 109173 (2024).

[61] D. Mohler and S. Schaefer, Remarks on strange-quark simulations with Wilson fermions, Phys. Rev. D **102**, 074506 (2020).

[62] D. Djukanovic, G. von Hippel, J. Koponen, H. B. Meyer, K. Ottnad, T. Schulz, and H. Wittig, The isovector axial form factor of the nucleon from lattice QCD, Phys. Rev. D **106**, 074503 (2022).

[63] A. Agadjanov, D. Djukanovic, G. von Hippel, H. B. Meyer, K. Ottnad, and H. Wittig, Nucleon sigma terms with $N_f = 2 + 1$ flavors of $\mathcal{O}(a)$-improved Wilson fermions, Phys. Rev. Lett. **131**, 261902 (2023).

[64] S. Güsken, U. Löw, K.-H. Mütter, R. Sommer, A. Patel, and K. Schilling, Non-singlet axial vector couplings of the baryon octet in lattice QCD, Phys. Lett. B **227**, 266 (1989).

[65] M. Albanese *et al.* (APE Collaboration), Glueball masses and string tension in lattice QCD, Phys. Lett. B **192**, 163 (1987).

[66] G. von Hippel, B. Jäger, T. D. Rae, and H. Wittig, The shape of covariantly smeared sources in lattice QCD, J. High Energy Phys. 09 (2013) 014.

[67] G. Martinelli and C. T. Sachrajda, A lattice study of nucleon structure, Nucl. Phys. **B316**, 355 (1989).

[68] L. Giusti, T. Harris, A. Nada, and S. Schaefer, Frequency-splitting estimators of single-propagator traces, Eur. Phys. J. C **79**, 586 (2019).

[69] V. Gülpers, G. von Hippel, and H. Wittig, Scalar pion form factor in two-flavor lattice QCD, Phys. Rev. D **89**, 094503 (2014).

[70] A. Stathopoulos, J. Laeuchli, and K. Orginos, Hierarchical probing for estimating the trace of the matrix inverse on toroidal lattices, SIAM J. Sci. Comput. **35**, S299 (2013).

[71] C. McNeile and C. Michael (UKQCD Collaboration), Decay width of light quark hybrid meson from the lattice, Phys. Rev. D **73**, 074506 (2006).

[72] P. Boucaud *et al.* (ETM Collaboration), Dynamical twisted mass fermions with light quarks: Simulation and analysis details, Comput. Phys. Commun. **179**, 695 (2008).

[73] M. Cè, A. Gérardin, G. von Hippel, H. B. Meyer, K. Miura, K. Ottnad, A. Risch, T. S. José, J. Wilhelm, and H. Wittig, The hadronic running of the electromagnetic coupling and the electroweak mixing angle from lattice QCD, J. High Energy Phys. 08 (2022) 220.

[74] G. S. Bali, S. Collins, and A. Schäfer, Effective noise reduction techniques for disconnected loops in Lattice QCD, Comput. Phys. Commun. **181**, 1570 (2010).

[75] T. Blum, T. Izubuchi, and E. Shintani, New class of variance-reduction techniques using lattice symmetries, Phys. Rev. D **88**, 094503 (2013).

[76] E. Shintani, R. Arthur, T. Blum, T. Izubuchi, C. Jung, and C. Lehner, Covariant approximation averaging, Phys. Rev. D **91**, 114511 (2015).

[77] T. A. DeGrand, A conditioning technique for matrix inversion for Wilson fermions, Comput. Phys. Commun. **52**, 161 (1988).

[78] M. Lüscher, Lattice QCD and the Schwarz alternating procedure, J. High Energy Phys. 05 (2003) 052.

[79] A. Gérardin, T. Harris, and H. B. Meyer, Nonperturbative renormalization and O(a)-improvement of the nonsinglet vector current with $N_f = 2 + 1$ Wilson fermions and tree-level Symanzik improved gauge action, Phys. Rev. D **99**, 014519 (2019).

[80] T. Korzec, C. Alexandrou, G. Koutsou, M. Brinet, J. Carbonell, V. Drach, P.-A. Harraud, and R. Baron (European Twisted Mass Collaboration), Nucleon form factors with dynamical twisted mass fermions, Proc. Sci. LATTICE2008 (**2008**) 139 [arXiv:0811.0724].

[81] G. S. Bali, S. Collins, S. Heybrock, M. Löffler, R. Rödl, W. Söldner, and S. Weishäupl (RQCD Collaboration), Octet baryon isovector charges from $N_f = 2 + 1$ lattice QCD, Phys. Rev. D **108**, 034512 (2023).

[82] M. Bruno, T. Korzec, and S. Schaefer, Setting the scale for the CLS $2 + 1$ flavor ensembles, Phys. Rev. D **95**, 074504 (2017).

[83] Y. Aoki *et al.* (Flavour Lattice Averaging Group), FLAG review 2021, Eur. Phys. J. C **82**, 869 (2022).

[84] H. W. Hamber, E. Marinari, G. Parisi, and C. Rebbi, Considerations on numerical analysis of QCD, Nucl. Phys. **B225**, 475 (1983).

[85] G. P. Lepage, The analysis of algorithms for lattice field theory, in *Theoretical Advanced Study Institute in Elementary Particle Physics* (World Scientific, Singapore, 1989), pp. 97–120.

[86] K. Ottnad, Excited states in nucleon structure calculations, Eur. Phys. J. A **57**, 50 (2021).

[87] L. Maiani, G. Martinelli, M. L. Paciello, and B. Taglienti, Scalar densities and baryon mass differences in lattice QCD with Wilson fermions, Nucl. Phys. **B293**, 420 (1987).

[88] T. Doi, M. Deka, S.-J. Dong, T. Draper, K.-F. Liu, D. Mankame, N. Mathur, and T. Streuer (χQCD Collaboration), Nucleon strangeness form factors from $N_f = 2 + 1$ clover fermion lattice QCD, Phys. Rev. D **80**, 094503 (2009).

[89] S. Capitani, M. Della Morte, G. von Hippel, B. Jäger, A. Jüttner, B. Knippschild, H. B. Meyer, and H. Wittig, The nucleon axial charge from lattice QCD with controlled errors, Phys. Rev. D **86**, 074502 (2012).

[90] T. Bauer, J. C. Bernauer, and S. Scherer, Electromagnetic form factors of the nucleon in effective field theory, Phys. Rev. C **86**, 065206 (2012).

[91] R. L. Workman *et al.* (Particle Data Group), Review of particle physics, Prog. Theor. Exp. Phys. **2022**, 083C01 (2022).

[92] K. Kawarabayashi and M. Suzuki, Partially conserved axial-vector current and the decays of vector mesons, Phys. Rev. Lett. **16**, 255 (1966); **16**, 384(E) (1966).

[93] Riazuddin and Fayyazuddin, Algebra of current components and decay widths of ρ and K^* mesons, Phys. Rev. **147**, 1071 (1966).

[94] D. Djukanovic, M. R. Schindler, J. Gegelia, G. Japaridze, and S. Scherer, Universality of the ρ meson coupling in effective field theory, Phys. Rev. Lett. **93**, 122002 (2004).
[95] T. Hahn and M. Pérez-Victoria, Automated one-loop calculations in four and D dimensions, Comput. Phys. Commun. **118**, 153 (1999).
[96] G. J. van Oldenborgh and J. A. M. Vermaseren, New algorithms for one-loop integrals, Z. Phys. C **46**, 425 (1990).
[97] T. Bauer, Elektromagnetische Formfaktoren des Nukleons in effektiver Feldtheorie, Diploma thesis, Johannes Gutenberg-Universität Mainz, Mainz, 2009.
[98] S. Aoki *et al.* (FLAG Working Group), Review of lattice results concerning low-energy particle physics, Eur. Phys. J. C **74**, 2890 (2014).
[99] S. R. Beane, Nucleon masses and magnetic moments in a finite volume, Phys. Rev. D **70**, 034507 (2004).
[100] R. J. Hill and G. Paz, Model-independent extraction of the proton charge radius from electron scattering, Phys. Rev. D **82**, 113005 (2010).
[101] V. Bernard, H. W. Fearing, T. R. Hemmert, and U.-G. Meißner, The form factors of the nucleon at small momentum transfer, Nucl. Phys. **A635**, 121 (1998); **A642**, 563(E) (1998).
[102] H. Akaike, Information theory and an extension of the maximum likelihood principle, in *Proceedings of the 2nd International Symposium on Information Theory*, edited by B. N. Petrov and F. Csaki (Akadémiai Kiadó, Budapest, 1973), pp. 267–281.
[103] H. Akaike, A new look at the statistical model identification, IEEE Trans. Autom. Control **19**, 716 (1974).
[104] E. T. Neil and J. W. Sitison, Improved information criteria for Bayesian model averaging in lattice field theory, Phys. Rev. D **109**, 014510 (2024).
[105] K. P. Burnham and D. R. Anderson, Multimodel inference: Understanding AIC and BIC in model selection, Social. Methods Res. **33**, 261 (2004).
[106] S. Borsányi *et al.*, *Ab initio* calculation of the neutron-proton mass difference, Science **347**, 1452 (2015).
[107] S. Borsányi *et al.*, Leading hadronic contribution to the muon magnetic moment from lattice QCD, Nature (London) **593**, 51 (2021).
[108] N. Carrasco *et al.* (The European Twisted Mass Collaboration), Up, down, strange and charm quark masses with $N_f = 2 + 1 + 1$ twisted mass lattice QCD, Nucl. Phys. **B887**, 19 (2014).
[109] Z. Ye, J. Arrington, R. J. Hill, and G. Lee, Proton and neutron electromagnetic form factors and uncertainties, Phys. Lett. B **777**, 8 (2018).
[110] H.-W. Hammer and U.-G. Meißner, The proton radius: From a puzzle to precision, Sci. Bull. **65**, 257 (2020).
[111] E. Tiesinga, P. J. Mohr, D. B. Newell, and B. N. Taylor, CODATA recommended values of the fundamental physical constants: 2018, Rev. Mod. Phys. **93**, 025010 (2021).
[112] A. Antognini, F. Hagelstein, and V. Pascalutsa, The proton structure in and out of muonic hydrogen, Annu. Rev. Nucl. Part. Sci. **72**, 389 (2022).
[113] https://hpc.uni-mainz.de.
[114] https://www.ahrp.info.
[115] https://www.gauss-centre.eu.
[116] R. G. Edwards and B. Joó, The Chroma software system for lattice QCD, Nucl. Phys. B, Proc. Suppl. **140**, 832 (2005).
[117] D. Djukanovic, Quark contraction tool—QCT, Comput. Phys. Commun. **247**, 106950 (2020).
[118] T. Harris, G. von Hippel, P. Junnarkar, H. B. Meyer, K. Ottnad, J. Wilhelm, H. Wittig, and L. Wrang, Nucleon isovector charges and twist-2 matrix elements with $N_f = 2 + 1$ dynamical Wilson quarks, Phys. Rev. D **100**, 034513 (2019).
[119] A. M. Segner, A. Risch, and H. Wittig, Precision determination of baryon masses including isospin-breaking, arXiv:2312.09065.
[120] G. H. Golub and V. Pereyra, The differentiation of pseudo-inverses and nonlinear least squares problems whose variables separate, SIAM J. Numer. Anal. **10**, 413 (1973).